CHALMERS

Numerical Investigation of Ship Responses in Calm Water and Regular Head Waves

MOHSEN IRANNEZHAD

Department of Mechanics and Maritime Sciences
CHALMERS UNIVERSITY OF TECHNOLOGY
Göteborg, Sweden 2022

THESIS FOR THE DEGREE OF LICENTIATE OF ENGINEERING

Numerical Investigation of Ship Responses in Calm Water and Regular Head Waves

MOHSEN IRANNEZHAD

Department of Mechanics and Maritime Sciences
Division of Marine Technology
CHALMERS UNIVERSITY OF TECHNOLOGY

Göteborg, Sweden 2022

Numerical Investigation of Ship Responses in Calm Water and Regular Head Waves
MOHSEN IRANNEZHAD

Thesis for the degree of Licentiate of Engineering 2022:04
ISSN 1652-8565
Department of Mechanics and Maritime Sciences
Division of Marine Technology
Chalmers University of Technology
SE-412 96 Göteborg
Sweden
Telephone: +46 (0)31-772 1000

Chalmers Reproservice
Göteborg, Sweden 2022

Numerical Investigation of Ship Responses in Calm Water and Regular Head Waves

MOHSEN IRANNEZHAD
Department of Mechanics and Maritime Sciences
Division of Marine Technology
Chalmers University of Technology

Abstract

In order to design fuel efficient ships and install right machinery onboard, ship designers need to know the interaction effects between hull, propeller and appendages in realistic operating conditions. Neglecting the interaction effects may result in under/over-prediction of the required power. Moreover, with the current strict regulations for reducing CO2 footprint from shipping different type of solutions should be implemented to comply with the regulations. Developing accurate and reliable engineering methods that can predict ship resistance and power in realistic operating conditions, such as in waves, can be an important contribution to achieve the aforementioned needs of the shipping industry.

Traditionally, ships power prediction has been carried out for the ships operating in calm water rather than more realistic environmental conditions. However, waves can play a significant role on ship performance at sea. In this thesis, as a first step towards prediction of interaction effects in waves, bare hull performance prediction in calm water and regular head waves is carried out using two distinct numerical methods. First, a Fully Nonlinear Potential Flow (FNPF) method is used to investigate a ship performance in a broad range of operational conditions. The analysis of results provided a valuable insight into the ship hydrodynamic responses and the correlation between them. Subsequently, a state-of-the-art Computational Fluid Dynamics (CFD) method is employed using a Reynolds-Averaged Navier-Stokes (RANS) approach. Besides ship hydrodynamic responses, the results from this method provided a detailed information about the flow field around the hull, including its transient nominal wake. In addition, a formal verification and validation (V&V) procedure is applied to understand and control the numerical and modeling error in the RANS computations.

Generally, the results of the employed numerical methods were in a good agreement with the experimental data. The prediction of ship motions and to some extend resistance in the FNPF method were rather accurate, however, due to the higher level of simplifications and approximations in this method, the RANS method deemed a better candidate for prediction of ship wake. The computational costs of RANS methods are 2-3 order of magnitude higher than that of FNPF. The ship hydrodynamic responses and the flow field analyses from this thesis can shed more light onto the hull wave interaction effects and help the ship/propeller designers to optimize their designs for more realistic conditions than only calm water.

Keywords: Ship motions, Resistance, Nominal wake, Regular head waves, FNPF, CFD, RANS.

Acknowledgements

This thesis is based on a research work carried out at the Division of Marine Technology, Department of Mechanics and Maritime sciences at Chalmers University of Technology. The research is funded by The Swedish Transport Administration through Lighthouse (Swedish Maritime Competence Center) as well as LeanShips project through the European Union's Horizon 2020 research and innovation programme (Contract No.: 636146). The simulations were performed on resources at Chalmers Centre for Computational Science and Engineering (C3SE) as well as National Supercomputer Center at Linköping University (NSC) provided by the Swedish National Infrastructure for Computing (SNIC).

I would like to greatly acknowledge Professor Yasuyuki Toda from Osaka University for generously sharing a considerable amount of experimental data for the KVLCC2 tanker. The Maritime Research Institute Netherlands (MARIN) is also acknowledged for providing the experimental data for the LDP vessel.

This project had not been possible without all the great people that have surrounded me and provided advice and feedback. First, I would like to sincerely thank my main supervisor Arash Eslamdoost for his constant encouragement, support and assistance during the project. I am very thankful for the technical experience he brought into the project and always finding time to support me, especially at the times that the research did not go as planned. In addition, I would like to thank my co-supervisor and examiner Rickard E. Bensow for the valuable help, discussions and guidance. I would also like to thank my co-supervisor Martin Kjellberg from SSPA AB for all the help and discussions in this project.

I would like to thank all my current and former colleagues at the Division of Marine Technology for creating a nice working environment. Special thanks to Mohammad, Ioli, Mehmet, Saeed and Muye for all the supports and wonderful moments that we share.

Finally, I would like to thank my supportive and lovely parents, my brothers Mike and Masoud who have always been there for me and they are my role models, my lovely girlfriend Rojin for all the patience and support in my ups and downs and all my friends, Alireza, Rasool, Setareh, Mohammad and Homayoon for never-ending positive energy that I have received from you.

List of Publications

This thesis includes both an original unpublished part as well as a re-used part from the author's publications provided here:

- Irannezhad, M., Eslamdoost A., Kjellberg M., and Bensow, R. E. (2022). Investigation of ship responses in regular head waves through a Fully Nonlinear Potential Flow approach. *Ocean Engineering* **246**, 110410. issn: 0029-8018. doi:10.1016/j.oceaneng.2021.110410.

- Irannezhad, M., Bensow, R. E., Kjellberg M., and Eslamdoost A. (2021). Towards uncertainty analysis of CFD simulation of ship responses in regular head waves. In: Proceedings of the 23rd Numerical Towing Tank Symposium (NuTTS 2021).

- Irannezhad, M., Eslamdoost A., and Bensow, R. E. (2019a). Numerical investigation of a general cargo vessel wake in waves. In: Proceedings of the 22nd Numerical Towing Tank Symposium (NuTTS 2019).

- Irannezhad, M., Eslamdoost A., and Bensow, R. E. (2019b). Numerical investigation of a large diameter propeller emergence risk for a vessel in waves. In: Proceedings of the 8th International Conference on Computational Methods in Marine Engineering (MARINE 2019). Gothenburg, Sweden, pp. 634–645. doi:10.5281/zenodo.2650219.

Nomenclature

$1+k$	Form factor $(-)$
$\bar{R}_F$	Mean frictional resistance in regular waves (N)
$\bar{R}_W$	Mean wave making resistance in regular waves (N)
$\bar{S}$	Mean wetted surface area in regular waves (m^2)
$\bar{T}$	Mean measured thrust in free-sailing self-propulsion model tests in regular waves (N)
$\bar{V}$ or $\bar{U}$	Mean measured speed in free-sailing self-propulsion model tests in regular waves (m/s)
Δt	Time step size (s)
Δ	Mass displacement (kg)
λ	Wave length (m)
λ_0	Fundamental wave length (m)
μ	Heading angle (deg)
∇	Volume displacement (m^3)
ν	Kinematic viscosity of water (m^2/s)
ω	Circular wave frequency (rad/s)
ω_E	Circular wave frequency of encounter (rad/s)
ϕ	Velocity potential (m^2/s)
ρ	Water density (kg/m^3)
θ	Calm water trim (deg)
θ_i	The ith harmonic amplitude of pitch motion response in regular waves (deg)
$\theta_{\varepsilon i}$	The ith harmonic phase of pitch motion response in regular waves (rad) or (deg)
$\vec{\omega}_h$	Angular velocity vector of the hull
$\vec{n}$	Unit normal vector of the hull surface pointing into the fluid domain
$\vec{p}_p$	Position vector of a particle on free surface
$\vec{r}_h$	Radius vector from the hull center of rotation
$\vec{u}_h$	Linear velocity vector of the hull
A	Wave amplitude $H/2$ (m)
A_i	The ith harmonic amplitude of measured wave height in self-propulsion model tests in regular waves (m)
$A_{\varepsilon i}$	The ith harmonic phase of measured wave height in self-propulsion model tests in regular waves (rad) or (deg)
B	Breadth at mid-ship (m)
C_B	Block coefficient $(-)$
C_F	Frictional resistance coefficient in the ITTC-57 model-ship correlation line $(-)$
C_{AW}	Added wave resistance coefficient $(-)$
F_{Tow}	Longitudinal towing force in model tests (N)
Fr	Froude number $(-)$
g	Gravitational acceleration (m/s^2)
H	Wave height (m)
k	Wave number (rad/m)
K_{yy}	Mass radius of gyration around Y-axis (m)
L	Length between perpendiculars (m)
L_{CG}	Longitudinal position of center of gravity from aft perpendicular (m)
p	Unsteady hydrodynamic pressure (N/m^2)
p_a	Atmospheric pressure (Pa)
r	Response in regular waves
R_F	Frictional resistance in calm water (N)
r_i	The ith harmonic amplitude of ship response in regular waves

R_T	Total resistance in calm water (N)
R_V	Viscous resistance in calm water (N)
R_W	Wave making resistance in calm water (N)
$r_{\varepsilon i}$	The ith harmonic phase of ship response in regular waves (rad) or (deg)
R_{Wi}	The ith harmonic amplitude of wave making resistance in regular waves (N)
Re	Reynolds number $(-)$
S	Bare hull wetted surface area at rest (m^2)
S_h	Instantaneous hull wetted surface area in the FNPF computations (m^2)
S_i	The ith harmonic amplitude of wetted surface area in regular waves (m^2)
S_{wet}	Wetted surface area at rest in the respective model test; bare hull plus rudder or all appendages (m^2)
T	Measured thrust in free-sailing self-propulsion model tests in calm water (N)
t	Time (s)
T_A	Draft at aft perpendicular (m)
t_d	Thrust deduction factor $(-)$
T_E	Wave encounter period (s)
T_F	Draft at fore perpendicular (m)
T_z	Heave natural period (s)
T_θ	Pitch natural period (s)
V	Forward velocity (m/s)
V_{CG}	Vertical position of center of gravity from keel (m)
x_d	Computational domain length from fore perpendicular (m)
x_i	The ith harmonic amplitude of surge motion response in regular waves (m)
y_d	Computational domain half breadth (m)
z	Calm water sinkage (m)
z_i	The ith harmonic amplitude of heave motion response in regular waves (m)
Z_p	Vertical position of a point with respect to the undisturbed free surface (m)
$z_{\varepsilon i}$	The ith harmonic phase of heave motion response in regular waves (rad) or (deg)
u	Axial velocity component of ship wake
v	Tangential Y velocity component of ship wake (tangential to the plane of study in which axial velocity component is defined on)
w	Tangential Z velocity component of ship wake (tangential to the plane of study in which axial velocity component is defined on)

Contents

1

Introduction

Although shipping is the most efficient and cost-effective mode of cargo transportation, maritime transport still considered as a rather large source of greenhouse gas emissions worldwide. Increasing environmental societal awareness and concerns, and strict international regulations regarding emissions from shipping to marine and atmospheric environment, stimulate further technological developments and energy efficiency improvements in marine industry. Reducing ships operational power is one of the main measures which is also motivated by ship owners to reduce their fleet fuel consumption and costs. Therefore, the maritime community has been in the process of developing various concepts for optimizing ships to operate at their most efficient and economical operational point. However, application of such optimizations requires accurate and reliable predictions of ships required power in the design process. Unbalanced powering would adversely affect the energy/fuel consumption, hence increasing ships environmental impact. Therefore, prediction of the required operational power would be beneficial for the overall assessment of a ship performance.[1]

Traditionally, ship performance in calm water has been the main research topic in ship hydrodynamics. However, calm water is rather an exception during an actual voyage. Ships may experience involuntary/voluntary speed loss when they operate in a more realistic environmental condition than calm water. Various factors responsible for the loss of speed in a seaway are mentioned by Bhattacharyya (1978) as added resistance due to waves, wind and ship motions, loss of propulsive efficiency (related to propeller overload and variation of wake into the propeller due to motions, speed loss, propeller ventilation/emergence and the change of propulsion system and machinery) as well as voluntary reduction of engine speed for preventing green water, slamming, excessive

[1] Parts of the text in this chapter is published in "Irannezhad, M., Eslamdoost A., Kjellberg M., and Bensow, R. E. (2022). Investigation of ship responses in regular head waves through a Fully Nonlinear Potential Flow approach. *Ocean Engineering* **246**, 110410. `issn`: 0029-8018. `doi`:10.1016/j.oceaneng.2021.110410." Copyright Elsevier (2022).

accelerations, propeller racing or course keeping. Therefore, ship designers consider an additional experience-based reserved power of 10-15%, called "sea margin" ITTC (2017a), to ensure a reliable performance of ships in other environmental conditions than calm water. Although this approach has been proven to be suitable for power predictions over the years for a very large number of vessels, it introduces a drawback that the ships may rarely confront such conditions which may lead to underpower/overpower situations. Today, there is a trend towards ship design optimization in operational conditions closer to near-service conditions than calm water.

Waves are playing a significant role in affecting most of the aforementioned factors responsible for the ships speed loss. A seaway may contain waves with various heights and lengths propagating in different directions. Operating in waves may have several effects on ship behavior. The interactions between waves, hull and the propulsion system of a ship may significantly affect the ship motions, resistance, wake and propeller load in comparison to calm water operational conditions. Added resistance due to waves for a ship operating in real sea conditions affects its required engine power in comparison to calm water conditions, which may lead to a noticeable ship performance degradation. Furthermore, large amplitude ship motions in a rough sea may adversely affect the ship structural integrity and harm the crew and cargo. Therefore, ship performance prediction in waves is crucial, especially in the early stages of the ship design process.

Ship performance in waves has been widely investigated experimentally and numerically. However, it is practically impossible to take all of the entailed physics into consideration. Hence, a series of assumptions and simplifications are often introduced in such methods. Different experimental and numerical methods can be utilized for prediction of ship performance in waves. For instance, the performance can be predicted experimentally through Captive or Free-Sailing (Free-Running) tests in towing tanks or seakeeping basins, ITTC (2018). Although these model tests are expensive and time-consuming, the ship's added resistance and motions are expected to be predicted with a high level of accuracy from the measured motions and towing force (or propeller thrust). On the other hand, since 1950s, computational seakeeping methods have started to evolve. Each method has different level of fidelity with respect to its computational costs and accuracy. Generally, the approach in these methods is based on either Potential Flow methods (Strip Theory or Three-Dimensional Panel Methods) or Computational Fluid Dynamics (CFD) techniques. Bertram (2012) has presented a structured overview of the most well-known ship performance prediction methods.

Usually, potential flow solvers are computationally much faster than CFD solvers. In potential flow methods, the flow is assumed to be inviscid, incompressible and irrotational. In reality, viscous effects can be significant in seakeeping, especially if the boundary layer separates periodically from the hull, e.g., in the case of roll and yaw motions, Bertram (2012). However, in the cases where the viscous effects are insignificant, application of potential flow methods may provide a great advantage in terms of computational efficiency. One of such scenarios is studying a ship performance in head waves in which the main ship motion responses are surge, heave and pitch which are found to be less affected by viscosity. Moreover, in potential flow solvers based on panel methods, only the boundaries are required to be discretized, not the whole fluid domain. This considerably reduces the effort needed for grid generation; however, the simple and continuous free surface defined

in potential flow solvers is not capable of modeling wave breaking, splashes or viscous phenomena or accurately predict the flow behind the transom. Generally, empirical treatments for inclusion of viscous effects can play a complementary role in these methods. Contrary to potential flow methods, the state-of-the-art CFD methods have the advantage of predicting ship hydrodynamic responses more accurately by performing high fidelity nonlinear computations with fewer simplifications related to the flow physics. However, these methods are computationally expensive and time-consuming. Therefore, based on the specific problem under study and the level of complexities required, one should choose a suitable numerical method for the ship performance prediction.

1.1 Motivation and Objectives

Today, with the development of advanced computational tools and availability of large computational resources, the numerical investigations of ship performance in more realistic environmental conditions than calm water are gradually gaining more popularity. For a full analysis of ship performance in a seaway, a broad range of environmental and operational conditions have to be considered. However, the ship hydrodynamic responses in such conditions may be subject to various correlated factors originating from the interaction effects between different ship components (e.g., hull, propeller, rudder and engine) in such environmental and operational conditions. This turns the analysis of ship responses to an extremely cumbersome, if not impossible, task. Therefore, it is often practical to first assume higher levels of simplifications and approximations for the problem under study and thereafter, step by step, increase the complexity of the problem. In this way, the effects of various factors can be initially studied in a rather isolated way, hence transforming the analysis of their interaction effects to a more feasible task.

This is the main motivation in this thesis, to perform numerical investigations of ship responses in calm water and regular head waves and perform a detailed analysis of the correlations between different responses as well as their effects on the ship behavior. Such studies may provide clearer understanding of the ship performance in a more realistic condition which may be beneficial for ship/propeller designers to optimize their designs or introduce new technological solutions, hence helping marine industry in different environmental, economical and safety related aspects.

The first level of simplifications applied in this thesis is the consideration of ship performance only in calm water and regular head waves. Although the ships in a real seaway may be subjected to irregular waves and ship heading other than head waves, the regular head waves are found to be a proper candidate for the initial stages of investigations due to their relatively less complicated effects on the ship performance. Through comparison of the ship behavior in regular head waves to that of calm water, the effects of such waves on the ship hydrodynamic responses can be examined.

The second level of simplifications applied in this thesis is to consider only the bare hull in model-scale operating in calm water and regular head waves. The appendages in a fully-appended ship may add complexity to the flow physics and thus the analysis of the ship performance. After understanding a bare hull performance in waves further complexities can be progressively elaborated for the combination of various ship components.

The third level of simplifications applied in this thesis is to consider only a set of selective operational points of the ship, i.e., advance velocities, loading conditions, environmental and wave conditions. Through analyzing the ship performance at such operational points, a general overview of the physical aspects for different contributing factors can be obtained which can be extended to other operational points.

The eventual objective of this research is to study the propeller-hull interaction effects in calm water and regular head waves. In order to accomplish such a comprehensive goal, first in the present licentiate thesis, the bare hull is investigated and the studies on the propeller-appended hull are planned to be carried out in the next step towards a doctoral thesis using the base knowledge gained in the current study. That said, the main objective of this licentiate thesis is to perform numerical investigations and analysis of the ship hydrodynamic responses and their correlations for the bare hull in model-scale operating in calm water and regular head waves.

1.2 Method

For studying ship bare hull hydrodynamic responses in regular head waves, the utilization of a potential flow method may be beneficial, enabling investigation of a broader range of operating conditions due to its lower computational demand. Then, the results of such studies can be used for understanding the overall behavior of the ship in regular head waves and eventually help with selecting more critical operational conditions to be studied in more detail using higher fidelity CFD solvers. Therefore, these two methods are employed for the investigations carried out in this thesis. Before analyzing the ship hydrodynamic responses using the achieved numerical results, comprehensive validation of the employed numerical tools are carried out using a collection of experimental data. Moreover, in order to examine the uncertainties involved in the computations performed in the CFD solvers, an extensive verification study is carried out. In this thesis, the main focus of the uncertainty analyses is on systematic grid convergence study.

1.3 Outline

This thesis consists of a brief review of the literature on the use of numerical methods in ship hydrodynamics, followed by a general explanation of the employed CFD and potential flow methods and extensive evaluation of these methods on two different vessels. For each vessel, more specific explanations of the vessel geometrical characteristics, operational conditions and available experimental data as well as the details of the applied numerical methods are provided. The results of such method applications are analyzed and the concluding remarks are presented. Finally, the thesis is concluded with a summary of learnings from the application of these methods as well as potential future work.

On the one hand, an extensive application of a potential flow method as well as some applications of a viscous flow method are considered for a general cargo vessel. The main objective concerns the analysis of ship motion and resistance responses in waves, while the ship nominal wake is also briefly analyzed through a set of viscous flow simulations. On the other hand, a more comprehensive viscous flow analysis is carried out for a tanker

ship concerning detailed analyses of the ship responses in waves and their effects on the ship nominal wake.

A more compact version of the investigations carried out by potential flow simulations can be found in the published article Irannezhad et al. (2022). However, only limited parts of the studies from the viscous flow analysis has already been published in Irannezhad et al. (2021, 2019a,b).

2

Numerical Methods

In order to predict the ship responses using numerical methods, the physics of the flow around the hull should be studied. However, it is practically impossible to take all of the entailed physics into consideration. Hence, a series of assumptions and simplifications are often introduced in numerical methods. Therefore, there exist a wide range of numerical methods with different levels of simplifications and assumptions, all being suitable for specific problems in ship hydrodynamics.

The governing equations of a Newtonian fluid flow are the so called Continuity and Navier-Stokes equations, both simply called Navier-Stokes equations henceforth. These equations are a set of non-linear partial differential equations derived from the basic laws of mass, momentum and energy conservation. These complex mathematical equations can be solved numerically. Often, discretization methods are used to convert the continuous system of equations to a set of discrete algebraic equations, which then can be solved using numerical techniques. In this chapter, the general information about the employed numerical methods and the levels of approximations and simplifications introduced in such methods as well as their governing equations are provided. The details about the implementation of each method and the specific numerical setups are given in Chapters 4 and 5.

2.1 Viscous Flow Methods

Generally, the starting point of simplifications introduced in numerical methods in ship hydrodynamics is the assumption of considering incompressible, constant density and viscous flow for the fluids involved. The Navier-Stokes equations of incompressible viscous flow for Newtonian fluids in three dimensions can be expressed as,

$$\frac{\partial U_i}{\partial x_i} = 0,$$

$$\frac{\partial U_i}{\partial t} + U_j \frac{\partial U_i}{\partial x_j} = -\frac{1}{\rho}\frac{\partial P}{\partial x_i} + \nu \frac{\partial^2 U_i}{\partial x_j \partial x_j} + g_i, \tag{2.1}$$

in which i and j represent the coordinates, U_i is the i^{th} component of the velocity vector U, t is time, ρ is the density, P is the pressure, ν is the kinematic viscosity of the fluid and g_i is the gravitational acceleration which is assumed to be the only existing body force.

Fluid flows can be divided into two different types of laminar and turbulent flow regimes. Laminar flow occurs when the fluid flows in infinitesimal parallel layers with no eddies or swirls. On the other hand, the turbulent flow is three dimensional, irregular, diffusive and dissipative consisting of eddies (turbulent structures) with different sizes. The flow around a ship is turbulent. However, for analyzing the global ship responses such as motions and loads, resolving completely even the smallest turbulent structures in the flow is not required as their influence on the ship responses are insignificant. Considering this, more simplifications can be introduced into the governing equations to model turbulence instead of resolving it. A broad variety of turbulence models has been developed, while here, only the one which is mostly used in ship hydrodynamics context is explained and briefly compared with some other ones.

2.1.1 Turbulence Modeling

The turbulent flow may be averaged over a time scale just large enough to effectively filter out the turbulent structures. This procedure is called Reynolds decomposition. The velocity and the pressure in the Navier-Stokes equations can then be decomposed into an averaged and a fluctuating quantities as,

$$U_i = \overline{U_i} + u_i,$$

$$P = \overline{P} + p, \tag{2.2}$$

in which the term $\overline{U_i}$ is the time-averaged component of the velocity in i-direction and the term u_i is the fluctuating velocity component. The Reynolds Averaged Navier-Stokes (RANS) equation are derived by inserting the Reynolds decomposition into the Navier-Stokes equations as,

$$\frac{\partial \overline{U_i}}{\partial x_i} = 0,$$

$$\frac{\partial \overline{U_i}}{\partial t} + \overline{U_j}\frac{\partial \overline{U_i}}{\partial x_j} = -\frac{1}{\rho}\frac{\partial \overline{P}}{\partial x_i} + \nu \frac{\partial^2 \overline{U_i}}{\partial x_j \partial x_j} + g_i - \frac{\partial \overline{u_i u_j}}{\partial x_j}, \tag{2.3}$$

which is similar to the original equations but with an extra term $\overline{u_i u_j}$ called Reynolds Stress Tensor. Mostly, the partial differential equations of a mathematical model are not a closed set, meaning that the number of unknowns quantities exceeds the number of equations. To provide closure, additional equations are introduced to the mathematical models. These additional equations called constitutive equations. In the RANS category, there are two common approaches for modeling the Reynolds Stress Tensor to provide the closure equation, i.e., Reynolds Stress Transport models and Eddy Viscosity models.

In Reynolds Stress Transport models, the components of the Reynolds Stress Tensor are directly calculated by solving their governing transport equations. Therefore, an extra transport equation should be solved for each component which increases the computational demands. On the other hand, the Reynolds Stress Tensor in Eddy Viscosity models can be represented in terms of the mean flow quantities. A well-known model is the Boussinesq approximation in which Reynolds Stress Tensor is assumed to be proportional to the mean strain rate tensor. The original Boussinesq approximation implies a linear constitutive relation as,

$$-\overline{u_i u_j} = \nu_t(\frac{\partial \overline{U_i}}{\partial x_j} + \frac{\partial \overline{U_j}}{\partial x_i}) - \frac{2}{3}k\delta_{ij}, \tag{2.4}$$

in which ν_t is the turbulent viscosity, δ_{ij} is the Kronecker delta and k is the turbulent kinetic energy. The turbulent viscosity as the factor of proportionality can be derived by solving additional transport equations for extra scalar quantities. The most common turbulence models in ship hydrodynamics are different variants of k-ϵ and k-ω models as well as a hybrid form of them k-ω SST (Shear Stress Transport). These models are considered as two-equation models that solve transport equations for turbulent kinetic energy k and turbulent dissipation rate ϵ or specific dissipation rate ω. For more theoretical information about these models and their implementations in STAR-CCM+ read its User Guide. For the viscous flow simulations in Chapter 5, different turbulence models are employed that will be discussed later.

Contrary to time-averaging the turbulent flow as in RANS turbulence models, a spatial-filtering can be performed so that turbulent structures can be resolved down to a certain scale and modeled below this threshold. Therefore, larger turbulence structures with more significant effects on the flow will be resolved and smaller scale structures with lower effects can be modeled. This approach is called Large Eddy simulations (LES) which in comparison to RANS based turbulence models, resolve larger range of eddy sizes and only model smaller eddies. Moreover, a hybrid technique called Detached Eddy Simulation (DES) can be used in which RANS and LES are combined. LES and DES require more number of cells to capture a larger range of eddy sizes and thus often demand more computational costs than RANS.

The viscous flow simulations in this thesis concerns only the RANS approach. In this method, the hull is assumed to be rigid, hence the hull flexibility and hydroelasticity as a result of fluid-structure interaction are not investigated.

2.2 Potential Flow Methods

Although detailed information can be investigated from a viscous flow solution of ship hydrodynamics, such methods have a drawback in the sense that they require rather large computational resources. For the occasions in which the detailed analysis of the flow is not of great importance, more simplifications and approximations can be introduced to the Navier-Stokes equations in order to reduce the required computational efforts.

Therefore, for the ship responses in which the viscous effects are less significant, the viscous term in the Navier-Stokes equations can be removed and these equations are now reduced to Euler equations. Solving the Euler equations are still computationally expensive, thus another assumption about the flow being irrotational can be adopted for further simplification of the governing equations. An incompressible, inviscid and irrotational flow is called potential flow. The governing equation for potential flow is then simplified into Laplace's equation, $\nabla^2\phi = 0$, where ϕ is a scalar quantity referred as velocity potential.

In potential flow methods, the Laplace equation is solved in conjunction with considerations of appropriate ship hull and free surface boundary conditions. Potential flow methods are often classified based on the levels of nonlinearities applied to these boundary conditions. These methods, based on ITTC (2017b) categorization, include linear potential flow methods, Froude-Krylov nonlinear methods (weakly nonlinear methods), body exact methods (or weak scatterer methods) and fully nonlinear methods. In linear potential flow methods, the linearized boundary conditions are represented in terms of the mean free surface and wetted surface area. Then the solution of the Boundary Value Problem (BVP) is a superposition of different potential components (steady, incident wave, radiation and diffraction). Linear potential flow methods are often fast, efficient, robust and easy to use in a practical sense. Another advantage of using linear potential flow methods is the possibility of solving the problem in frequency domain, which offers a very low computational cost in comparison to the unsteady methods. In weakly nonlinear and body exact methods, nonlinearities are introduced to a certain extent in order to increase the solution accuracy. When the free surface boundary conditions are applied without any simplifications or approximations, it is commonly referred as Fully Nonlinear Potential Flow (FNPF) method. In this thesis, an FNPF approach is employed for studying the ship responses using potential flow methods in Chapter 4.[1]

The FNPF methods represent the category of potential flow methods with the least amount of approximations to the potential flow and the interactions between the ship hull and the fluid. The term "Fully Nonlinear" in such methods should not be confused with the Fully Nonlinear viscous flow methods indicated in the taxonomy of hydrodynamic solutions explained by Hirdaris et al. (2016), as the FNPF methods are counted as potential flow methods and hence, the nonlinear phenomena associated with the fluid in the form of viscosity are neglected. In these methods, the aspects of violent flow incidences, such as slamming, is not considered. The FNPF methods fall into the category

[1] Parts of the text in this chapter is published in "Irannezhad, M., Eslamdoost A., Kjellberg M., and Bensow, R. E. (2022). Investigation of ship responses in regular head waves through a Fully Nonlinear Potential Flow approach. *Ocean Engineering* **246**, 110410. `issn`: 0029-8018. `doi`:10.1016/j.oceaneng.2021.110410." Copyright Elsevier (2022).

of "Smooth Waves" in the aforementioned taxonomy which fill the gap between the partially nonlinear potential flow and fully nonlinear viscous flow methods. Moreover, it is assumed that the waves are "smooth" in the FNPF methods, therefore, wave breaking or fragmentation of the fluid domain (e.g., green water on deck) can not be modeled in such methods. Furthermore, in the current FNPF method, the hull is assumed to be rigid, hence the hull flexibility and hydroelasticity as a result of fluid-structure interaction are not investigated.

3

Literature Review

In this chapter, a brief literature review is provided for the usage of FNPF and RANS methods in the ship performance prediction in calm water and regular head waves. It should be mentioned that this review does not completely cover the works performed in this context, but rather gives a general information about the application of these numerical methods in maritime community.

It should be noted that the numerical methods for solving problems in ship hydrodynamics were first introduced in 1950s using simpler methods (e.g., linear potential flow methods) and later with a more availability of computational resources more sophisticated methods (e.g., RANS) have been developed and used. The computational costs involved in FNPF methods are higher than the simpler methods, but significantly lower than the viscous flow methods. More information about the employed FNPF method and the simulation setups are discussed in Section 4.3. On the other hand, the simulation setups used for the employed RANS method are discussed in Chapter 5.

Although there are several FNPF methods developed in recent years, there are not extensive publications available on the application of these methods for investigation of ship hydrodynamic responses in waves in a wide range of operational and environmental conditions incorporating a detailed analysis of the responses. For instance, water waves are simulated by a fully nonlinear potential flow method developed by Engsig-Karup et al. (2009) which is further developed by Ducrozet et al. (2010) to study the wave-wave and wave-structure interactions for a fixed circular cylinder. A fully nonlinear potential flow method is developed by Mola et al. (2017) to evaluate the performances of different hulls in calm water. Coslovich et al. (2021) studied the KVLCC2 tanker motions and resistance responses in waves using an FNPF method focusing mainly on adaptive grid refinement and nonlinear decomposition of the velocity potential and wave field. There are also more publications available such as the ones presented in the extensive review paper by Hirdaris et al. (2014) as well as the studies by Zhang and Xu-Ning (2018) and Pacuraru et al. (2020). However, the characteristic difference which stands out in the

current work relative to these studies is the investigations of ship responses by a fully nonlinear unsteady three-dimensional potential flow solver, SHIPFLOW MOTIONS, in a broad range of operational and environmental conditions and the detailed analysis of the ship responses and their correlations. This leads to an evaluation of the capabilities of the employed FNPF method in this context.[1]

Added resistance is the time-average of the longitudinal force (in the opposite direction of movement) on a ship in waves minus the force in calm water at the same forward speed. It demonstrates higher order nature than motions, hence more difficult to be determined, Bertram (2016). The added resistance value is relatively small in comparison to the amplitude of the instantaneous wave exciting force, Faltinsen (1990), thus a high degree of accuracy is required for prediction of added resistance in both experiments and numerical computations, Sadat-Hosseini et al. (2013). Moreover, the dependency of added resistance on ship motions, ship speed, wave length, wave height, wave heading angle, hull form and bow shape makes its accurate prediction even more challenging, Wu (2013). Two major contributors to added resistance in waves are radiation from generated waves due to ship motions and diffraction and reflection of the incident wave. Fully nonlinear interaction between incident and radiated/diffracted waves is considered in the current FNPF method.

Two main analytical formulations for prediction of added resistance in potential flow methods are known as far-field method and near-field method, ITTC (2018). The far-field methods are based on conservation of energy and momentum. The first far-field method was introduced by Maruo (1957) and Maruo (1960). The method was further developed by Joosen (1966) as well as Newman (1967). Other far-field methods have also been developed by Gerritsma and Beukelman (1972) in which the added resistance was estimated based on the radiated energy method. The near-field methods are based on integration of hydrodynamic pressure on the hull surface. This method was first introduced by Havelock (1937) and further developed in Havelock (1942) based on the Froude-Krylov approach for calculation of wave induced pressure forces acting on the hull. Other examples of well-known near-field methods are presented in Boese (1970), Salvesen (1978) and Faltinsen et al. (1980). Most of the aforementioned methods are based on Strip Theory. Ship motions are playing a significant role in the formulation of these analytical methods. Therefore, ship motions are supposed to be estimated prior to the prediction of added resistance. In the Strip Theory, ship motions are generally obtained in frequency domain based on the Slender Body Theory. More advanced potential flow methods usually utilize free surface Green functions that satisfy the corresponding free surface boundary conditions, or Rankine sources, or a combination of them, ITTC (2017b). SHIPFLOW MOTIONS is a time-accurate three-dimensional potential flow solver using Rankine source distribution where both the free surface and hull are discretized. In this FNPF solver, the added resistance is computed based on a near-field method from the direct pressure integration on the hull wetted surface area. The rigid body motions equations are also solved.

[1] Parts of the text in this chapter is published in "Irannezhad, M., Eslamdoost A., Kjellberg M., and Bensow, R. E. (2022). Investigation of ship responses in regular head waves through a Fully Nonlinear Potential Flow approach. *Ocean Engineering* **246**, 110410. `issn`: 0029-8018. `doi`:10.1016/j.oceaneng.2021.110410." Copyright Elsevier (2022).

Since excessive wake variation in waves may have a significant impact on the propeller performance, it is important to study dynamics of the wake field for ships operating in waves. Although the propeller designers consider experienced-based margins for propellers operating in waves and off-design conditions, the knowledge of the wake field at different wave conditions for each specific hull could be beneficial in designing a more efficient propeller. This is one of the scenarios when the application of RANS methods is encouraged.

Optimizing propulsive efficiency of ships operating in more realistic environmental conditions than calm water has been gaining more attention recently. Such optimization concepts can be investigated in RANS methods. The effects of waves on propeller performance using RANS approaches have been investigated by different researchers such as Taskar et al. (2016) who studied different influencing factors in terms of cavitation, pressure pulses and efficiency on propeller performance of KVLCC2. Moreover, Sigmund (2019) in his PhD thesis performed an extensive and systematic investigations of the ship performance in regular and irregular waves using a RANS method in which the effects of different factors on the ship responses are studied. Regener (2016) also studied the propulsive factors in self-propulsion simulations using a hybrid RANS-BEM approach. Before the full analysis of propeller-hull interaction effects in waves, often the bare hull performance in waves is analyzed.

An extensive number of publications are available for application of RANS methods for the investigations of ships bare hull hydrodynamic responses in calm water and waves. For instance, Guo et al. (2012) used the RANS method to predict the wave-induced motions and added resistance for KVLCC2 in head waves. Wu (2013) calculated the added resistance for KVLCC2 in head short and long waves by RANS methods. Kim et al. (2017) used the validated results of an application of a RANS method for a ship hydrodynamic performance to study speed loss in waves. Lee et al. (2019a) used a RANS method to calculate the added resistance and propeller wake. Yao et al. (2020) numerically predicted added resistance and ship motion of KVLCC2 by using a RANS method in which the effects of wavelength, wave amplitude and the scales of the ship model on the results were analyzed.

One of the main points missing in some of the available investigations in literature regarding the usage of RANS methods for prediction of ship performance in wave is the lack of a comprehensive prediction of numerical uncertainty for the applied RANS methods. On the other hand, some of the studies involve a grid convergence study, however, there is not enough information available about the grids geometrical similarity which is one of the most important requirements for such studies,. Moreover, most of the uncertainty analyses are preformed for the global variables in ship hydrodynamic responses such as motions and resistance and the grid convergence study is not well carried out for wake predictions in literature.

4

Potential Flow Simulations

In this chapter, the hydrodynamic performance of a ship in terms of motions and resistance responses in calm water and in regular head waves is investigated using a Fully Nonlinear Potential Flow (FNPF) panel method. The investigations using the FNPF method are carried out for two loading conditions in a broad range of operational conditions. Comprehensive analyses of the motions and their correlation with the wave making resistance including their harmonics in waves are presented and compared against experimental data.[1]

The main objective of investigations in this chapter is to study the hydrodynamic performance of a vessel in terms of resistance and motion responses in a range of operational conditions by an FNPF method, and compare the results against experimental data. For comparison, the added wave resistance is also computed with a design tool by Martinsen (2016), through linear interpolations from an added resistance transfer function database. This database has been created by combining radiated energy method and the near-field asymptotic approach for different geometries in a range of Froude numbers and heading angles. The vessel under investigation in this chapter is a general cargo vessel developed in LeanShips[2], which is designed with a "tunnel-shaped" aft configuration meant to accommodate a Large Diameter Propeller (LDP). The concept of transforming a ship conventional-sized propeller to an LDP was introduced in order to improve the vessel propulsive efficiency; however, the LDP vessel peculiarities regarding its design and efficiency characteristics are not taken into consideration as part of this study objectives.

[1] This chapter is published in "Irannezhad, M., Eslamdoost A., Kjellberg M., and Bensow, R. E. (2022). Investigation of ship responses in regular head waves through a Fully Nonlinear Potential Flow approach. *Ocean Engineering* **246**, 110410. `issn`: 0029-8018. `doi`:10.1016/j.oceaneng.2021.110410." Copyright Elsevier (2022).

[2] Low Energy And Near to zero emissions Ships (LeanShips), is an EU-funded project, 2015-2019. More information about Large Diameter Propeller demo case can be found in https://www.leanships-project.eu/demo-cases/demo-case-09/overview.

4.1 Vessel Geometry and Operational Conditions

The LDP vessel main particulars in model-scale and in two loading conditions are given in Table 4.1. In this study, the hydrodynamic performance of the vessel operating in fresh water with the density of $\rho = 998.3\ kg/m^3$ and the kinematic viscosity of $\nu = 1.018 \times 10^{-6}\ m^2/s$ is investigated at different advancing speeds presented in Table 4.2.

Table 4.1: Model-scale LDP vessel main particulars (scale factor = 27).

Symbol	**Loading Conditions**		**Unit**	**Denotation**
	Full	**Ballast**		
L	7.95		(m)	Length between perpendiculars
B	0.88		(m)	Breadth at mid-ship
T_F	0.296	0.118	(m)	Draft at fore perpendicular
T_A	0.296	0.259	(m)	Draft at aft perpendicular
∇	1.743	1.089	(m^3)	Volume displacement
Δ	1740	1087	(kg)	Mass displacement
S	10.24	8.46	(m^2)	Bare hull wetted surface area at rest
C_B	0.842	0.825	$(-)$	Block coefficient
L_{CG}	3.94	3.59	(m)	Longitudinal position of COG from aft perpendicular
V_{CG}	0.344	0.258	(m)	Vertical position of COG from Keel
K_{yy}	1.99	1.95	(m)	Mass radius of gyration around Y-axis (pitch)

Table 4.2: Vessel speeds in model-scale and the respective Froude numbers $Fr = V/\sqrt{gL}$.

Froude	$Fr\ (-)$	$V\ (m/s)$
Fr_0	0.00	0.01
Fr_1	0.09	0.79
Fr_2	0.10	0.89
Fr_3	0.11	0.99
Fr_4	0.13	1.19
Fr_5	0.16	1.39
Fr_6	0.18	1.58

An earth-fixed coordinate system as well as a ship-fixed coordinate system are used. The earth-fixed Cartesian coordinate system in considered to be located at the initial mean free surface with X-axis pointing from the ship's bow towards its stern and Z-axis pointing upwards. The ship-fixed Cartesian coordinate system is located at the vessel Center of Gravity (COG) with X-axis pointing astern and Z-axis pointing upwards. Consequently, positive surge motion occurs when the COG moves in the opposite direction of the ship's forward speed. Positive heave motion is defined as when the COG moves upwards and positive pitch motion is defined as when the ship's bow moves upwards (or stern moves downwards).

The investigations are mainly concerned with the vessel in deep water subjected to regular head waves, however, the vessel performance in calm water is also presented. An overview of the operational conditions in regular head waves is presented in Table 4.3 in which wave heights H and wave lengths λ are non-dimensionalized by the ship length

L. Each of these operating conditions are labeled with a code which are used later as plot legends in Section 4.5. Prior to the model tests, it was predicted that propeller ventilation/emergence may occur frequently for the LDP due to its proximity to the free surface. Since one of the goals of the experiments was the ventilation risk assessment, ballast condition (with a lower draft at the aft perpendicular and hence higher risk of ventilation) was studied more in detail in the measurements.

Table 4.3: Operational conditions in regular head waves. Non-dimensional wave lengths λ/L in **bold** text are representing equivalent conditions in both self-propulsion model tests (SP EFD) and Fully Nonlinear Potential Flow computations (FNPF).

Loading Conditions	Fr $(-)$	H/L $(-)$	**Condition Label**	λ/L $(-)$	
				SP EFD	**FNPF**
Full	0.10	0.014	$Fr_2 - H_2$	**0.28**	**0.28**, 0.55, 0.70, 0.79, 0.91, 1.06, 1.24
		0.028	$Fr_2 - H_4$	**0.70**, **0.79**, **0.91**, **1.06**, **1.24**	0.28, 0.40, 0.51, 0.55, 0.61, **0.70**, **0.79**, **0.91**, **1.06**, **1.24**, 1.35, 1.53, 2.04
	0.18	0.014	$Fr_6 - H_2$	-	0.20, 0.28, 0.55, 0.70, 0.79, 0.91, 0.97, 1.06, 1.17, 1.24, 1.35, 1.53, 3.06
		0.028	$Fr_6 - H_4$	-	0.20, 0.28, 0.55, 0.70, 0.79, 0.83, 0.91, 0.97, 1.02, 1.06, 1.17, 1.24, 1.35, 1.53, 2.04, 3.06
Ballast	0.10	0.014	$Fr_2 - H_2$	**0.91**, **1.06**, **1.24**	0.37, 0.55, 0.70, 0.79, **0.91**, **1.06**, **1.24**, 1.35, 1.53
	0.13	0.007	$Fr_4 - H_1$	**0.79**, **1.06**, **1.24**	0.55, 0.70, **0.79**, 0.91, **1.06**, **1.24**, 1.35, 1.53
		0.014	$Fr_4 - H_2$	**0.28**, **0.37**, **0.49**, **0.55**, **0.70**, **0.79**, **0.91**, **1.06**, **1.24**	**0.28**, **0.37**, **0.49**, **0.55**, **0.70**, **0.79**, **0.91**, **1.06**, **1.24**, 1.35, 1.53
		0.021	$Fr_4 - H_3$	**0.79**, **1.06**, **1.24**	0.49, 0.70, **0.79**, **1.06**, **1.24**, 1.35, 1.53

4.2 Experimental Method

Experimental model tests in calm water and in regular head waves were performed by Maritime Research Institute Netherlands (MARIN). The wooden model is manufactured at MARIN. The calm water model tests were carried out at Fr_1, Fr_3, Fr_4, Fr_5 and Fr_6 in two different setups (rudder-equipped bare hull and self-propelled model) and the results for Fr_2 were interpolated. During the calm water tests, the model was free to heave and pitch. For the first setup, the resistance test was carried out based on towing the rudder-equipped bare hull by a towing carriage, in which the measured towing force is the vessel total resistance R_T. Based on the decomposition of resistance in ITTC-78 method mentioned by Larsson and Raven (2010), the total resistance is divided into a

viscous resistance component $R_V = (1+k)R_F$, which includes the form effect on friction and pressure, and a wave making resistance component R_W as,

$$R_T = (1+k)R_F + R_W. \tag{4.1}$$

The frictional resistance R_F can be computed from,

$$R_F = 0.5\rho S_{wet} V^2 C_F, \tag{4.2}$$

in which the wetted surface area at rest S_{wet} includes the wetted surface area of the configured rudder plus that of bare hull. The frictional resistance coefficient C_F can be computed from the ITTC-57 model-ship correlation line,

$$C_F = \frac{0.075}{(log\ Re - 2)^2}, \tag{4.3}$$

where $Re = VL/\nu$ is the Reynolds number. The calm water wave making resistance R_W then can be deduced from Equation 4.1 considering the experimentally and numerically (double-body viscous flow) obtained form factor of $1 + k = 1.167$. The resistance test results of the rudder-equipped bare hull are labeled as TOW EFD henceforth.

The calm water model tests were also carried out for the self-propelled model, in which the model was equipped with a propeller while it was unloaded by means of a tow force to compensate for the difference in viscous resistance between model-scale and full-scale. The calm water propeller thrust T, the towing force F_{tow} as well as the dynamic sinkage z and trim θ were measured from these tests. The calm water thrust deduction factor t_d at each respective loading condition and forward speed is then obtained from,

$$t_d = 1 - \frac{R_T - F_{Tow}}{T}, \tag{4.4}$$

where R_T is the measured total calm water resistance for the rudder-equipped bare hull. On the other hand, the model tests in regular head waves were carried out at the given Froude numbers in Table 4.3 solely in six Degrees of Freedom (6DOF) in free-sailing self-propelled and self-steered mode. The model acceleration/deceleration in the beginning/end of each run were performed using a towing system consisting four lines controlled under tension or slack by four remotely-operated winches. The model's six degrees of freedom and speed were measured by means of optical tracking systems at a sampling rate of 100 Hz. Thrust and torque were measured by strain gauge transducers at 4800 Hz sampling frequency. Moreover, wave elevation was measured by a resistance type wave probe at a sampling frequency of 200 Hz. The measured harmonic amplitudes and phases of the ship forward speed, ship motions, incident wave height and the propeller thrust were provided. The mean wave making resistance component in regular waves $\bar{R}_W$ is then deduced from the mean thrust in regular waves $\bar{T}$ as,

$$\bar{R}_W = (1 - t_d)\bar{T} - (1+k)\bar{R}_F, \tag{4.5}$$

in which t_d and $\bar{R}_F$ need special considerations. It is well-established that the propulsion factors such as wake fraction and thrust deduction for a ship operating in waves deviate from those of calm water, for instance by Gerritsma et al. (1961), Moor and

Murdey (1970) as well as Nakamura and Naito (1975). The deviation is more significant when the ship motions are severe. In the case of LDP vessel, the deviation might be even more pronounced because of the proximity of the propeller to free surface and hence high occurrence of propeller ventilation/emergence in severe conditions, associated with a sudden change in propeller thrust and torque. Due to the lack of knowledge about how exactly the propulsion factors change for the LDP vessel in waves, the thrust deduction factor in Equation 4.5 is assumed to be equal to the calm water t_d value at the same loading condition and forward speed. A similar assumption is considered by Taskar et al. (2016) and Valanto and Hong (2017) for studying the propulsion performance of KVLCC2 tanker and a cruise ship in waves, respectively. Block (1993) also mentioned that the thrust deduction factor obtained in calm water can be applied to the ships in moderate sea-states. Furthermore, since the model was running in free-sailing self-propulsion mode, the mean value of the measured speed $\bar{V}$ was not exactly equal to the expected V in Table 4.2. Therefore, a linear interpolation is used for estimation of the thrust deduction factor at the mean attained speed $\bar{V}$ in regular waves from the previously computed calm water t_d in Equation 4.4. Moreover, the Reynolds number in Equation 4.3 and accordingly C_F in Equation 4.2 are calculated for the mean attained speed $\bar{V}$ in each respective model test. $\bar{R}_F$ in waves is then calculated assuming the same wetted surface area and hence similar frictional resistance in waves as in calm water at each certain loading condition and forward speed. S_{wet} includes the wetted surface area of the bare hull and all other appendages presented in the self-propulsion model tests. The self-propulsion model tests results are labeled as SP EFD henceforth.

4.3 Potential Flow Method

A fully nonlinear unsteady three-dimensional potential flow solver SHIPFLOW MOTIONS (Version 6) is used for the numerical computations. The flow in potential flow methods is assumed to be homogeneous, inviscid, incompressible and irrotational. A scalar quantity referred as velocity potential ϕ of which satisfies Laplace's equation $\nabla^2\phi = 0$ is used to describe the flow. In FNPF methods, fully nonlinear kinematic and dynamic boundary conditions are applied on the free surface as,

$$\frac{D\vec{p}_p}{Dt} = \nabla\phi, \tag{4.6}$$

$$\frac{D\phi}{Dt} = -gZ_p + \frac{1}{2}\nabla\phi.\nabla\phi - \frac{P_a}{\rho}, \tag{4.7}$$

in Lagrangian frame where D is the material derivative ($\frac{D}{Dt} \equiv \frac{\partial}{\partial t} + \nabla\phi.\nabla$), $\vec{p}_p = (X_p, Y_p, Z_p)$ is the position of a particle on the free surface in the earth-fixed coordinate system, Z_p is the vertical position of the particle with respect to the undisturbed free surface and P_a is the atmospheric pressure. These equations are solved in the employed FNPF method without any linearization or simplifications, as opposed to the linear or partially nonlinear potential flow methods. Moreover, an impermeability condition is applied on the rigid hull surface taking into account the hull motions,

$$\frac{\partial \phi}{\partial n} = \vec{n}.(\vec{u}_h + \vec{\omega}_h \times \vec{r}_h), \tag{4.8}$$

where $\vec{n}$ is the unit normal vector of the hull surface pointing into the fluid domain, $\vec{u}_h$ and $\vec{\omega}_h$ are the linear and angular velocity vectors of the hull and $\vec{r}_h$ is the radius vector from the hull center of rotation. Impermeability condition is also applied on the bottom of the computational domain.

Then, the BVP (defined by the Laplace's equation and the boundary conditions) is solved using a Boundary Element Method (BEM). The hull surface and computational domain are discretized by means of flat quadrilateral panels assuming constant strength source distribution. Green Functions are used to obtain the source strength. The fully nonlinear free surface boundary conditions introduce a time dependency into the problem. Therefore, the free surface boundary conditions equations are integrated in time to evolve the free surface position and velocity potential using a Mixed Eulerian-Lagrangian (MEL) method in which each time step is divided into two sub-steps. Evolution of the free surface and velocity potential in time is tracked by markers associated at each panel. In the Eulerian sub-step, the boundary value problem is solved using the BEM and the velocity potential and the velocity of the free surface markers are obtained in the domain. In the Lagrangian sub-step, the boundary conditions are integrated in time and the free surface position and velocity potential are updated for the next time step.

In order to avoid unwanted wave reflections from the boundaries of the computational domain an artificial damping zone is introduced away from the hull. In this zone, the perturbed part of the solution is blended with the analytically described undisturbed wave field, hence matching the computed solution to the solution of the known wave field at the boundaries. Moreover, the FNPF method is not able to handle wave breaking and in the case of occurrence, the computations will stop immediately. Wave breaking is a natural phenomenon that occurs when waves become too steep, for instance it may be seen around the bow and stern of ships. In the current FNPF method, the waves that are about to break are identified and suppressed to prevent breaking, hence the smooth wave assumption is considered. The unsteady hydrodynamic pressure is calculated at any point in the domain from the unsteady Bernoulli equation,

$$p = -\rho \left(\frac{\partial \phi}{\partial t} + \frac{1}{2} |\nabla \phi|^2 + g Z_p \right), \tag{4.9}$$

in which the time derivative term is evaluated using a finite difference second order backward scheme. In this way, the nonlinear interactions between the diffracted and radiated wave components as well as the fully nonlinear incident wave field are implicitly taken into account. The hydrodynamic forces and moments acting on the body are computed by integration of the hydrodynamic pressure over all the surface elements dS of the wetted surface area of the hull S_h as,

$$\vec{F} = - \iint_{S_h} p \; \vec{n} \; dS, \tag{4.10}$$

$$\vec{M} = - \iint_{S_h} p \; (\vec{r_h} \; \times \; \vec{n}) \; dS. \tag{4.11}$$

Then the rigid body motions equations are solved representing the equilibrium between the inertial, gravitational and hydrodynamic forces and moments. For more details about this FNPF method and free surface modeling see Kjellberg (2013).

All of the FNPF simulations are carried out for the LDP vessel bare hull in 3 degrees of freedom (3DOF) where the hull is free to surge, heave and pitch, except in the 1DOF heave/pitch decay motions simulations. Calm water simulations are carried out at Fr_1 to Fr_6 to obtain the sinkage and trim as well as the calm water wave making resistance R_W. Moreover, decay motion simulations in calm water are performed at Fr_0, Fr_2 and Fr_6 in 1DOF as well as in 3DOF. Since the specification of zero ship velocity is not possible in the current FNPF solver, a minor velocity ($V = 0.01\ m/s$) is used in the simulations at Fr_0 (Table 4.2). The 5th order Stokes regular head waves with fuller troughs and sharper crests than airy (linear) waves are introduced at the inlet of the computational domain. These Stokes waves were found to be a better resemblance of the real-world waves, Fenton (1985). Other important computational specifications in the FNPF solver are discussed in the following sections.

4.3.1 Computational Domain

The size of computational domain is calculated based on the respective Froude number in each simulation. Taking advantage of a symmetry boundary condition, only half of the domain is considered in the simulations. The potential flow computations in SHIPFLOW MOTIONS are scale-independent, therefore, all the computations are carried out for the ship with unit length (i.e. geometry non-dimensionalized by the ship length). An overview of the computational domain is shown in Figure 4.1. The domain dimensions are defined as the normal distances to the ship fore perpendicular in which x_d/L and y_d/L are the boundaries edges in longitudinal and transverse directions, respectively. The domain is made wide enough to cover the Kelvin wedge over the considered domain length.

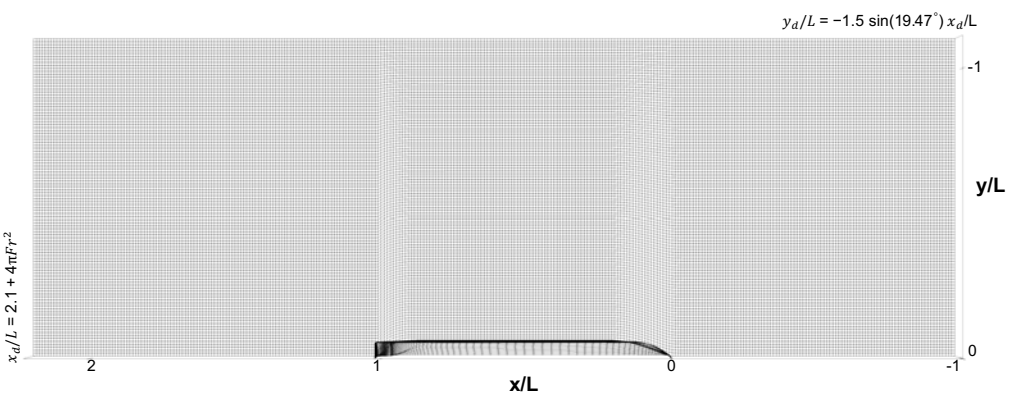

Figure 4.1: Computational domain overview.

4.3.2 Hull Discretization

In the FNPF method, the complete hull is discretized and remains body-fixed during the computations to allow for large variation of wetted surface. The hull discretization is done based on the best practices for hull panelization in potential flow methods in order to appropriately capture the form of the hull. The hull panel distribution is shown in Figure 4.2 where the non-dimensional distance from the fore perpendicular (x/L) is also shown. The number of panels on the half of the hull used in the FNPF simulations is 6747.

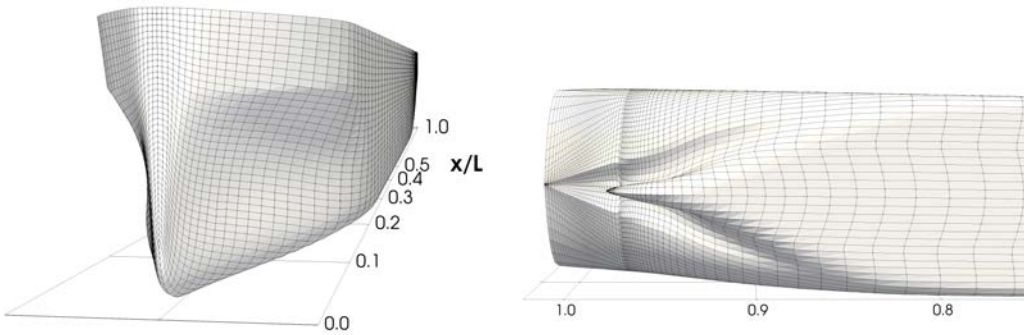

(a) Fore (b) Aft

Figure 4.2: Hull panelization overview.

4.3.3 Free Surface Discretization

In the current version of the FNPF solver the panelization on the free surface cannot be modified locally meaning that any modification of the free surface panel size results in change of the size of all panels everywhere in the domain. In order to keep the free surface panelization error as low as possible, a panel size sensitivity analysis has been carried out. These simulations are performed for an operational condition in regular head waves for the fully-loaded ship at Fr_2. Wave height $H/L = 0.028$ and wave length $\lambda/L = 0.79$ as well as the hull panelization presented in Section 4.3.2 remain the same in all of these simulations while uniformly refining the free surface panels. It is believed that the wave making resistance as well as the motion responses are fairly large for the selected case (Fully-loaded, $Fr_2 - H_4$ and $\lambda/L = 0.79$ in Table 4.3) which makes this case a suitable candidate for the free surface panelization study.

The results are post-processed based on the techniques explained in Section 4.3.7. The 0th harmonic amplitude of wave making resistance as well as the 1st harmonic amplitudes of heave z_1 and pitch θ_1 motions are shown in Figure 4.3. The wave making resistance clearly reaches an approximate convergence by increasing the number of panels on free surface. The convergence of heave and pitch motions are less pronounced since

the magnitudes of changes are very small for these motions. These results reveal that free surface panelization has a larger impact on the wave making resistance rather than the motions. The results obtained by the free surface panel distribution at Fr_2 and represented by 32754 panels are considered to be in the asymptotic range and thus the same panelization setup is used for the rest of the simulations in this work. The free surface panels for this case are shown in Figure 4.1. The panel size in both longitudinal and transverse directions is approximately 1% of the ship length. The total number of panels (including the hull panels) in half domain for Fr_1 to Fr_6 are approximately between 39000 and 47000.

In linear wave theory, the fundamental wave length generated by a ship at constant speed is $\lambda_0 = 2\pi Fr^2 L$ (notice that $L = 1$ in the current FNPF simulations as the ship is scaled based on its length). Due to very small Froude numbers in this study, the criterion of keeping the free surface panels smaller than 5% of the fundamental wave length suggested by Larsson and Raven (2010) would result in extremely small panels, hence very high computational costs. Therefore, this criterion is not fulfilled in this study.

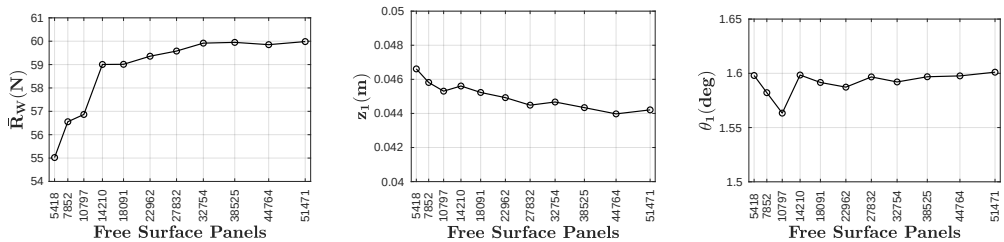

(a) Mean wave making resistance. (b) Heave 1st harmonic amplitude. (c) Pitch 1st harmonic amplitude.

Figure 4.3: Free surface panelization study of the fully-loaded ship at $Fr_2 - H_4$ and $\lambda/L = 0.79$.

4.3.4 Time Step Size

The computational time step size is determined to be a function of fundamental wave period $\sqrt{\lambda_0 2\pi/g}$. In the following simulations, 60 time steps per each wave period is used as the criterion for determining the time step size,

$$\Delta t = \frac{2\pi Fr\sqrt{L/g}}{60}, \tag{4.12}$$

in which $L = 1$ in the current FNPF simulations. Therefore, time step size becomes only a function of Froude number. In the case of approximately zero speed Fr_0, the time step size is computed based on $Fr = 0.05$.

4.3.5 Convergence Criteria and Computational Costs

The simulations in calm water is deemed converged when the standard deviation of the wave making resistance time history drops below 1% of its rolling tail-weighted root mean

square value (last 60% of the signal). The convergence criterion for simulations in waves is defined as when the standard deviation of the mean wave making resistance response signal drops below 1% of its root mean square value in the trailing last two encountered wave periods.

The simulations are carried out using parallel processing on multiple cores on a desktop workstation equipped with an Intel® Core™ i7-8700 CPU @ 3.20 GHz processor base frequency. The computational cost for an individual simulation in this work (using FNPF) is approximately 20 to 80 core-hours depending on the Froude number, incoming wave characteristics and other operational conditions. However, a viscous flow simulation in similar conditions may require two to three orders of magnitude higher computational cost in terms of core-hours based on the data presented by Irannezhad et al. (2019b) for the same hull in regular head waves using unsteady Reynolds-Averaged Navier-Stokes (RANS) simulations as well as by Larsson et al. (2014) and Hino et al. (2021) for different geometries using various viscous flow computations.

4.3.6 Design Tool for Estimating Added Wave Resistance

Added wave resistance of the LDP vessel is also estimated by a design tool developed at Technical University of Denmark (DTU) by Martinsen (2016). In this tool, added wave resistance was calculated for different combinations of geometries at various Froude numbers and heading angles to form a database. The added wave resistance in frequency domain was computed from Salvesen (1978) radiated energy method (5DOF Strip Theory) for long waves and Faltinsen et al. (1980) near-field asymptotic approach for short waves forming a continuous curve at their intersection. Then, five input parameters (L/B, B/Draft, C_B, Fr and heading angle μ) are used to carry out a linear interpolation within the validity range of the database to predict the added wave resistance, Martinsen (2016). Since it is not possible to assign different values for the fore and aft draft, the draft in ballast condition is considered as the averaged value, $(T_F + T_A)/2$. The computed added wave resistance from the design tool is labeled as TOOLBOX in the results.

4.3.7 Post-processing Techniques

In order to post-process the time-series of resistance and motions responses $r(t)$ computed in the simulations in waves, Fourier analysis is performed as,

$$r(t) = r_0 + r_1 cos(\omega_E t + r_{\varepsilon 1}) + r_2 cos(2\omega_E t + r_{\varepsilon 2}) + r_3 cos(3\omega_E t + r_{\varepsilon 3}) + ..., \quad (4.13)$$

where r_i is the ith harmonic amplitude of the response r, and $r_{\varepsilon i}$ is the phase component related to ith harmonic amplitude. The circular wave frequency of encounter ω_E is computed based on the circular wave frequency ω, ship velocity V and its heading angle μ as,

$$\omega_E = \omega - \frac{\omega^2 V}{g} \cos(\mu), \quad (4.14)$$

where $\mu = 180°$ for head waves. The wave encounter period T_E is then computed as $T_E = 2\pi/\omega_E$. The Fourier analysis is carried out over the last two encountered wave periods of the response signals when the simulation is converged, see Section 4.3.5. On the other hand, the Fourier analysis on experimental data was performed by MARIN and the harmonic amplitudes and phases of the ship forward speed, ship motions, incident wave height and propeller thrust were provided.

The ith harmonic amplitudes of surge and heave motions are non-dimensionalized by the wave amplitude (x_i/A and z_i/A). Pitch motion harmonic amplitudes are non-dimensionalized based on θ_i/kA in which θ_i is the pitch ith harmonic amplitude in radian and $k = 2\pi/\lambda$ is the wave number. The added wave resistance coefficient C_{AW} is computed from,

$$C_{AW} = \frac{\bar{R}_W - R_W}{\rho g B^2 A^2 / L}, \tag{4.15}$$

where $\bar{R}_W$ is the mean wave making resistance component in regular waves, R_W is the calm water wave making resistance, B is the ship breadth and A is the wave amplitude. As mentioned in Section 4.2, since the model tests in waves were carried out in free-sailing self-propulsion mode, the mean value of the measured speed $\bar{V}$ slightly deviated from the intended speeds in Table 4.2. Therefore, experimental $\bar{R}_W$ is calculated for the mean measured speed using Equation 4.5 with the aforementioned special considerations for t_d and $\bar{R}_F$, see Section 4.2. Moreover, calm water wave making resistance R_W at the mean measured speed $\bar{V}$ is obtained through interpolation of the measured calm water R_W at the speeds listed in Table 4.2.

Moreover, the incident wave height experienced by the ship is different in the measurements and computations. Although the incident wave height in the computations remains relatively close to the specified wave height at the inlet boundary, in the model tests the wave height experienced by the ship slightly varies from one test to another. The incident wave height in experiments was measured by a wave probe located approximately 2.4 m ahead of the fore perpendicular and 3.4 m towards the port side of the hull center plane. The Fourier analysis was performed on the measured wave height and the harmonic amplitudes and phases were provided. In order to calculate the experimental non-dimensional harmonic amplitudes of motions and C_{AW}, the experimental wave height $H(t)$ profile is expressed as,

$$H(t) = A_0 + A_1 cos(\omega_E t + A_{\varepsilon 1}) + A_2 cos(2\omega_E t + A_{\varepsilon 2}) + A_3 cos(3\omega_E t + A_{\varepsilon 3}), \tag{4.16}$$

where A_i and $A_{\varepsilon i}$ are the ith harmonic amplitude and phase of the measured wave height and ω_E is the wave encounter frequency based on the mean attained speed $\bar{V}$ in each respective model test. Then the experimental wave amplitude A is derived from,

$$A = \frac{H^{max} - H^{min}}{2}, \tag{4.17}$$

in which H^{max} and H^{min} are the maximum and minimum (peak and trough) values of the wave height profile in each respective model test.

4.4 Calm Water Results

The results of calm water wave making resistance, sinkage and trim are shown in Figure 4.4. A good agreement between the potential flow computed wave making resistance and the experimental data is seen in the fully-loaded condition, except an over-prediction at the highest Froude number and minor under-predictions at the lower Froude numbers. The under-prediction is more pronounced in the ballast condition over the whole range of Froude numbers, which also resulted in rather small negative values of resistance at the lower Froude numbers (these results are not shown in the plot). The wave making resistance is obtained from the integration of considerably large pressure values over the instantaneous wetted surface area of the hull. This increases the risk of error in the lower speed range where the total wave making resistance is small. Alternatively, far-field methods can be employed to overcome this issue. Generally, this kind of numerical errors in conjunction with the discretization errors, as seen in Section 4.3.2, as well as the potential flow simplifications and the use of empirical formulas, such as ITTC-57 skin friction line, are the main sources of discrepancy between the computed and the measured results. Moreover, the uncertainty related to the experimental data should not be forgotten. In order to be consistent in the computation of added wave resistance, the negative calm water wave making resistance values at the lower Froude numbers are considered to be zero.

The computed sinkage and trim and especially their trends at different Froude numbers are in a good agreement with the experimental data considering the very small values, see Figures 4.4b and 4.4c. It should be noted that the experimental data for sinkage and trim are related to the self-propulsion model tests (SP EFD), while only bare hull is considered in the FNPF simulations.

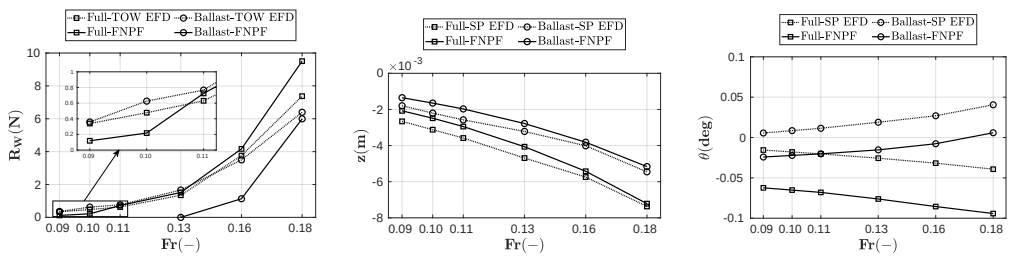

(a) Wave making resistance. (b) Sinkage. (c) Trim.

Figure 4.4: Comparison of the computed resistance, sinkage and trim with the measured values in calm water.

4.4.1 Decay Motions

Lewis (1989) noted that the most significant features of the heave and pitch Response Amplitude Operators (RAOs) to a large extent are dictated by their natural periods. In order to estimate the ship's natural periods of heave T_z and pitch T_θ motions, a

series of free heave and pitch decay motion simulations are performed in the fully-loaded condition at Fr_0, Fr_2 and Fr_6 in 1DOF and 3DOF, see Figure 4.5. The initial heave is approximately 0.08 m and the initial pitch is 3 deg for all of the cases. Besides, extra heave and pitch decay simulations are carried out at Fr_0 with 3DOF where the initial heave and pitch are set to approximately 0.12 m and 4 deg, respectively.

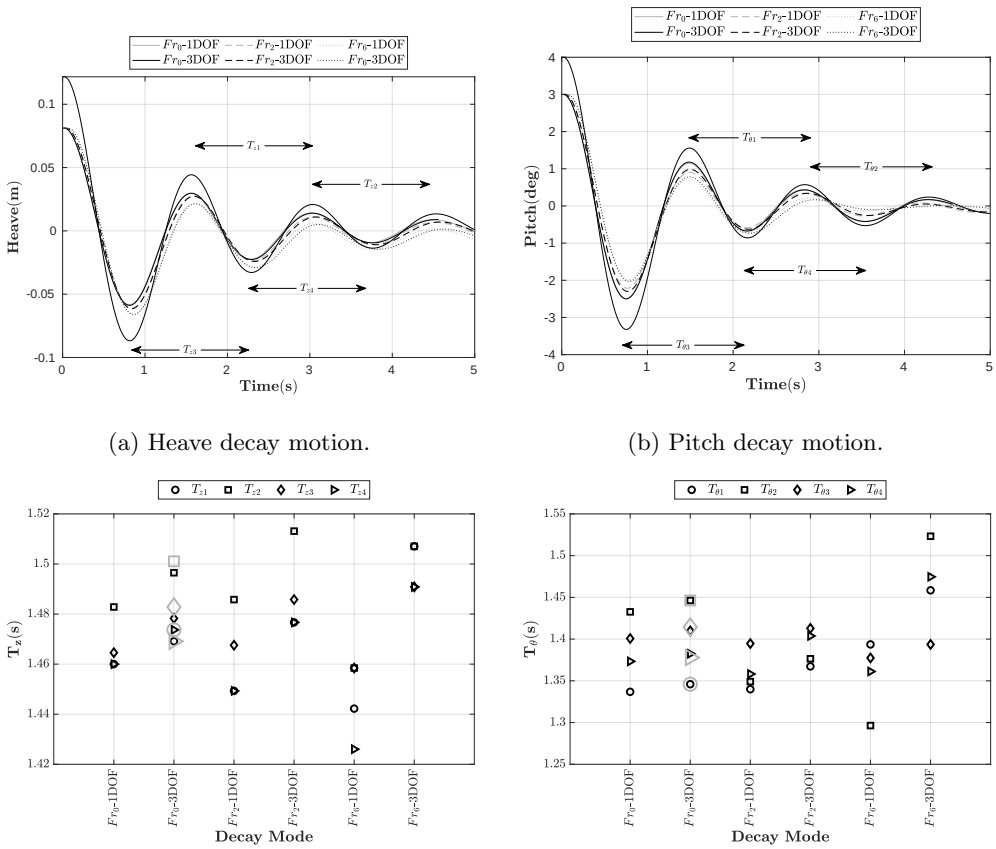

(a) Heave decay motion.

(b) Pitch decay motion.

(c) Heave natural periods.

(d) Pitch natural periods.

Figure 4.5: Free decay motions time-series and computed natural periods in fully-loaded conditions. The approximate ranges of T_{z1} to T_{z4}, and $T_{\theta 1}$ to $T_{\theta 4}$ are indicated by horizontal arrows in (a) and (b), respectively. Gray markers in (c) and (d) are for larger initial heave and pitch cases.

In order to obtain the natural periods, four different intervals between the subsequent peaks or subsequent troughs of the decay curves, as presented in Figures 4.5a and 4.5b, are extracted and shown in Figures 4.5c and 4.5d. The gray symbols belong to the cases with higher initial heave and pitch values which give relatively similar results as of the smaller initial values; indicating a negligible effects from initial values on natural periods.

The uncertainty of capturing the precise time intervals in which the peaks and troughs of the decay curves occur depends on the time step size. The time step size varies at different Froude numbers, see Section 4.3.4, and at worst situation may introduce an error up to $2\Delta t$ (one numerical time step error for each captured peak or trough) in the computations of natural period intervals for the unit ship length $L = 1$. In such situations, the maximum error may reach 0.03 s (at the highest Fr) in the calculation of natural period intervals for the results shown in Figure 4.5.

It can be seen that the motion coupling slightly increases both heave and pitch natural periods at all Froude numbers. Although there are some minor effects related to forward speed, the trend of such effects is not similar in all of the cases. These differences may originate from the fact that the non-zero forward speed introduces sinkage and trim which can for instance alter the underwater geometry of hull, water plane area and block coefficient and consequently the dynamics of the ship. This can be confirmed considering that the final heave and pitch motions amplitudes converge to zero for the cases with zero speed when the motions are totally decayed, but these values are non-zero (i.e., equal to sinkage and trim derived in Section 4.4) for the cases with non-zero forward speeds. Wu (2013) mentioned that the forward velocity effects on natural periods of motions are negligible. The effects seen in the current study are also small and they might be negligible considering the possible error introduced by the time step size.

It is interesting to study the vessel heave and pitch responses in regular head waves when the wave encounter period is close to heave and pitch natural periods. Since the aim of this study is to investigate the behavior of the vessel in waves, the exact value of heave and pitch natural periods are not of a critical importance per se. In order to be consistent, natural periods of heave and pitch motions are approximated through averaging the calculated values for all Froude numbers in 3DOF (only small initial values), which gives $T_z \approx 1.488$ s and $T_\theta \approx 1.416$ s in the fully-loaded condition. Similarly, free heave and pitch decay simulations in 3DOF at Fr_0, Fr_2 and Fr_6 are also performed in the ballast condition and the natural periods are approximated as $T_z \approx 1.307$ s and $T_\theta \approx 1.177$ s. The same method is used for averaging, but since the motions decay faster in the ballast condition, only two periods T_{z1} and T_{z3} for heave and $T_{\theta 1}$ and $T_{\theta 3}$ for pitch are considered. As it can be confirmed in the studies by Lewis (1989) and Wu (2013), the larger block coefficient in the fully-loaded condition gives larger heave and pitch natural periods in comparison to the ballast condition.

4.5 Regular Wave Results

All of the potential flow computations in waves are carried out for the bare hull in 3DOF in the 5th order Stokes regular head waves. Then the hydrodynamic performance of the vessel is analyzed. An overview of the operational conditions in waves is given in Table 4.3. Resistance and motions as the main ship responses are investigated and the simulation results are compared against the available self-propulsion 6DOF model test data. Ship responses in waves are mainly influenced by the wave forces (and moments) exerted on the hull. Wave excitation forces and radiation forces form the total wave forces acting on the hull in the presence of waves. The forces exerted on the restrained hull in waves

which excite the motions are called wave excitation forces. Radiation forces are due to the motions of the ship which is forced to oscillate in calm water. In the current FNPF computations, the total forces (and moments) acting on the ship are calculated from the pressure integration on the wetted surface area of the hull and the force decomposition into different components is not possible.

Fourier analysis is used to evaluate the time-series of the responses. It should be noticed that, the mean velocity $\bar{V}$ and hence the encounter wave frequency in the self-propulsion model tests are slightly different than the simulation encounter wave frequency, see Section 4.2. Moreover, the wave amplitude A used for non-dimensionalization of the harmonic amplitudes of motions and added wave resistance in the FNPF method is the theoretical 5th order stokes wave amplitude, while for SP EFD data A is derived from the wave height measurements explained in Section 4.3.7. The regular head wave results are presented in model-scale.

4.5.1 Motion Responses

The 0th harmonic amplitudes of surge, heave and pitch motions are relatively small and almost equal to the values observed in their respective operational conditions in calm water. The 1st harmonic amplitudes of these motions are the dominating components in the Fourier analysis of the response signals, whereas higher order components are close to zero. Generally, the amplitudes and phases of wave excitation and radiation forces, which form the total wave forces, determine the motion responses of the ship in different conditions. In the following, different motion responses of the ship in regular waves are analyzed in which the 1st and 2nd harmonic amplitudes of motions are considered. It should be pointed out that the harmonic amplitudes of motions derived from the model tests are rounded which turned the small values of the 2nd harmonic amplitudes of motions into zero.

Surge Motion

The surge motion response of the ship is shown in Figures 4.6 and 4.7 for the fully-loaded and ballast conditions, respectively. The magnitude of the 1st harmonic surge motion x_1 is rather small except for very long waves, where the wave excitation surge forces are expected to be large. At the same Froude number, x_1 increases by increasing wave height, see Figures 4.6a and 4.7a. Very small local peaks are seen especially in the fully-loaded condition, see Figures 4.6b and 4.7b, where the wave encounter frequency is close to the heave and pitch natural frequencies ($\omega_z \approx 4.22\ rad/s$ and $\omega_\theta \approx 4.44\ rad/s$ in fully-loaded condition and $\omega_z \approx 4.81\ rad/s$ and $\omega_\theta \approx 5.34\ rad/s$ in ballast condition). This might be an indication of strong motion coupling within that range of encounter frequencies. On the other hand, these local peaks occur in the vicinity of $\lambda/L = 0.70$ for most of the studied operational conditions, see Figures 4.6a and 4.7a, which may reflect the effects of wave excitation surge forces near such wave lengths. In other words, these local peaks may occur due to the nearly matching lengths of the incident wave and the parallel mid-body (the distance between fore and aft shoulders). More investigations near such wave lengths are motivated for different hull types.

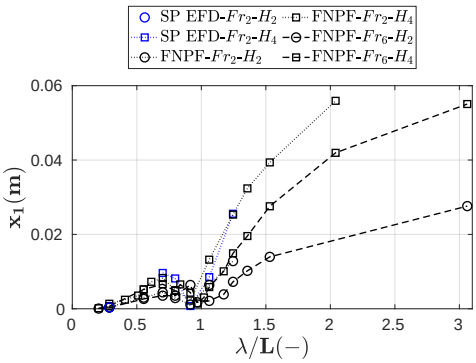

(a) Surge 1st harmonic amplitude.

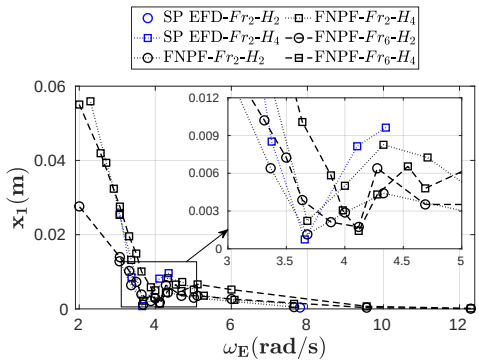

(b) Surge 1st harmonic amplitude.

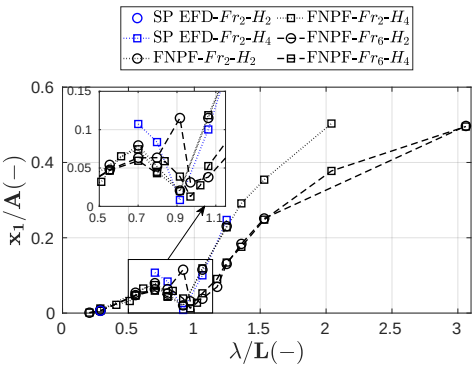

(c) Non-dimensional 1st harmonic amplitude.

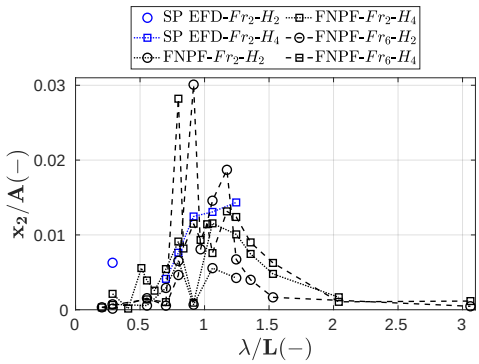

(d) Non-dimensional 2nd harmonic amplitude.

Figure 4.6: Comparison of the computed surge motion response with the measured values in regular head waves in fully-loaded condition.

The non-dimensional 1st harmonic amplitude of surge motion, shown in Figures 4.6c and 4.7c, indicates an approximate linear relation of the 1st harmonic surge motion response to wave amplitude A, as the cases with similar Froude number and different wave heights have almost similar x_1/A. The non-dimensional 2nd harmonic amplitude of surge motion, shown in Figures 4.6d and 4.7d, are rather small compared to x_1/A. Since the surge motion response of the vessel is rather insignificant, any possible numerical errors can significantly affect the results. Therefore, drawing a more solid conclusion about surge motion response would involve a high level of uncertainty.

The importance of accurate surge prediction for ships operating in waves has been discussed in literature. For instance, Joncquez et al. (2008) stated that the influence of surge motion on added wave resistance of a bulk carrier is insignificant. Moreover, Sadat-Hosseini et al. (2013) found that for KVLCC2 vessel the effects of surge motion on added wave resistance was negligible in their numerical computations, however, their model tests under free and fixed conditions revealed that the pitch motion and added

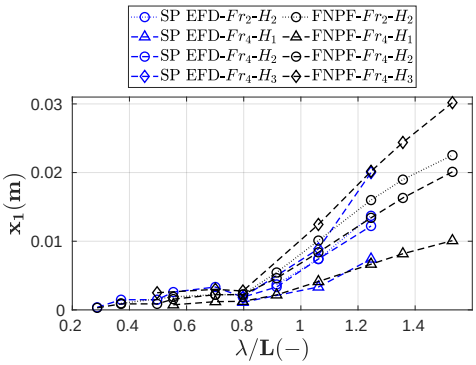

(a) Surge 1st harmonic amplitude.

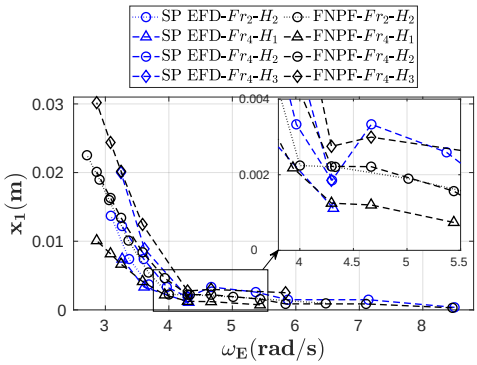

(b) Surge 1st harmonic amplitude.

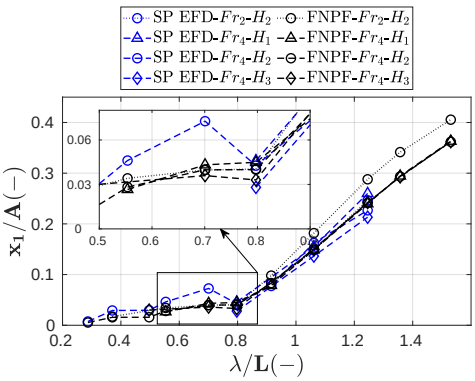

(c) Non-dimensional 1st harmonic amplitude.

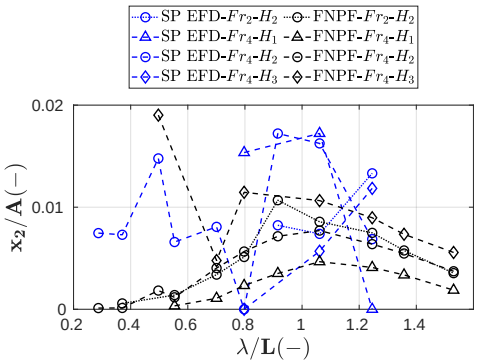

(d) Non-dimensional 2nd harmonic amplitude.

Figure 4.7: Comparison of the computed surge motion response with the measured values in regular head waves in ballast condition.

wave resistance are influenced in certain conditions. Yu et al. (2017) also mentioned that the prediction of surge motion is important due to the coupling between surge, heave and pitch motions. Therefore, accurate prediction of surge motion would be beneficial to enhance the prediction accuracy for other ship responses in waves. Generally, for the LDP vessel a good agreement between the FNPF computational results and experimental data is seen for the surge motion response of the ship in Figures 4.6 and 4.7.

Heave Motion

The heave motion response of the ship in both loading conditions is shown in Figures 4.8 and 4.9. The 1st harmonic amplitude of heave motion is relatively larger in the longest waves, see Figures 4.8a and 4.9a. There are clearly local maxima near the resonance condition in Figures 4.8b and 4.9b, i.e., when the encounter wave frequency is close

to $\omega_z \approx 4.22\ rad/s$ in the fully-loaded condition and $\omega_z \approx 4.81\ rad/s$ in the ballast condition. The wave encounter frequency of the local peak at Fr_2 (Figure 4.9b) is under-resolved in the computations meaning that more simulations are required in the vicinity of $\omega_z \approx 4.81\ rad/s$ to capture the trend of heave resonance. The heave resonance in the ballast condition is more pronounced, resulting in considerably large heave motion responses.

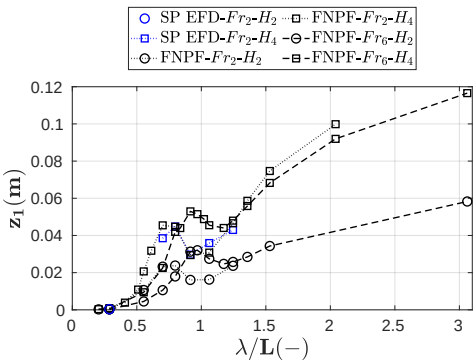

(a) Heave 1st harmonic amplitude.

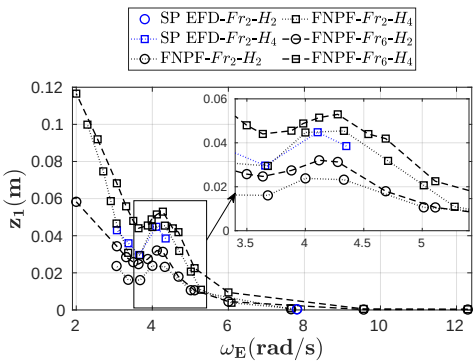

(b) Heave 1st harmonic amplitude.

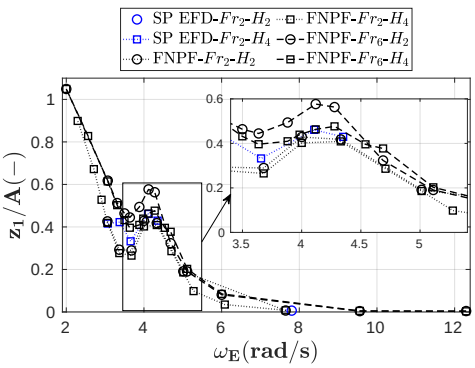

(c) Non-dimensional 1st harmonic amplitude.

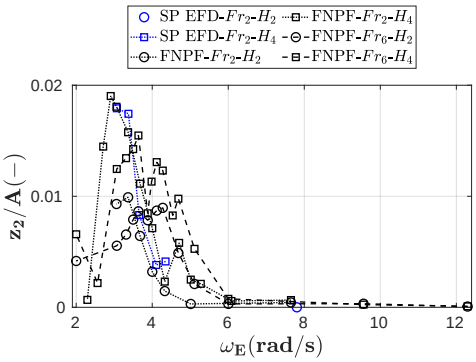

(d) Non-dimensional 2nd harmonic amplitude.

Figure 4.8: Comparison of the computed heave motion response with the measured values in regular head waves in fully-loaded condition.

The comparison of the non-dimensional 1st harmonic amplitude of heave motion between the cases with the same Froude number and different wave heights in Figures 4.8c and 4.9c, reveals an approximate linear relation between the heave 1st harmonic amplitude z_1 and the wave amplitude. However, this relation does not hold in the near resonance region in the fully-loaded condition, see e.g., Fr_6-H_2 and Fr_6-H_4 in Figure 4.8c. Irvine et al. (2008) also mentioned that the nonlinear effects for pitch and heave motions of a surface combatant vessel were evident near resonance conditions as z_1/A

and θ_1/kA showed wave steepness dependencies in those situations. Generally, for the LDP vessel, larger z_1/A arise for the cases with the same wave height and higher Froude numbers. The heave excitation force is expected to increase by increasing wave length and the maximum heave excitation force often occurs in extremely long waves. For the LDP vessel, the maximum may occur around $\lambda/L = 3.06$ as the computed z_1/A at Fr_6 exceeds 1 in the fully-loaded condition but the result obtained for $\lambda/L = 3.5$ (not included in the plots) shows reduction of z_1/A to 1 again. Very small z_2/A values are seen in Figures 4.8d and 4.9d compared to z_1/A. The non-dimensional 2nd harmonic amplitude of heave motion increases by decreasing ω_E in both loading conditions but it decreases again in very long waves. Since z_2 values from the experimental data are rounded, the small values obtained from the ballast conditions are turned into zero. The potential flow results for the heave motion response agree quite well with the available experimental data. The largest discrepancies of z_1/A are seen at $\omega_E \approx 3.37\ rad/s$ in the fully-loaded condition and at the resonance in the ballast condition.

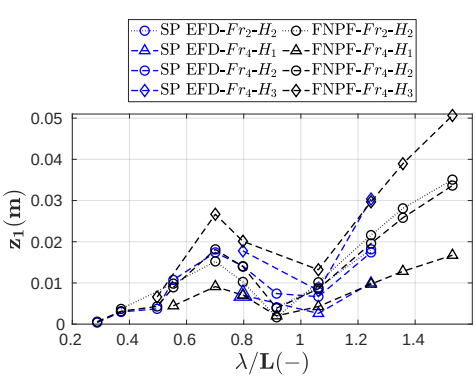

(a) Heave 1st harmonic amplitude.

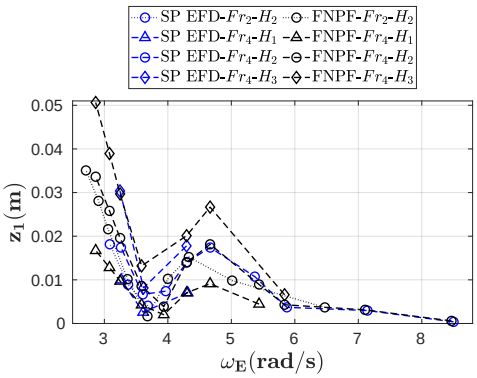

(b) Heave 1st harmonic amplitude.

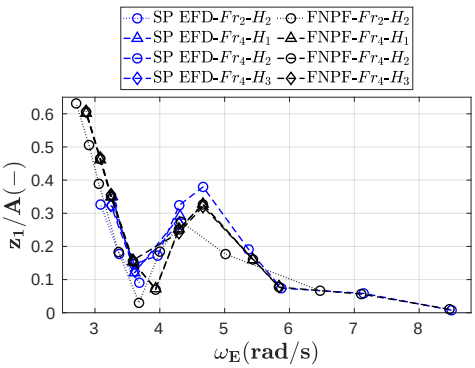

(c) Non-dimensional 1st harmonic amplitude.

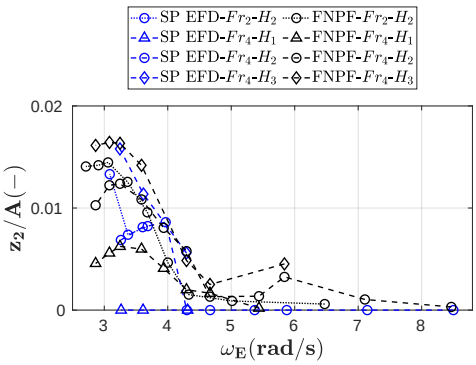

(d) Non-dimensional 2nd harmonic amplitude.

Figure 4.9: Comparison of the computed heave motion response with the measured values in regular head waves in ballast condition.

Pitch Motion

The pitch motion response of the ship is shown in Figures 4.10 and 4.11 for the fully-loaded and ballast conditions, respectively. Global maxima for the 1st harmonic amplitudes of pitch motion are observed in the vicinity of $\lambda/L = 1.24$ in the fully-loaded condition and close to $\lambda/L = 1.35$ in the ballast condition, see Figures 4.10a and 4.11a. Presumably the maximum excitation pitch forces occur in the vicinity of these wave lengths and the combination with the radiation forces (considering the phase differences between them) yield the maxima in pitch motion. This hypothesis has also mentioned by Lewis (1989) and seen in the studies by Irvine et al. (2008), Sadat-Hosseini et al. (2013) and Simonsen et al. (2013) for different ship hulls that the maximum pitch excitation depends only on the ship length and the incident wave length which occurs in $\lambda/L \approx 1.33$. For the LDP vessel, in the vicinity of $\lambda/L = 1.24$, the cases with the same wave height and higher Froude numbers, exhibit larger θ_1 in the fully-loaded condition, see Figure 4.10a. Nevertheless, this trend is not seen in the ballast condition in Figure 4.11a, and θ_1 values near the global maxima are almost equal for H_2 at Fr_2 and Fr_4.

There are small local maxima associated with resonance near the region in which the wave encounter frequency matches the pitch natural frequency in the ballast condition ($\omega_\theta \approx 5.34\ rad/s$), see Figure 4.11b. However, this trend is not seen in fully-loaded condition in Figure 4.10b for wave encounter frequencies close to $\omega_\theta \approx 4.44\ rad/s$. The reason might be that the wave excitation pitch forces continuously increase within that wave length range by increasing wave lengths, hence θ_1 increases accordingly and no local maximum occurs as the result of total wave forces in the fully-loaded condition. On the other hand, comparison of θ_1 values versus the non-dimensional wave lengths in Figures 4.10a and 4.11a reveals that these secondary local maxima appear in $\lambda/L = 0.55$ in both loading conditions. It is mentioned that the response of the ship in regular waves is formed as a result of combination of wave excitation and radiation forces amplitudes and phases. Since the radiation forces are expected to be relatively small in short waves, the effects of the wave excitation forces may probably produced these secondary peaks. More studies on the pitch response of ships near $\lambda/L \approx 0.55$ are motivated. For the LDP vessel, these secondary peaks are comparatively larger in the ballast condition mainly due to the occurrence of the pitch resonance in the vicinity of $\lambda/L = 0.55$ at the studied Froude numbers.

The comparison of the non-dimensional 1st harmonic amplitude of pitch motion between the cases with the same Froude number and different wave heights clearly demonstrates an approximate linear relation between the pitch 1st harmonic amplitude and the wave slope kA, see Figures 4.10c and 4.11c. θ_1/kA near the maximum pitch excitation wave lengths are larger at the higher Froude numbers for the same wave height in the fully-loaded condition, however, almost equal in the ballast condition. The FNPF computed pitch motion response agrees well with the experimental data (in which the effects of actual measured incident wave amplitude is taken into consideration). Nonetheless, modest discrepancies of θ_1/kA are seen in the ballast condition in long waves, see Figure 4.11c. These discrepancies are mainly under-predictions at Fr_4 and over-predictions at Fr_2. The non-dimensional 2nd harmonic amplitudes of pitch motion are shown in Figures 4.10d and 4.11d. Very small local peaks are seen near $\lambda/L \approx 1$ in both loading conditions.

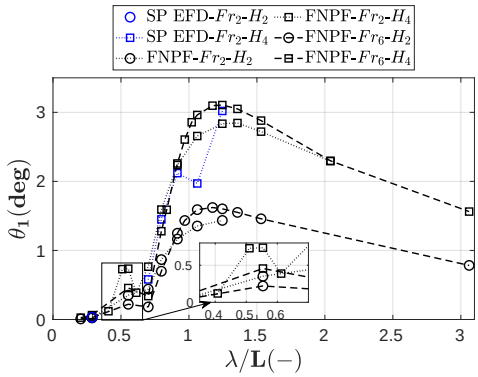

(a) Pitch 1st harmonic amplitude.

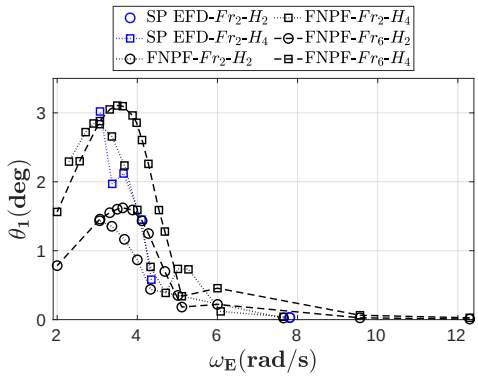

(b) Pitch 1st harmonic amplitude.

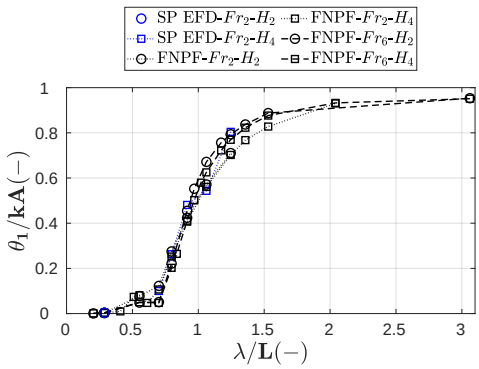

(c) Non-dimensional 1st harmonic amplitude.

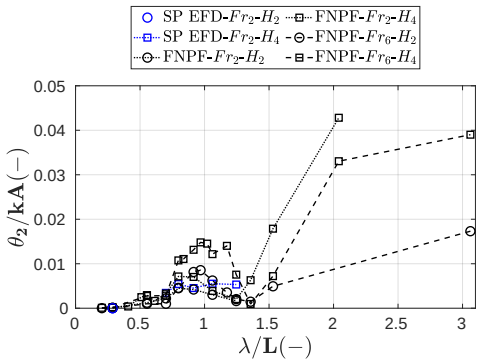

(d) Non-dimensional 2nd harmonic amplitude.

Figure 4.10: Comparison of the computed pitch motion response with the measured values in regular head waves in fully-loaded condition.

Although the 2nd harmonic amplitudes of pitch motion have rather small values, very good predictions are obtained from the FNPF method as the trend of curves with respect to the wave length is similar to the trend of measured values.

Based on the studied 1st harmonic amplitudes of different motions, it can be endorsed that the vessel in very long waves follows the water surface, as the surge, heave and pitch non-dimensional 1st harmonic amplitudes approach the value of 1 by increasing wave length. However, the overall behavior of the vessel over the wide range of wave lengths depends not only on the harmonic amplitudes of motions, but also on the harmonic phases of these motions. It is seen that the magnitudes of the surge motion responses are rather small, hence the behavior of the vessel is mainly influenced by the heave and pitch motions in regular head waves. The first and second harmonic amplitude of these motions has been covered up to here. In the subsequent part the harmonic phase of these motions are presented to conclude the discussion.

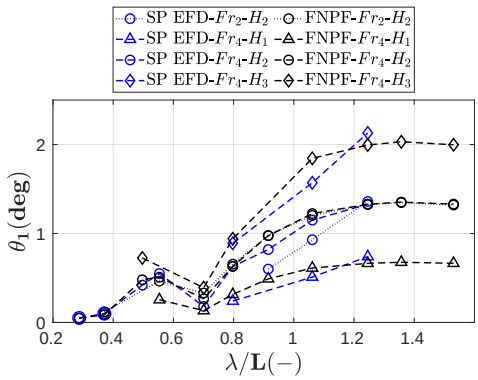

(a) Pitch 1st harmonic amplitude.

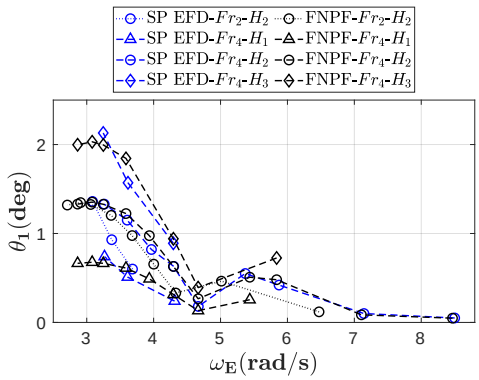

(b) Pitch 1st harmonic amplitude.

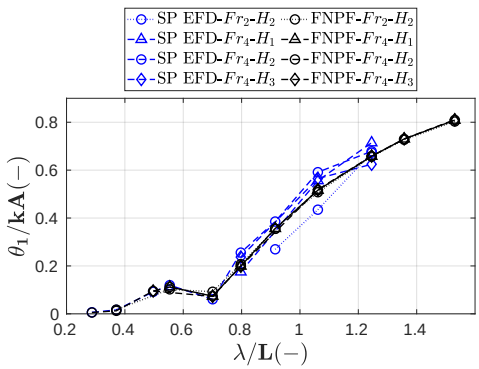

(c) Non-dimensional 1st harmonic amplitude.

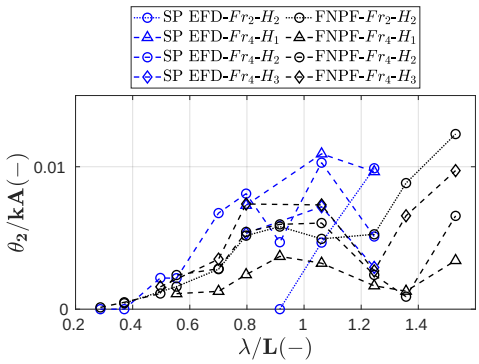

(d) Non-dimensional 2nd harmonic amplitude.

Figure 4.11: Comparison of the computed pitch motion response with the measured values in regular head waves in ballast condition.

Heave and Pitch Motions Phase Difference

The 1st harmonic phase of pitch motion $\theta_{\varepsilon 1}$ is subtracted from the 1st harmonic phase of heave motion $z_{\varepsilon 1}$ for both loading conditions and the results are shown in Figure 4.12. The resulted phase difference curves for various conditions exhibit a quite similar trend when plotted against λ/L. The phase difference in very long waves approaches -90 *deg* confirming the behavior of the vessel in long waves in which the heave motion is synchronized with the wave motion near the COG and its phase goes to 0 *deg* while the pitch phase tends to 90 *deg* as the pitch response is in phase with the wave slope. A comparable trend in long waves is also seen by Sadat-Hosseini et al. (2013) and Simonsen et al. (2013) for KVLCC2 and KCS vessels, respectively. The largest relative motions may occur when there are large amplitude motion responses together with a phase difference of ± 180 *deg* or 0 *deg*. For the LDP vessel, the phase difference values are close to zero

in $\lambda/L = 0.91$ at Fr_2 as well as $0.79 < \lambda/L < 1.02$ at Fr_6 in the fully-loaded condition. In ballast condition the phase difference for Fr_2-H_2 occurred in $\lambda/L = 0.91$. However, for other cases in the ballast condition, near-zero values of the phase difference are under-resolved in the simulations and additional wave lengths near $\lambda/L \approx 1$ are required to capture the condition with approximately zero phase difference. The trends of curves as well as the phase difference values computed in the FNPF method are comparable to that of self-propulsion model test data in both loading conditions.

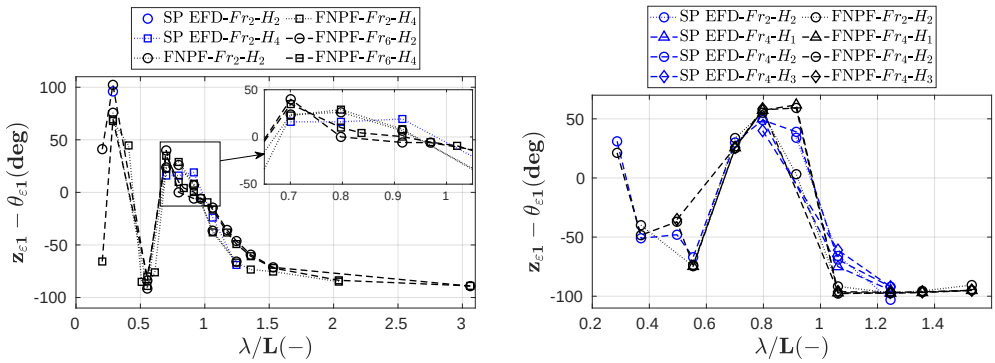

(a) Fully-loaded condition.

(b) Ballast condition.

Figure 4.12: Comparison of the computed heave and pitch 1st harmonic phase difference with the measured values in regular head waves.

The abrupt transition in the phase difference curves from high positive values to approximately -80 down to -90 *deg* in the vicinity of $\lambda/L = 0.55$ in the fully-loaded condition is an interesting feature, see Figure 4.12a. A similar behavior also can be seen in the ballast condition, however, since the ship responses are investigated only in a limited number of wave lengths near $\lambda/L = 0.55$, the trend of phase difference can not be precisely determined. It should be reminded that the secondary local maxima for θ_1 are also seen near such wave lengths, which encourages further investigations. Sadat-Hosseini et al. (2013) reported an abrupt jump of $\theta_{\varepsilon 1}$ of KVLCC2 around $\lambda/L = 0.7$. It should be noted that in the extreme short waves other harmonic amplitudes of motions have the same order of magnitude as the 1st harmonic amplitude. Thus, the ship only oscillates with very small amplitudes around the calm water sinkage and trim values. The ship response in such conditions is particularly nonlinear with relatively small amplitudes, which makes the 1st harmonic phase difference unimportant for determination of ship behavior. For instance, see Figure 4.12a for the abrupt transitions occurred in the shortest waves in the fully-loaded condition.

Validation Error of Motions

In order to present a quantitative analysis of errors associated with the FNPF method predictions compared to the experimental data, the averaged absolute errors are derived

and shown in Table 4.4. First, the comparison errors in terms of percentage of the experimental data are calculated in the equivalent operational conditions shown in Table 4.3 for the dimensional and non-dimensional surge, heave and pitch 1st harmonic amplitudes. Then, the absolute error values $|E|$ are calculated and averaged $|\bar{E}|$ for the respective Froude numbers, wave heights and wave lengths in each loading condition for the mentioned responses. The averaged absolute errors reduce when the effects of actual incident wave heights measured in the model tests are taken into account, hence $|\bar{E}|$ for the non-dimensional 1st harmonic amplitudes are smaller than the dimensional 1st harmonic amplitude $|\bar{E}|$ for each motion response. The only exception is the heave motion response in the fully-loaded condition where the magnitude of the averaged absolute errors are relatively low. However, the effect of actual model speed in the self-propulsion model tests, which alters the wave encounter frequency, is not taken into consideration. The highest averaged absolute errors are seen for the surge motion response of the ship, mainly because that x_1 and x_1/A values are small, thereby small differences yield large errors.

Table 4.4: Averaged absolute errors of the FNPF method results in percentage of the experimental data for motion responses.

Loading Conditions	$\|\bar{E}\|_{x_1}$ (%)	$\|\bar{E}\|_{x_1/A}$ (%)	$\|\bar{E}\|_{z_1}$ (%)	$\|\bar{E}\|_{z_1/A}$ (%)	$\|\bar{E}\|_{\theta_1}$ (%)	$\|\bar{E}\|_{\theta_1/kA}$ (%)
Fully-loaded	56.6	47.2	7.1	13.4	18.5	9.9
Ballast	27.3	19.2	23.8	19.7	16.6	12.4

One possible source of discrepancy between the predicted motions by the FNPF method and model test data is the difference in the number of degrees of freedom between these methods and consequently, difference in the motion coupling. The model in the experiments was free in all six degrees of freedom that possibly has altered the ship responses in regular head waves. Moreover, a few other factors such as rudder or propeller existence may contribute to the discrepancy between the computed motions and the measured ones.

4.5.2 Resistance Responses

Wave Making Resistance

The mean wave making resistance $\bar{R}_W$ as well as the added wave resistance coefficient C_{AW} are shown for both loading conditions in Figures 4.13 and 4.17. The mean wave making resistance in self-propulsion model tests in regular head waves is deduced from the mean measured thrust based on Equation 4.5 assuming the same thrust deduction factor and frictional resistance as of calm water, see Section 4.2. Moreover, $\bar{R}_F$ is computed for the mean attained speed $\bar{V}$ and the thrust deduction factor at $\bar{V}$ is interpolated from the calm water t_d at the speeds given in Table 4.2. The added wave resistance coefficient C_{AW} is computed from Equation 4.15, in which linear interpolation is used for calm water resistance R_W at the attained speed, see Section 4.3.7. It is worth mentioning that the negative calm water resistance values obtained from the simulations in ballast condition (see Section 4.4) are considered as zero in this equation. Moreover, in the calculation of C_{AW}, the considered wave amplitude A in FNPF computations is the theoretical 5th

order Stokes wave amplitude, while in the experimental data A is derived from the wave height measurements based on the procedure explained in Section 4.3.7.

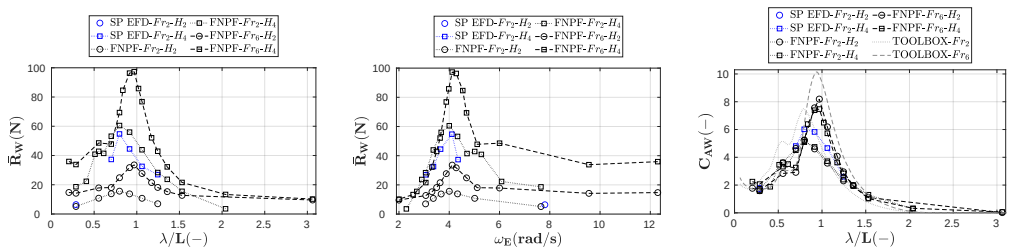

(a) Mean wave making resistance.

(b) Mean wave making resistance.

(c) Added wave resistance coefficient.

Figure 4.13: Comparison of the computed resistance response with the measured values in regular head waves in fully-loaded condition.

In the fully-loaded condition in Figure 4.13, the values of mean wave making resistance are larger for the higher encountered wave heights at the same Froude number. Moreover, the maximum value of $\bar{R}_W$ at the same wave height increases by increasing Froude number while moving towards longer waves, see Figure 4.13a. The resistance peaks for the wave heights H_2 and H_4 occur in $\lambda/L = 0.79$ at Fr_2 as well as $\lambda/L = 0.97$ at Fr_6. Comparison of $\bar{R}_W$ versus ω_E in Figure 4.13b reveals that the main peaks of mean wave making resistance occur at the wave encounter frequencies which are rather close to the heave and pitch natural frequencies ($\omega_z \approx 4.22\ rad/s$ and $\omega_\theta \approx 4.44\ rad/s$). In such conditions, θ_1 values are also relatively large (Figure 4.10b) and heave resonance yields a local maxima (Figure 4.8b). The 1st harmonic phase difference between heave and pitch motions in Figure 4.12a becomes approximately zero in the vicinity of $\lambda/L = 0.91$ at Fr_2 and in $0.79 < \lambda/L < 1.02$ at Fr_6, which together with the heave and pitch motion responses produce large relative motions and hence large mean wave making resistance.

Another important aspect of the mean wave making resistance in Figure 4.13a is the existence of small secondary local peaks near $\lambda/L = 0.55$, except for Fr_2-H_4 which is under-resolved in the simulations. Additional simulations with wave lengths in the vicinity of $\lambda/L = 0.55$ are required to capture a more accurate trend. Although the heave and pitch motion responses are rather insignificant near such wavelength (shown in Figures 4.8a and 4.10a), small secondary local maxima are observed in the pitch 1st harmonic amplitudes of the vessel. Furthermore, the 1st harmonic phase difference between heave and pitch motions in the fully-loaded condition near $\lambda/L = 0.55$ abruptly changes to approximately $-90\ deg$. Since the phase difference tends to $-90\ deg$, the behavior of the vessel is mainly determined by either heave or pitch motion at a time, similar to the ship motions in very long waves. Therefore, due to the existence of the secondary local peaks of pitch motion, it might be concluded that the secondary peaks of the mean wave making resistance are mainly governed by the pitch motion responses of the vessel. The secondary peaks of $\bar{R}_W$, at the same Froude number, are more significant for H_4 in comparison to H_2, similar to the respective θ_1 values near $\lambda/L = 0.55$.

The approximate linear relation of the added wave resistance to the wave amplitude squared has been discussed thoroughly in literature, for instance by Gerritsma and Beukelman (1972) and Block (1993). This can also be observed in Figure 4.13c as the cases with the same Froude number and different wave heights exhibit almost similar C_{AW}. Although the global trend of the added wave resistance is proportional to the wave amplitude squared, some conditions show a different trend. For instance, modest nonlinearities are seen in short waves as well as near the main peak of C_{AW}. Such nonlinear behavior is also reported for KVLCC2 by different authors, e.g, Yu et al. (2017), Lee et al. (2017), Lee et al. (2019b) and Seo et al. (2020). Overall, the FNPF computed wave making resistance resembles well to the model test data and the wave length in which the main peak of C_{AW} occurs for Fr_2-H_4 coincides in two methods. However, the computed and the measured C_{AW} values at the main peaks are different. Although in most of the studied wave lengths the measured mean wave making resistance is lower than the computed one, the relation between the measured and computed C_{AW} shows an opposite behavior when the effects of actual measured incident wave amplitude in model tests are taken into consideration. Interestingly, the TOOLBOX predicts the approximate wave lengths in which the peaks of added wave resistance coefficient occurs, however, it over-predicts the value of C_{AW} at both Froude numbers. The secondary peaks of added wave resistance coefficient near $\lambda/L = 0.55$ is also predicted by the TOOLBOX whereas the values of C_{AW} are over-predicted at Fr_2 and rather well predicted at Fr_6 compared to the FNPF results.

The computed harmonic amplitudes of wave making resistance by the FNPF method are shown in Figure 4.14 for the fully-loaded condition. The 1st harmonic amplitude of wave making resistance is the dominant component over the major range of wave lengths, except near $\lambda/L \approx 1$ in which the 2nd harmonic component is larger. R_{W1} is small in very short waves and has a large local peak around $\lambda/L \approx 0.55$, then its magnitude decreases considerably around $\lambda/L \approx 1$ and again increases in long waves. R_{W1} for the cases with the same wave height and lower Froude number are lower before $\lambda/L < 1$ however larger when $\lambda/L > 1$. The second harmonic amplitude of wave making resistance R_{W2} is maximum in $\lambda/L = 0.97$ at Fr_6 (exactly the same wave length as of maximum $\bar{R}_W$) and in $\lambda/L = 0.91$ at Fr_2 (maximum of $\bar{R}_W$ is in $\lambda/L = 0.79$) for both wave heights H_2 and H_4. It should be noticed that the ship responses in $\lambda/L = 0.97$ at Fr_2 is under-resolved in the FNPF computations, see Table 4.3. The 3rd harmonic component is very small except in the vicinity of $\lambda/L = 0.83$ at Fr_6-H_4. The wave making resistance response of the ship is mainly formed based on the different harmonic amplitudes of the wave making resistance together with the consideration of harmonic phases.

In order to have a clearer picture of the wave making resistance response of the ship, a selection of computed R_W time-series (the same time window in which the Fourier analysis is performed on) are shown in Figure 4.15 in the fully-loaded condition. The selected conditions are extracted for both of the studied wave heights in a short and a long wave length where the 1st harmonic amplitudes are larger than the higher harmonic amplitudes. Moreover, a wave length is selected near the region where the 1st harmonic amplitude is small and comparable to the higher harmonic amplitudes. The nonlinearities can also be observed in the time-series as the wave making resistance exhibits nonlinear behavior when the higher harmonics are significant.

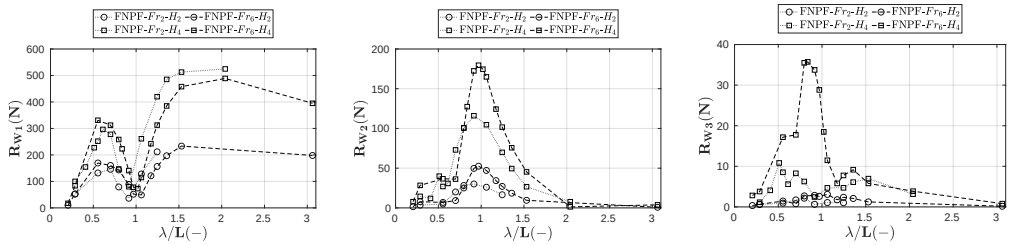

(a) 1st harmonic amplitude. (b) 2nd harmonic amplitude. (c) 3rd harmonic amplitude.

Figure 4.14: The harmonic amplitudes of wave making resistance in regular head waves in fully-loaded condition.

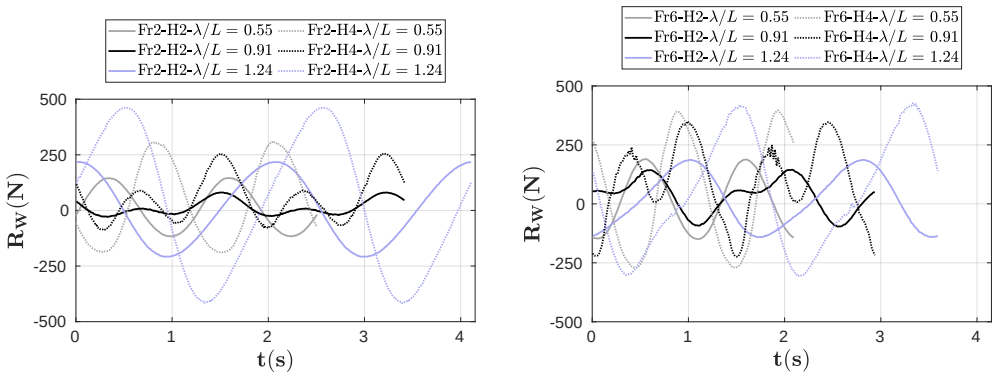

(a) Selected time-series at Fr_2. (b) Selected time-series at Fr_6.

Figure 4.15: Wave making resistance time-series over two encountered wave periods in regular head waves in fully-loaded condition.

In Figure 4.16, the 1st and 2nd harmonic amplitudes of wave making resistance are non-dimensionalized by $\rho g B^2 A$ and $\rho g B^2 A^2/L$, respectively. An approximately linear correlation between R_{W1} and the wave amplitude A is observed as the cases with the same Froude number and different wave heights have similar values in Figure 4.16a. $R_{W1}/\rho g B^2 A$ exhibit a considerably large peak within $0.50 < \lambda/L < 0.70$, which might be related to the secondary local maxima seen for θ_1 in the same wave length interval which is believed to be the cause of the secondary peak of C_{AW}. This might be the cause of the nonlinearities seen for the relation between the added wave resistance and wave amplitude squared in short waves. An approximately linear correlation between R_{W2} and the wave amplitude squared A^2 is seen in Figure 4.16b, except than the vicinity of $\lambda/L \approx 1$.

In the ballast condition in Figure 4.17, similar to the fully-loaded condition, the values of the mean wave making resistance are larger for the higher encountered wave heights at the same Froude number. Contrary to the fully-loaded condition, $\bar{R}_W$ in the ballast condition does not vary significantly over the whole range of wave lengths and there

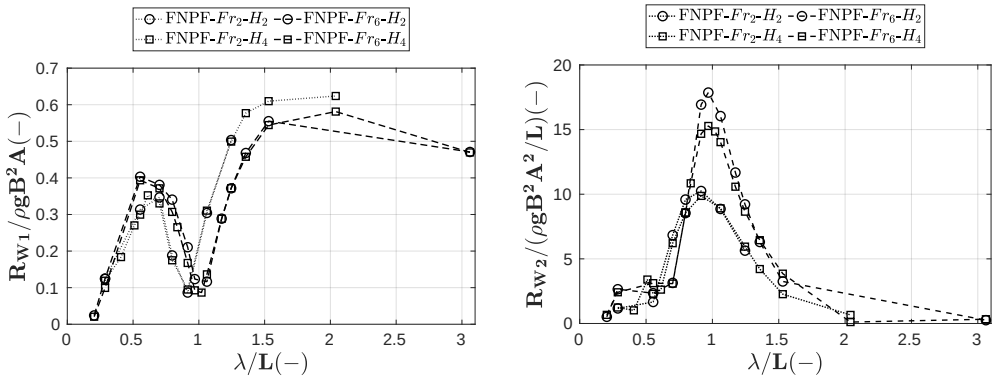

(a) The 1st harmonic amplitude.

(b) The 2nd harmonic amplitude.

Figure 4.16: The non-dimensional harmonic amplitudes of wave making resistance in regular head waves in fully-loaded condition.

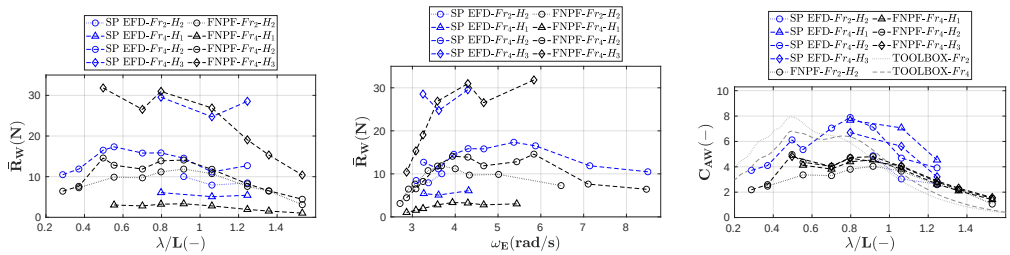

(a) Mean wave making resistance.

(b) Mean wave making resistance.

(c) Added wave resistance coefficient.

Figure 4.17: Comparison of the computed resistance response with the measured values in regular head waves in ballast condition.

are no dominant large peaks formed, see Figure 4.17a. Instead, there are two relatively small peaks near $\lambda/L = 0.49$ and $\lambda/L = 0.91$, while for Fr_2-H_2 in $\lambda/L = 0.49$ as well as Fr_4-H_3 in $\lambda/L = 0.91$ these peaks are under-resolved in the simulations. Although in the ballast condition local peaks are seen for z_1 and θ_1 in the near resonance conditions, the peaks of $\bar{R}_W$ do not coincide with the natural frequencies of heave and pitch motions. It should be noted that, the overall behavior of the hull is related not only to its motions amplitudes but also the phase differences of the motions. For instance, high value of $\bar{R}_W$ at Fr_2-H_2 in $\lambda/L = 0.91$ might be due to the near zero 1st harmonic phase difference between heave and pitch motions and hence large relative motions in that wave length. It is seen that the near-zero phase difference for other conditions are under-resolved in the simulations. Due to the complexity of the motions amplitudes and phases in the ballast condition, it is hard to derive more solid statements regarding the relation of the mean wave making resistance to the motion responses.

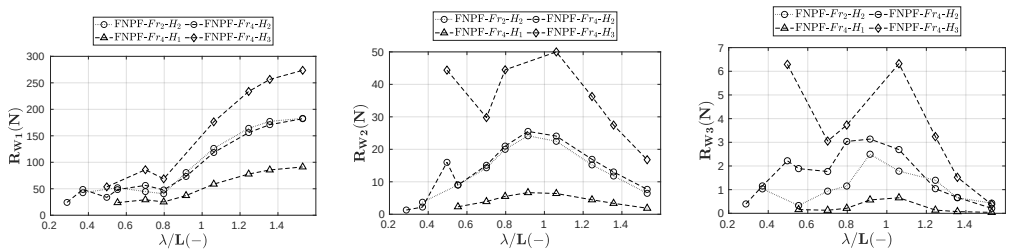

(a) 1st harmonic amplitude. (b) 2nd harmonic amplitude. (c) 3rd harmonic amplitude.

Figure 4.18: The harmonic amplitudes of wave making resistance in regular head waves in ballast condition.

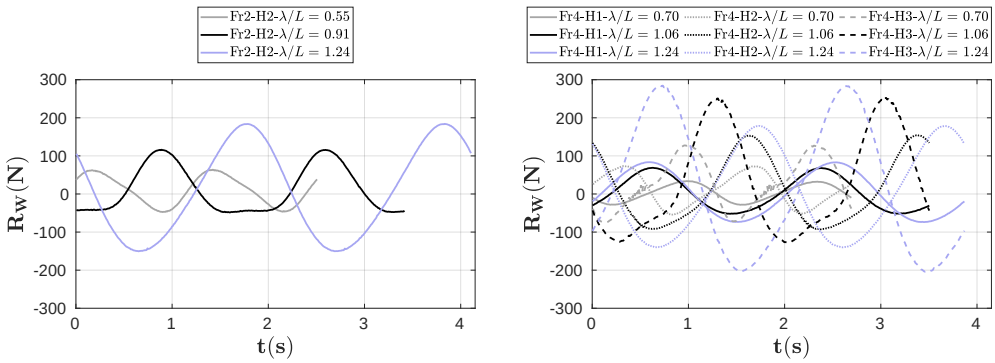

(a) Selected time-series at Fr_2. (b) Selected time-series at Fr_4.

Figure 4.19: Wave making resistance time-series over two encountered wave periods in regular head waves in ballast condition.

Comparison of C_{AW} in the ballast condition reveals an approximate quadratic relation between wave amplitude and the added wave resistance in FNPF computations. Nevertheless, this dependency is not valid in the experimental data, as the measured C_{AW} values in different wave heights are scattered in long waves. The trend of computed $\bar{R}_W$ is comparable to the experimental data in most of the wave lengths except from $\lambda/L = 1.06$ to $\lambda/L = 1.24$ in which the experimental resistance increases but the simulated one decreases, see Figure 4.17a. However, reduced C_{AW} in $\lambda/L = 1.24$ in Figure 4.17c reveals that the incident wave amplitude in those model tests were actually larger than the theoretical wave amplitudes, which explains the reason for larger measured mean wave making resistance relative to the simulated values, see Figure 4.17a. Although the trend of C_{AW} versus λ/L is rather similar in the FNPF computations and model test experiments, the computed added wave resistance coefficient is clearly under-predicted, except acceptable predictions for Fr_2-H_2. One possible source of discrepancies might be related to the modest under-predictions of pitch motion at Fr_4 and small over-predictions

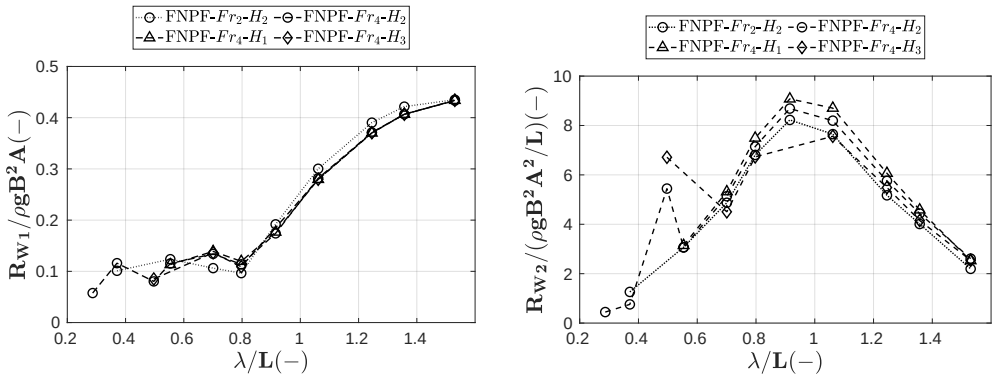

(a) The 1st harmonic amplitude.

(b) The 2nd harmonic amplitude.

Figure 4.20: The non-dimensional harmonic amplitudes of wave making resistance in regular head waves in ballast condition.

at Fr_2 in Figure 4.11c. The C_{AW} results from the TOOLBOX also shows two peaks, while the peak in shorter waves is relatively higher at lower Froude number. It should be noted that the draft in the ballast condition in TOOLBOX is considered as the average draft between the fore and aft perpendiculars which does not exactly resemble the ballast condition considered in the FNPF simulations and model test experiments, see Section 4.3.6.

The harmonic amplitudes of wave making resistance in the ballast condition are shown in Figure 4.18. The 1st harmonic amplitude of wave making resistance is the dominant component over the whole range of wave lengths, unlike the fully-loaded condition in which the 2nd harmonic amplitudes are dominant near $\lambda/L \approx 1$. R_{W3} is smaller than other harmonic amplitudes. R_{W1} is small in short waves up to $\lambda/L \approx 0.79$ and then it starts to increase in the longer waves. R_{W2} is large around $\lambda/L = 0.49$, where $\bar{R}_W$ is also large in Figure 4.17a. Non-dimensional R_{W1} and R_{W2} are shown in Figure 4.20 where their relations with the wave amplitude is found to be similar to that of fully-loaded condition. It is interesting that the peaks of $R_{W2}/(\rho g B^2 A^2/L)$ occur in the same wave lengths as of peaks of C_{AW} in the ballast condition. A selection of R_W time-series in the ballast condition is shown in Figure 4.19. The nonlinear behavior of the wave making resistance time-series in $\lambda/L = 0.91$ at Fr_2 and in $\lambda/L = 1.06$ at Fr_4 can also be identified in the harmonic amplitudes of R_W in Figure 4.18.

Validation Error of Resistance

The same procedure explained in Section 4.5.1 are used to calculate the averaged absolute errors of mean wave making resistance and added wave resistance coefficient in waves, see Table 4.5. Although the effect of actual incident wave height significantly reduced the averaged absolute error in the fully-loaded condition, $|\bar{E}|_{C_{AW}}$ is slightly increased in the ballast condition compared to the averaged absolute error of the mean wave making

resistance.

Table 4.5: Averaged absolute errors of the FNPF method results in percentage of the experimental data for resistance responses.

Loading Conditions	$\lvert\bar{E}\rvert_{\bar{R}_W}$ (%)	$\lvert\bar{E}\rvert_{C_{AW}}$ (%)
Fully-loaded	23.1	12.0
Ballast	25.6	28.3

Although the motions of the LDP vessel are predicted with a high level of accuracy through the potential flow computations, the accuracy of resistance predictions are arguable. C_{AW} in both loading conditions is mostly under-predicted compared to the experimental data. It should be kept in mind that the model tests have been carried out in free-sailing self-propulsion mode while the FNPF computations were performed for the bare hull in 3DOF. One source of discrepancy would be the other degrees of freedom present in the model tests. Valanto and Hong (2017) also mentioned that all motion responses have an effect on the wave added resistance of a cruise ship. Another source of discrepancy might be related to the propeller ventilation. Although the LDP was initially expected to undergo severe ventilation, it was found during the tests that the "tunnel-shaped" aft configuration is very effective in keeping the propeller submerged. Propeller ventilation was observed in some operational conditions mostly in the cases with wave heights of H_3 or H_4. Although, the thrust and torque measurements showed relatively little sensitivity to occurrences of ventilation, minor effects could be anticipated on the results. It should be noticed that the interactions between the incoming waves, hull and propulsion system of the ship may strongly influence its performance in waves. Therefore, another source of discrepancy may be related to the considered assumption of similar R_F and t_d for the ship operating in regular head waves and in calm water.

Frictional Resistance

In order to examine the assumption on the frictional resistance, $\bar{R}_F$ in waves is calculated in the FNPF computations and compared with the respective calm water R_F in Figure 4.21. From simulations, at each time step the instantaneous velocity and wetted surface area are known. First, the instantaneous Reynolds number is computed assuming constant L. Then, the instantaneous C_F from the ITTC-57 model-ship correlation line in Equation 4.3 is calculated. Finally, by using the instantaneous wetted surface area, the instantaneous R_F is calculated from Equation 4.2. Similar to other responses, Fourier analysis on the R_F time-series is performed over the last two encountered wave periods when the simulations are converged. The change of mean frictional resistance in waves $\bar{R}_F$ is then computed in terms of percentage of the calm water frictional resistance R_F at each respective Froude number, see Figure 4.21. It can be seen that the mean frictional resistance is very similar to the calm water frictional resistance over the whole ranges of wave lengths in both loading conditions, as the change of frictional resistance in regular waves remains less than 2% of the calm water value. It should be noticed that other viscous effects such as periodic flow separations at the stern, splashes, bow and stern slamming and green water on deck are not taken into account and the frictional resistance coefficient is estimated

from the ITTC-57 model-ship correlation line in Equation 4.3. Higher fidelity viscous flow CFD simulations are needed for investigation of the aforementioned effects.

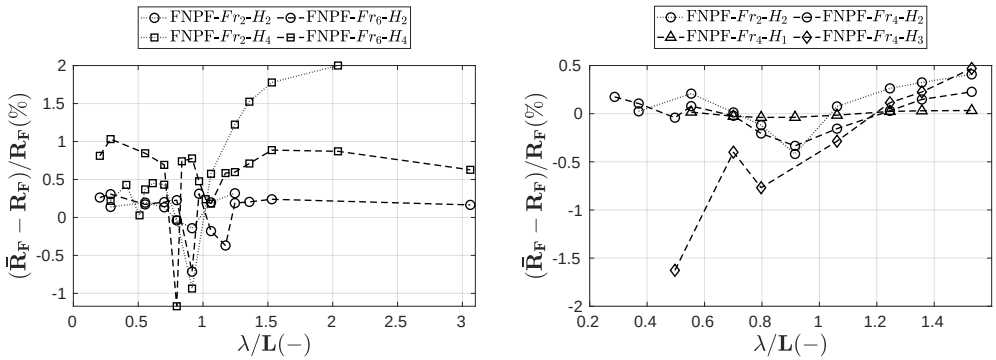

(a) Fully-loaded condition. (b) Ballast condition.

Figure 4.21: Change of $\bar{R}_F$ in waves in terms of percentage of its calm water value.

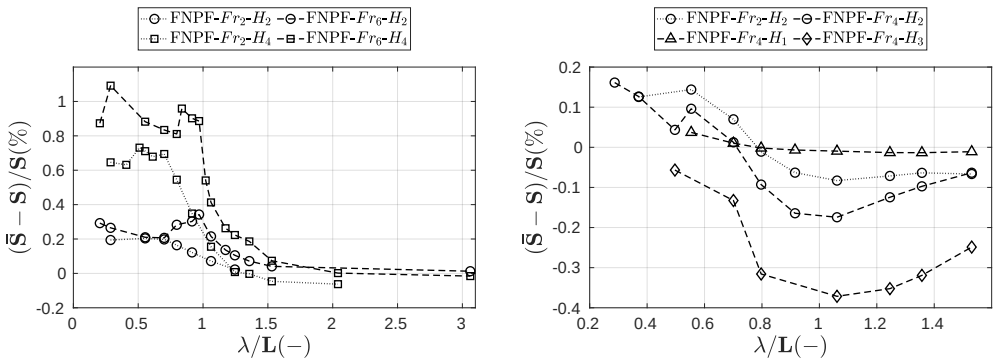

(a) Fully-loaded condition. (b) Ballast condition.

Figure 4.22: Change of the mean wetted surface area in regular head waves in terms of the percentage of its calm water value.

The change of wetted surface area in time in regular head waves exhibit a periodic behavior with a frequency equal to the wave encounter frequency. Therefore, Fourier analysis is performed on the time-series of wetted surface area captured in the FNPF simulations. The 0th and the 1st harmonic amplitudes are the dominant components, whereas higher harmonic components are negligible. The change of mean wetted surface area $\bar{S}$ in waves relative to the calm water wetted surface area S at each respective Froude number is shown in Figure 4.22. Change of the mean wetted surface area remains approximately less than 1% of the calm water S over the major part of the studied wave

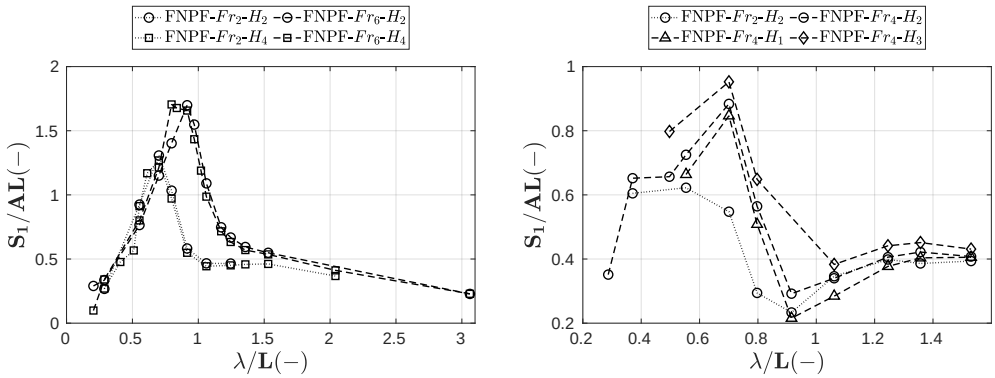

(a) Fully-loaded condition.

(b) Ballast condition.

Figure 4.23: The 1st harmonic amplitude of change of wetted surface area in regular head waves.

lengths in both loading conditions. In very long waves the values of $\bar{S}$ approaches the calm water wetted surface area as the vessel follows the water surface. Moreover, as shown in Figure 4.23, the first harmonic amplitude of wetted surface area S_1 in regular head waves are found to have an approximately linear relation with respect to wave amplitude in the cases with the same Froude number.

4.6 Conclusions

In this study, the hydrodynamic performance of a general cargo ship was investigated in terms of resistance and motions responses in calm water as well as in regular head waves. Two loading conditions were considered, namely, fully-loaded and ballast. A Fully Nonlinear Potential Flow (FNPF) panel method was used in order to predict the performance of the vessel in a wide range of operational conditions (loading conditions, Froude numbers, wave heights and wave lengths). Several computational settings (e.g., computational domain dimensions, hull and free surface discretization and time step size) in the FNPF solver were specified in order to attain a high level of computational efficiency with respect to cost and accuracy. The computational results were compared against model test data.

Our investigations in calm water at different Froude numbers include resistance simulations as well as free decay heave and pitch simulations (for obtaining natural periods of these motions) in various degrees of freedom. The computed wave making resistance, sinkage and trim by the FNPF method in calm water were in a rather good agreement with the measured data, except modest under-predictions of wave making resistance seen in the ballast condition at lower Froude numbers.

The 1st harmonic amplitudes of motions were the dominating components in the Fourier analysis of the motions responses in waves. The magnitudes of the 1st harmonic amplitudes of surge motion x_1 were rather small except in very long waves. Further

investigations are motivated on the very small local peaks seen in x_1 near $\lambda/L = 0.7$, in which the wave excitation surge forces associated with the ratio between the length of parallel mid-body and the incident wave length can be examined. In both loading conditions, the 1st harmonic amplitudes of heave motion z_1 exhibited local maxima near the heave resonance conditions, i.e., when the encounter wave frequency was close to the heave natural frequency. The heave resonances in the ballast condition were more intense resulting in prominent local maxima. Small local maxima near the resonance conditions were seen in the 1st harmonic amplitudes of pitch motion θ_1 solely in the ballast condition, whereas in the fully-loaded condition, the increasing pitch excitation wave forces near resonance conditions were believed to be the main reason for the absence of local maxima. On the other hand, θ_1 exhibited large peaks resulted from high excitation wave forces near $\lambda/L = 1.24$ and $\lambda/L = 1.35$ in the fully-loaded and ballast conditions, respectively. Furthermore, secondary local maxima for θ_1 were seen near $\lambda/L = 0.55$ in both loading conditions. These local peaks in the ballast condition coincided with the pitch resonance conditions resulting in considerable pitch 1st harmonic amplitudes. The 2nd harmonic amplitudes of motions are relatively lower than the 1st harmonic amplitudes except where both components are small and the ship motion responses are nonlinear with very small magnitudes.

The 1st harmonic phase differences between heave and pitch motions $z_{\varepsilon 1} - \theta_{\varepsilon 1}$ versus wave length exhibited rather similar trends in different operational conditions. The phase differences in very long waves approached -90 *deg* confirming the behavior of the vessel in long waves. In long waves, the heave motion was synchronized with the wave motion near the center of gravity (COG) and its phase converged to 0 *deg*, while the pitch phase tended to 90 *deg*, since the pitch response was in phase with the wave slope. Interesting abrupt transitions were seen in the phase difference curves near $\lambda/L = 0.55$. Overall, the predicted motion responses by the current FNPF method in regular head waves were in good agreement with the experimental data.

Another aspect investigated in this study was the 0th, 1st and 2nd harmonic amplitudes of the wave making resistance as well as the added wave resistance coefficients C_{AW} in different operational conditions. The 0th harmonic amplitude (mean value) of the wave making resistance $\bar{R}_W$ exhibited large peaks in the fully-loaded condition close to the heave and pitch natural frequencies, while the variation of $\bar{R}_W$ in the ballast condition stayed insignificant over the major range of the studied wave encounter frequencies. Interestingly, two peaks in each loading condition were seen for the added wave resistance coefficient. Although in the fully-loaded condition one of the peaks in the longer waves was dominating, the peaks were rather equal in size in the ballast condition. The main peaks of C_{AW} in the fully-loaded condition were larger for the higher Froude numbers and moved towards longer waves. The secondary peaks of C_{AW} were seen in short waves near $\lambda/L = 0.55$ in the fully-loaded condition and near $\lambda/L = 0.49$ in the ballast condition. It is believed that these secondary peaks were related to the secondary peaks of θ_1 as well as the abrupt transitions of the 1st harmonic phase difference between heave and pitch motions observed near such wave lengths. Further investigations for different hull types and operational conditions are recommended for better understanding of the behavior of ships near $\lambda/L \approx 0.5$.

C_{AW} at each Froude number in both loading conditions indicated approximate linear

relation between the added wave making resistance and the wave amplitude squared in the FNPF computational results, except in relatively short waves and near the peaks. However, this quadratic wave amplitude dependency of added wave resistance was not well identified from the experimental data in the ballast condition. Moreover, from the potential flow computations in both loading conditions, approximately linear correlations were observed for the 1st and 2nd harmonic amplitudes of the wave making resistance (R_{W1} and R_{W2}) against the wave amplitude and the wave amplitude squared, respectively.

Although the computed motions in the FNPF method were comparable to the measurements, the resistance results were arguably less accurate in some conditions. The averaged absolute error of FNPF computational results in terms of percentage of the experimental values in both loading conditions for surge, heave and pitch 1st harmonic amplitudes were 34.6%, 19.6% and 17.1%, respectively. When the effects of actual measured wave height in the model tests were taken into account, the average absolute error of the non-dimensional 1st harmonic amplitudes of surge, heave and pitch motions reduced to 26.2%, 18.1% and 11.8%, respectively. On the other hand, the averaged absolute errors associated with the mean wave making resistance and added wave resistance coefficient (considering the actual incident wave height in the experiments) were found to be 25.0% and 24.3%, respectively. Generally, numerical errors in conjunction with the discretization errors as well as the potential flow approximations and the use of empirical formulas, such as ITTC-57 model-ship correlation line, are the main sources which contribute to discrepancy between the computed and the measured results. Moreover, the uncertainty related to the experimental data as well as the differences between the experimental and numerical setups (6DOF self-propelled against 3DOF bare hull) in this study should not be forgotten. The frictional resistance and thrust deduction factor in waves were assumed to be equal to those of calm water. However, the interaction effects between waves, hull and propulsion system may dispute the validity of these assumptions. Based on a simple approximations in the FNPF solver, the change of frictional resistance in presence of waves was found to be less than 2% of the respective calm water values. Supplementary investigations on the change of thrust deduction factor as well as frictional resistance in the presence of waves by higher fidelity viscous flow methods are encouraged.

The FNPF computational cost for each simulation was approximately 20-80 core-hours which lies between the computational cost required by lower fidelity methods (often with lower accuracy) such as methods based on Strip Theory and higher fidelity methods such as viscous flow solvers. Although the FNPF computational cost is considerably lower than the cost of higher fidelity methods, yet the results are in a good agreement with the experimental data. Therefore, the utilization of the FNPF methods in prediction of the overall performance of ships in regular head waves is found to be computationally efficient and cost-effective.

5

Viscous Flow Simulations

In this chapter, the application of viscous flow methods in solving ship performance prediction in calm water and regular head waves is investigated. This is considered as a forward step in the approach towards the main objectives of this thesis provided in Chapter 1. This step is inline with reducing the level of simplifications considered in the problem of ship hydrodynamics performance by using higher fidelity solvers to shed more light into physics of ship performance in calm water and waves. Extensive verification and validation exercises of the employed viscous flow RANS solvers are performed and the ship hydrodynamic responses and nominal wake are analyzed thoroughly. Understanding of the variation of nominal wake in waves (due to ship motions and waves orbital velocities) in comparison to calm water condition provides an important insight into the propeller performance and power prediction in such conditions, hence increasing the opportunities of a more optimized propulsive efficiency and propeller design.

In the following, first, a summary of the initial attempt for studying the LDP vessel performance using a RANS solver is provided. The challenges in terms of finding a robust numerical setup and performing wake validation are briefly explained. Then, the key motivations are stated for replacing the investigated vessel by a tanker vessel followed by an extensive experimental data set. From that point onward, the numerical investigations in this chapter concerns the tanker vessel.

5.1 Initial Attempt

At an earlier stage, some operational conditions of the LDP vessel were selected to be studied in a viscous flow solver. The preliminary results of such investigations are already published in Irannezhad et al. (2019a,b).

The LDP vessel in these investigations was appended with a shaft and an asymmetric rudder and free only in heave and pitch (2DOF). The propeller (diameter = 0.26 m)

was not modeled in the simulations. The aim here was to first validate the LDP vessel computed heave and pitch motions as well as its resistance due to regular head waves against the experimental data, then compare the results to that of potential flow methods discussed in Chapter 4 and finally, to analyze the time-varying wake field and compare it in different wave conditions in the viscous flow solver. The ship performance was studied in fully-loaded operational condition at $Fr = 0.10$ in calm water as well as two regular head waves both with height of $H/L = 0.028$ and lengths of $\lambda/L = 0.70$ and 0.91, see Table 4.3.

The viscous flow simulations were performed in Simcenter STAR-CCM+ (version 13.06) using an unsteady Reynolds-Averaged Navier-Stokes (RANS) approach. A finite volume method together with a segregated approach for coupling velocity and pressure fields were used for solving the conservation equations for mass, momentum as well as turbulence quantities. A second order spacial discretization scheme was used.

In order to simulate the vessel motions, the Dynamic Fluid Body Interaction (DFBI) module was used. The DFBI Rotation and Translation model was used in order to enable the RANS solver in STAR-CCM+ to compute the vessel motions from the fluid excitation forces and moments as well as the gravity force. The Planar Motion Carriage mechanism was used within the DFBI Rotation and Translation model, in order to simulates the hull free to heave and pitch (2DOF) while it was translating with a prescribed constant speed (ship forward speed) in the longitudinal direction (surge fixed).

The 5th order Stokes waves were considered. In order to achieve a robust simulation setup for wave propagation in STAR-CCM+, the best practices provided by Peric' (2017) were complied. The aim was to minimize the wave propagation simulation issues, such as amplitude reduction and period change during propagation, disturbances (wiggles) on the free-surface and reflection at boundaries.

The Volume of Fluid (VOF) model is used to capture the free surface. The High-Resolution Interface Capturing (HRIC) scheme (second order convection scheme), Muzaferija and Peric' (1998), was used in VOF simulations to maintain a sharp interface between the incompressible fluid phases (water and air).

Mesh generation was performed using the automatic mesh generation tool in STAR-CCM+. The trimmed hexahedral meshes with local refinements near the free-surface as well as near the hull together with prism layers along the hull surface were used. Overset method consisting an overset region and a background region with specific treatment of cell sizes near the overlapping region was used to discretize the computational domain. The prism layers were placed in such a way that the non-dimensional wall distance y^+ remains above 30 over the major part of the hull wetted surface area during the simulation, hence wall functions utilization.

Approximately 16 cells were considered per wave height and the aspect ratio of cells near free surface in the longitudinal direction was twice of the vertical cell size, hence approximately 200 and 260 cells per wave length for $\lambda/L = 0.70$ and 0.91, respectively. Due to the asymmetric geometry of the rudder, no symmetry plane was considered. The generated grid near free surface was different between calm water and regular head wave simulations, therefore, the total number of cells was 8.1 M and 17.6 M in calm water and regular head waves, respectively. An overview of the background mesh for the simulations in regular head waves and the computational domain sizes are shown in Fig. 5.1 in which

the applied boundary conditions are also given. The pressure outlet boundary condition for the simulations in waves was at the top boundary but in the simulations in calm water it was imposed on the outlet boundary.

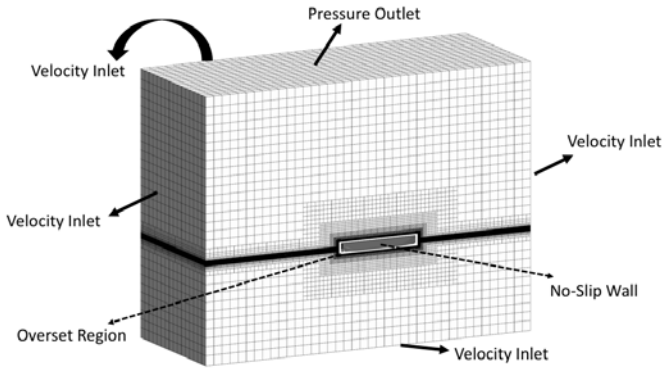

(a) Grid overview.

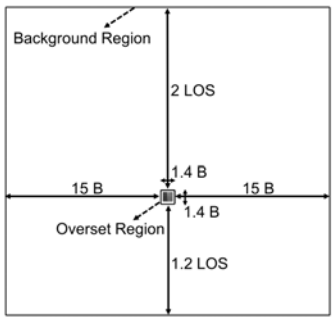

(b) Front view.

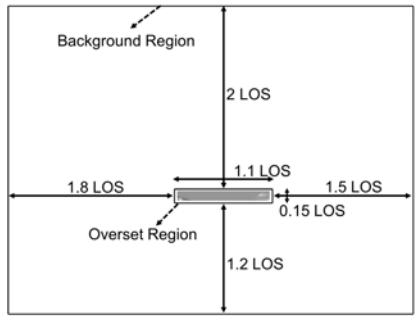

(c) Side view.

Figure 5.1: Overview of the background mesh, dimensions of the computational domain and the applied boundary conditions for simulations in regular head waves. LOS is approximately similar to the ship length L.

For simulations in waves, the wave forcing capability was applied to all of the velocity inlet vertical boundaries in order to force the solution of the discretized Navier-Stokes equations towards the theoretical 5th order Stokes wave solution over a distance approximately similar to the ship length L from the boundaries. For simulation in calm water, the wave damping capability was used in order to minimize the wave reflection from the boundaries.

The Realizable $k-\varepsilon$ turbulence model together with all y^+ wall treatment was used for calm water simulations. On the other hand, based on the best practices for numerical wave propagation simulations given by Peric' (2017), the Standard Low-Re $k-\varepsilon$ turbulence model was used for simulations in regular head waves in order to minimize the growth of turbulent viscosity on free surface.

An implicit unsteady solver with a second order temporal discretizational scheme (time-step of 0.003 s) for simulation in waves and a first order temporal discretizational scheme (time-step of 0.02 s) for simulation in calm water were used. Last but not least, 40 and 10 maximum number of inner iterations for each unsteady time step were considered in the simulations for calm water and regular head waves, respectively.

The calm water total resistance from the towing experiments at $Fr = 0.10$ was about 15.8 N and from CFD simulations it was computed as 14.6 N. The measured sinkage and trim from the self-propulsion model tests were approximately -0.003 m and 0.018 deg, while from the simulations they were computed as -0.002 m and 0.114 deg. A good agreement was seen considering the very small magnitudes of motions and the possible uncertainties involved in the measurements, as discussed in Section 4.4.

The quality of the propagated numerical waves was studied in order to ensure that the incident waves were as similar as possible to the theoretical waves introduced at the boundaries. It was found that the wave height deviates slightly from the theoretical value but in an acceptable scope. The 1st and 2nd harmonic amplitude of the wave elevation was under-predicted by 3% and 6%, respectively.

The absolute value of errors (from the self-propelled experimental data in which the measured wave amplitude effects were taken into account) for z_1/A and θ_1/kA were approximately 14% and 11% in $\lambda/L = 0.70$ and 19% and 20% in $\lambda/L = 0.91$. The average absolute errors for z_1/A and θ_1/kA from the FNPF simulations were approximately 18% and 12%, respectively. For total resistance, the errors of the viscous flow solver were 18% and 14% for shorter and longer waves, respectively, which are lower than the averaged absolute errors of wave making resistance computations in the FNPF solver (25%). Beside the sources of discrepancies thoroughly discussed within Chapter 4 and summarized in Section 4.6, in the current viscous flow simulations the surge motion was fixed which might be counted as an extra source of discrepancy.

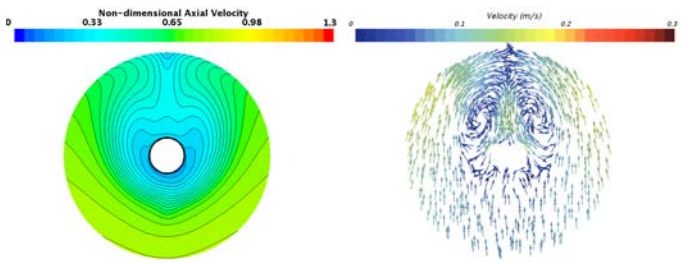

(a) Non-dim. axial contour. (b) Transverse vectors.

Figure 5.2: Velocity components on the propeller disk in calm water.

The nominal wake was investigated on a hull-fixed propeller plane. The nominal wake varied significantly during one encounter period responses of the ship and its mean value slightly deviated from the calm water value, however, a different distribution of the axial an radial velocity components were observed. Strong correlation between the pitch motion and the wake field dynamics was seen. The wake fraction was at its minimum (meaning that the inflow velocity into the propeller disk was close to free stream velocity) when

the pitch motion was close to zero and the hull stern was just about to move downwards into the water. On the other hand, the wake fraction was at its maximum when the pitch motion was zero but the hull stern moving upwards out of water.

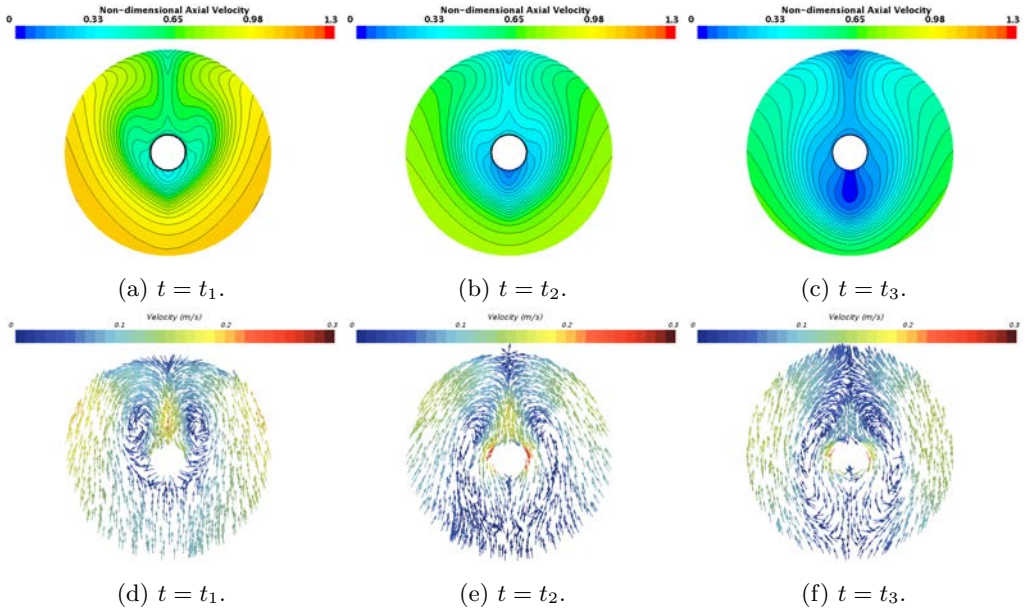

(a) $t = t_1$. (b) $t = t_2$. (c) $t = t_3$.

(d) $t = t_1$. (e) $t = t_2$. (f) $t = t_3$.

Figure 5.3: Non-dimensional axial velocity contours and transverse velocity vectors for $\lambda/L = 0.70$ at three instances of response.

The non-dimensional axial velocity contour in the shaft direction (perpendicular to the propeller plane) as well as the transverse velocity vectors for the simulation in calm water are shown in Fig. 5.2. Moreover, after obtaining the transient surface averaged wake fraction from the simulations in waves, three time instances of the lowest $t = t_1, t_1'$, the mean level $t = t_2, t_2'$ and the highest $t = t_3, t_3'$ surface averaged wake fraction are extracted and used to plot the non-dimensional axial velocity contours and the transverse velocity vectors in waves. These contour plots are shown in Fig. 5.3 and Fig. 5.4.

The bilge vortex found by the same Q-criterion in different conditions is shown in Fig. 5.5. The bilge vortices in waves showed a more dynamic behavior in comparison to calm water. They became stronger by increasing wave length. The position where the bilge vortices hit the propeller disk in calm water was more and less stationary, while they considerably moved up and down in the propeller disk when the waves were present. The other interesting phenomenon in waves was the existence of a secondary vortex system which was caused by the propeller shaft and enters the propeller disk.

To sum up, the motion and resistance responses were to some extent comparable to the EFD data but there is no wake measurements to make a comparison for the nominal wake. However, a question may raise that how trustworthy were the applied numerical method and simulation setups. In literature, the validity of the incorporated discretization schemes and modelling assumptions in the state-of-the-art CFD methods

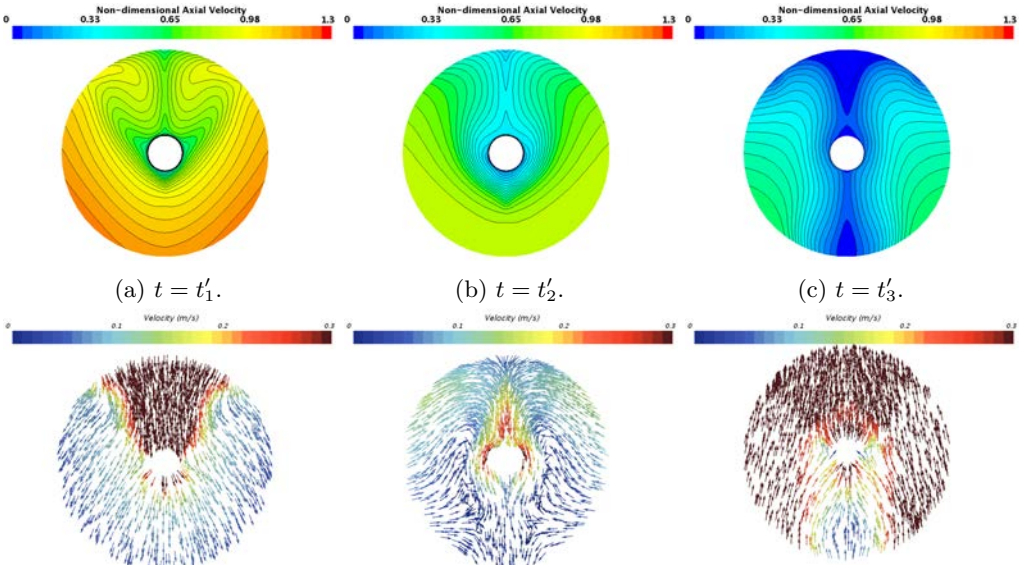

(a) $t = t'_1$. (b) $t = t'_2$. (c) $t = t'_3$.

(d) $t = t'_1$. (e) $t = t'_2$. (f) $t = t'_3$.

Figure 5.4: Non-dimensional axial velocity contours and transverse velocity vectors for $\lambda/L = 0.91$ at three instances of response.

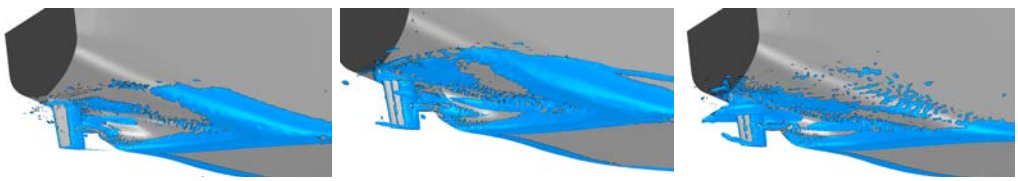

(a) Calm water. (b) $\lambda/L = 0.70$ at $t = t_1$. (c) $\lambda/L = 0.91$ at $t = t'_1$.

Figure 5.5: The bilge vortex found by Q-criterion = 7.5 $/s^2$.

are often overlooked and the method accuracy is mainly assessed through the validation of the results based on the respective model test data. However, as it is mentioned in Chapter 3, verification is needed to evaluate the possible numerical uncertainties in such methods. Furthermore, the choice of turbulence model which was made in order to follow best practices of numerical wave propagation in STAR-CCM+ can be questioned, as this turbulence model might not be a good candidate for nominal wake computations.

Therefore, it is decided to perform the viscous flow investigations for the MOERI tanker (KVLCC2) of which there are nominal wake measurements available in calm water and regular head waves, hence possibility of nominal wake validation. Moreover, KVLCC2 is chosen because the eventual objective of the research is to study the propeller-appended simulations and advance experimental wake measurements are available for KVLCC2 in such modes.

In the following, the main focus is set on the verification of numerical method in calm

water and waves as well as the sophisticated nominal wake, which is inherently dependent on the hull resistance and its motions. To this end, extensive attempts have been made to investigate numerical wave propagation without the presence of the hull using a more robust turbulence model for wake computations. The verification analysis are also carried out for KVLCC2 in calm water and regular head waves. In this thesis, the main focus of the uncertainty analyses is on the systematic grid convergence study.

5.2 Vessel Geometry and Operational Conditions

The KVLCC2 bare hull in model-scale (scale factor = 100) appended with a shaft (dummy hub) is employed in this study. The ship main particulars in the fully-loaded operational condition are given in Table 5.1. Since the nominal wake analysis is carried out mainly at the propeller plane, the particulars of the propeller are also provided in Table 5.1.

Table 5.1: Model-scale KVLCC2 vessel bare hull and propeller main particulars (scale factor = 100).

Symbol	Value	Unit	Denotation
			Bare Hull
L	3.2	(m)	Length between perpendiculars
B	0.58	(m)	Breadth at mid-ship
T_F	0.208	(m)	Draft at fore perpendicular
T_A	0.208	(m)	Draft at aft perpendicular
∇	0.312622	(m^3)	Volume displacement
Δ	312.028	(kg)	Mass displacement
S	2.7194	(m^2)	Bare hull wetted surface area at rest
C_B	0.8098	$(-)$	Block coefficient
L_{CG}	1.71136	(m)	Longitudinal position of COG from aft perpendicular
V_{CG}	0.186	(m)	Vertical position of COG from Keel
K_{yy}	0.8	(m)	Mass radius of gyration around Y-axis (pitch)
			Propeller - KP458 (based on Osaka University Towing Tank model setup)
D_P	0.0986	(m)	Propeller diameter
D_{Hub}	$0.155D_P$	(m)	Hub diameter
X_P	$0.02L$	(m)	Longitudinal position of propeller centre forward aft perpendicular
Z_P	$0.046875L$	(m)	Vertical position of propeller centre under water line

The hydrodynamic performance of the vessel operating in fresh water with the density of $\rho = 998.1\ kg/m^3$ and the kinematic viscosity of $\nu = 1.002 \times 10^{-6}\ m^2/s$ is investigated at the ship design speed (Froude number of $Fr = U/\sqrt{gL} = 0.142$), hence Reynolds number of $Re = UL/\nu = 2.546 \times 10^6$. The investigations are carried out in calm water and in three regular head waves with the same wave height $H = 0.06\ m$ and three different wave lengths $\lambda/L = 0.6$, 1.1 and 1.6.

A carriage-fixed reference frame as well as a ship-fixed reference frame are considered and thus two different coordinate systems are defined. The coordinate systems at the initial position of the ship are shown in Figure 5.6. The carriage-fixed reference frame is considered to move in longitudinal direction with the ship design speed. On the other hand, the hull-fixed reference frame follows the ship motions and its actual speed. One Cartesian coordinate system in each reference frames are defined at the ship initial position

of COG (CF_{COG} and HF_{COG}). Both coordinate systems initially have X-axis pointing towards ship advancing direction, Y-axis towards ship portside and Z-axis pointing upwards. While the axes directions always remain the same for the coordinate system in the carriage-fixed reference frame CF_{COG}, they change based on the ship motions for the coordinate system in the hull-fixed reference frame HF_{COG}.

The motions of the ship are defined at its COG with respect to these reference frames. Consequently, positive surge motion occurs when the COG moves in the direction of the ship's forward speed. Positive heave motion is defined as when the COG moves upwards and positive pitch motion is defined as when the ship's bow moves downwards (or stern moves upwards).

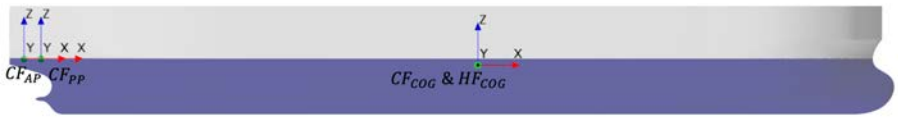

Figure 5.6: Initial locations of the considered coordinate systems.

Moreover, two planes at the ship aft perpendicular and its propeller plane are defined in the carriage-fixed reference frame in order to study the nominal wake of the hull in those locations. Therefore, extra coordinate systems (CF_{AP} and CF_{PP}) are defined in the carriage-fixed reference frame similar to the aforementioned coordinate system at COG but with the origins at the initial ship design waterline and plane locations, see Figure 5.6. The carriage-fixed wake analysis is carried out in these coordinate systems which move with the ship design speed irrespective of the ship actual speed or its motions.

5.3 Experimental Method

The experimental model tests were carried out in Osaka University Towing Tank (OU). The tank (100 m long, 7.8 m wide and 4.35 m deep) is equipped with a drive carriage running from 0.01 to 3.5 m/s. It is quipped with a plunger-type wave maker with capability of generating regular and irregular waves up to 500 mm height and 0.5–15 m length as well as an automated wave damper system and wave dampening beaches at the tank's end. In this case study, the utilized experimental data for KVLCC2 in calm water and regular head waves are divided into two main data sets (called EFD_1 and EFD_2 henceforth) from an extensive test campaign led by OU. In these tests, the 2-Dimensional Stereo Particle Image Velocimetry (SPIV) system was used to measure the velocity distribution at different planes. Detailed information for the first data set EFD_1 can be found in Hayashi (2012), Wu (2013), Sadat-Hosseini et al. (2013) and Kim (2014) and for the more recent data set EFD_2 in Mwangi (2021). The experimental setups were relatively similar in these data sets.

The wooden KVLCC2 model (scale factor = 100) was manufactured in OU, see Figure 5.7a. The model tests were carried out in 3 Degrees of Freedom (3DOF) in which the model was free in surge, heave and pitch, except in a few tests in calm water in which the

surge motion was fixed.

In 3DOF tests, the model was free to surge while it was towed with a light weight carriage connected to the main carriage through a weak spring system, as sketched in Figure 5.7b. The spring stiffness $K = 98\ N/m$ was chosen to avoid resonance and interfere of the spring natural frequency with surge motion frequency due to waves. An external constant force F_0 (obtained through a set of preliminary tests to keep the calm water surge and the mean surge in waves close to zero) was applied to avoid large spring stretch in each operational condition. F_0 and K were mimicked by a servo motor. Unfortunately, the applied F_0 is not available in any of the reports from the experiments.

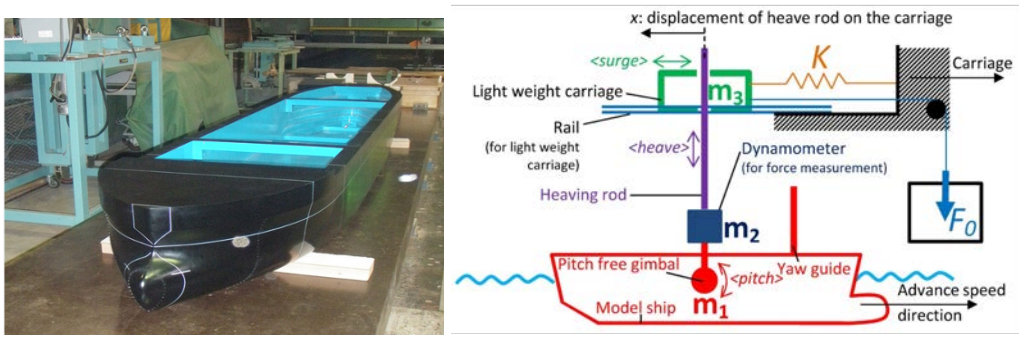

(a) Manufactured KVLCC2 model. (b) Test setup for free surge conditions.

Figure 5.7: Experimental setup and KVLCC2 model, Kim (2014).

A pitch free gimbal was installed in the hull COG and connected to the carriage by a heaving rod. A load cell dynamometer was installed above the gimbal for force measurements. The hull motions were measured using three potentiometers and the incident wave height was measured by a servo type wave gauge at some distance in front of the fore perpendicular (4.425 m in front of the heaving rod in EFD_1 and 3.52 m or 3.314 m in front of fore perpendicular depending on the test type in EFD_2). In both data sets, it is mentioned that the actual measured incident wave height at some tests were different from the target ones, possibly due to the performance of the wave generator and wave dampener systems. This will be discussed thoroughly later on. The sampling rate of the equipment was 100 Hz. In such experimental setup, the masses of the hull plus pitch free gimbal ($m_1 = 306.2\ kg$) as well as the dynamometer mass ($m_2 = 6.4\ kg$) were involved in the hull motions ($m_1 + m_2 \approx \Delta$), while the mass of the light weight carriage ($m_3 = 2.5\ kg$) was only involved in surge motion.

An SPIV system was fixed on the carriage and the model moved around the original position with wave encounter frequency and the spring natural frequency. The details of the experimental SPIV setup and equipment can be found in the aforementioned references for each data set. This system can take particle image not only at a certain interval but at a certain moment by using external trigger signals. The operational conditions, measurement planes and trigger were different in different data set. The major peculiarities caused by these are discussed the subsequent sections.

5.3.1 SPIV in EFD_1

In EFD_1, no information is found about the water temperature, hence the Reynolds number in this data set is assumed to be equal to the design value. The plane of measurements in this data set was fixed on the carriage at the initial position of the propeller plane. In calm water, approximately 1000 instantaneous velocity distribution frames were averaged to present a single frame. Unfortunately, the raw SPIV data is not found for calm water in EFD_1 and only a screenshot from Kim (2014) can be found. In waves, the trigger of the SPIV system was set in accordance with the phase of the heave response of the model.

The SPIV measurements were carried out in all three wave lengths. The goal was to capture the wake at heave phases of 0°, 45°, 90°, 135°, 180°, 225°, 270° and 315° in $\lambda/L = 0.6$, as well as phases of 0° , 30°, 60°, 90°, 120°, 150°, 180°, 210°, 240°, 270°, 300° and 330° in $\lambda/L = 1.1$ and phases of 0° , 60°, 120°, 180°, 240°, and 300° in $\lambda/L = 1.6$. A heave synchronizer system was introduced in order to find such heave phases during the test runs. Heave was chosen because of its relatively stable behavior during different runs. The system included a laser sensor fixed on the towing carriage and a marker plate installed on the heaving rod following the heave motion of the hull, see Figure 5.8.

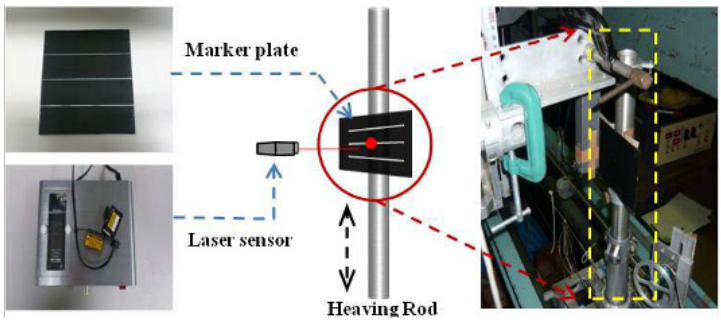

Figure 5.8: Heave synchronizer system for SPIV trigger in EFD_1, Kim (2014).

A series of parallel horizontal lines were drawn on the marker plate (representing different heave phases) in order to be detected by the laser sensor and hence sending a signal to trigger the SPIV measurements. Different groups of phases (lines on the marker plane) were considered in each run. Only the PIV data immediately after the start of measurements were used (due to irregular motions due to reflected waves over time). Moreover, the data from the tests that the surge motion was not controlled and large even from the beginning of experiment were excluded. Therefore, different number of incident waves were considered for each phase. In EFD_1, approximately 200 frames were averaged to obtain each phase of the SPIV data in waves.

In order to find the location of the phase lines on the marker plate, preliminary experiments were carried out to find the heave mean and first harmonic amplitude in each wave length. Then, the centre line was set to capture the heave mean value and the location of other phase lines were derived by calculating the expected instantaneous heave motion $z_{_{plate}} = \bar{z}_{_{plate}} + z_{1_{plate}} \sin(\phi_{_{desired}})$ using the results of the preliminary

experiments. $\bar{z}_{_{plate}}$ was found to be -0.0030, -0.0030 and -0.0028 m and $z_{1_{plate}}$ was found to be 0.0025, 0.0193 and 0.0256 m for $\lambda/L = 0.6$, 1.1 and 1.6, respectively. It is very important to notice that the heave responses might change during each run (e.g., due to the actual incident wave) and the actual measured heave might differ from the expected one. This would introduce an uncertainty to the actual instances of SPIV measurements.

5.3.2 SPIV in EFD_2

In EFD_2, it is very important to notice that the tests in which the motions and resistance were measured are different from those of SPIV measurements. This may introduce a source of uncertainty into the measurements in this data set, as the response of the hull might be different in different conditions. Moreover, the water temperature for the motion and resistance measurements and hence the respective Reynolds number ($Re = 1.9141 \times 10^6$) were different from those for SPIV measurements ($Re = 2.2519 \times 10^6$). The plane of measurements in this data set was fixed on the carriage at the initial position of the aft perpendicular. The plane was moved from the propeller plane to the aft perpendicular due to the disturbing reflections from the dummy hub. The calm water SPIV measurements were carried out in fixed surge conditions (2DOF) and approximately 230 velocity distribution images collected and averaged. The measurements were at $Re = 2.6159 \times 10^6$. In waves, the trigger in the SPIV system was based on the measured wave height at the wave gauge placed at a certain distance in front of the model.

The SPIV measurements in waves were only performed for $\lambda/L = 1.1$ and 1.6 in EFD_2. The trigger was based on the incident wave elevation at the wave gauge at 4 phases of 0° (zero up crossing of wave at wave meter), 90°, 180° (zero down crossing of wave at wave meter) and 270° for each λ/L. The wave gauge location was different in the tests in which the motions and resistance were measured (3.52 m in front of fore perpendicular) to that of SPIV measurements (3.314 m in front of fore perpendicular). For each phase, the measurements were carried out in two runs in which the measurement plane was moved vertically to cover a larger area due to the large ship motions relative to the carriage. Approximately 180 images were collected and averaged for each phase. One source of uncertainty of results in this data set raise from the fact that the measured wave elevation may differ from the expected one in some tests which might affected the exact instances of SPIV measurements.

5.4 Numerical Method

The numerical simulations are performed by a commercial CFD solver, Simcenter STAR-CCM+ (version 2020.3), using a RANS approach. The continuous equations are discretized using a Finite Volume method. A segregated approach for coupling velocity and pressure fields is used for solving the conservation equations for mass, momentum as well as turbulence quantities. A second order spacial discretization scheme is used.

The VOF multiphase model was used as the free-surface capturing technique. The High-Resolution Interface Capturing scheme (HRIC) Muzaferija and Peric' (1998) was used in VOF simulations to maintain a sharp interface between the incompressible fluid phases. As it is mentioned by Perić and Abdel-Maksoud (2018), Berndt et al. (2021)

and Perić et al. (2022) case-dependent parameters should be tuned for minimizing the reflections from the boundaries of the computational domain and improving the numerical simulations of flows with free surface waves. Therefore, different user-defined parameters under the HRIC scheme (e.g., the angle factor of 0.15) are tuned based on the preliminary simulations carried out for the regular head waves under study in this thesis. For more details about such parameters including the angle factor which affects the discretization of the volume fraction, see Perić and Abdel-Maksoud (2020) and STAR-CCM+ User Guide.

The turbulent viscosity is modeled using the $k-\omega$ SST turbulence model (using all y^+ wall treatment) via solving additional transport equations for turbulent kinetic energy k and specific dissipation rate ω. The implementation of this turbulence model in STAR-CCM+ is based on Menter (1994). In order to take into account the anisotropy of the turbulence, the linear Bossenisque approximation, given in Equation 2.4, is extended by adding nonlinear functions of the strain and voticity tensors to derive a quadratic constitutive relation. For more details read STAR-CCM+ User Guide.

The 5th order Stokes waves are considered in the simulations as they are found to be as a better resemblance of the real-world waves, Fenton 1985. In order to achieve a robust simulation setup for wave propagation in STAR-CCM+, comprehensive attempts are made to model wave propagation in an empty domain without the presence of the hull. The aim is to minimize the wave propagation simulation issues (e.g., amplitude reduction and period change during propagation, disturbances (wiggles) on the free-surface and reflection at boundaries) and estimate the scope of potential discrepancies from the analytical wave. Such estimations can explain the behavior of the ship in waves, due to the fact that the main excitation forces on the ship are exerted from the waves. It was presumed that the steepest wave is the most critical wave for numerical propagation modeling, hence only the wave with length of $\lambda/L = 0.6$ is considered for a quantitative investigation of the numerical waves characteristics along the computational domain.

5.4.1 Motion Modeling

In order to simulate the vessel motions, the DFBI Rotation and Translation model is used. The Planar Motion Carriage mechanism is used for the simulations in 2DOF (i.e., fixed in surge), however, 3DOF simulations are carried out using Free Motion model in the DFBI module. In 3DOF simulations, for numerical replication of the spring and light weight carriage effects which were present in the experiments, two external forces one for constant force $F_0/2$ and one varying spring force $-Kx/2 - m_3\ddot{x}/2$ are applied at the COG in the ship forward direction, in which K is spring stiffness, x is the instantaneous surge motion and $\ddot{x}$ is the instantaneous surge acceleration.

Since F_0 is not available from the experiments, an estimated F_0 is considered in each operational point approximately close to the total resistance of the ship in order to prevent large mean surge value. This can be counted as a source of discrepancy which will be discussed further in the thesis. Moreover, since in the simulations a symmetry boundary condition is considered at the ship centerline plane $Y = 0$, the experimental values of the spring stiffness and light weight carriage mass are divided by 2. It should be noticed that when the surge has a positive value based on the considered coordinate systems shown in Figure 5.6, the spring force $-Kx/2$ gets a negative value (in the opposite

direction of the ship forward speed) as the spring is compressed, see Figure 5.7. Moreover, in the experiments, the light weight carriage was coupled with the hull in the surge motion, while in the current simulation setup it is decoupled by using an external force of $-m_3\ddot{x}/2$ at COG. The surge acceleration during the simulations remains very small, hence insignificant effects are expected.

For the initial part of the simulations, it is very important to prevent any shock effects in the forces or large amplitudes of surge motion (i.e., large spring force), as it takes a very long time (increased computational costs) for such effects and oscillations to get dissipated. Therefore, quite long Release and Ramp times are considered under DFBI model. Release time in the DFBI model is defined as the time before calculation of body motion begins in order to allow the fluid flow to initialize. Ramp time is the time after release time in which the applied forces and moments to the body are increased gradually from zero to the expected values to reduce the shock effects.

5.4.2 Grid Generation

Unstructured grids including the trimmed hexahedral meshes with local refinements near the free surface and near the hull as well as prism layer meshes along the hull surface are generated using STAR-CCM+ automatic mesh generator. In order to perform a valid grid convergence study, several progressively refined grids should be generated where all grids should be exactly "geometrically similar". However, generating geometrically similar unstructured grids is extremely cumbersome, if not impossible. Therefore, in the current investigations, different cautions are taken into account to eliminate/diminish undesired grid refinement diffusion depths (transition zone between two local refinement zones) and also to generate "as geometrically similar as possible" set of unstructured grids. The computational domain in each grid is discretized employing an Overset Topology which consists an overset region and a background region with specific treatment of cell sizes near the overlapping zone (where the information is exchanged between the background and overset regions).

The simulations are mainly carried out for five different grid sets explained in Table 5.2. The wave propagation simulations in an empty domain without the presence of the hull are carried out for GS1-GS4 in which the effects of different local refinement zones as well as the quality of the cell size and overset interpolations in the overlapping zones are evaluated for the steepest wave ($\lambda/L = 0.6$). In GS4, a sinusoidal pitch motion with an amplitude of 3 *deg* and a frequency equal to the wave encounter frequency is predefined for the overset region to examine the overset interpolations for a moving overset region. These simulations are mostly carried out in three different computational domain widths, i.e., Quasi-2D (only one cell in Y direction), Small Width SW-3D (one third of the full domain in Y) and Full Width FW-3D (full domain size in Y). The reason behind choosing one third of the domain size for the SW-3D case is to eliminate undesired grid refinement diffusion depths that may be introduced by the grid generator.

Although the Quasi-2D simulations are computationally much cheaper than 3D simulations, it was found that the Quasi-2D results for the wave propagation simulations are not necessarily similar to that of the 3D cases, therefore, no further attempts were made to continue such simulations. On the other hand, the SW-3D simulation results were

Table 5.2: Grid sets details. The simulation types are Wave Propagation (WP) and Hull Performance (HP).

Grid Set	Sim. Type	Regions		Local Refinement Zones					Prism Layer
		Back-ground	Overset	Free Surface	Kelvin Wedge	Overl-apping	Around Overset	Inside Overset	
GS1	WP	✓	–	✓	–	–	–	–	–
GS2	WP	✓	–	✓	✓	✓	✓	–	–
GS3	WP	✓	✓ Restrained	✓	✓	✓	✓	–	–
GS4	WP	✓	✓ Predefined Motion	✓	✓	✓	✓	–	–
GS5	HP	✓	✓ Hull Motion	✓	✓	✓	✓	✓	✓

quite similar to those of FW-3D. Therefore, in order to reduce the computational costs, it is decided to perform wave propagation simulations only in SW-3D. On the other hand, the hull performance simulations carried out for GS5 only in FW-3D in order to study the ship responses in calm water and three regular head waves ($\lambda/L = 0.6$, 1.1 and 1.6). Consequently, the grid for calm water simulations was similar to that of waves, which is not a common practice per se but required for obtaining the current study objectives. The same is considered in the PhD thesis by Sigmund (2019).

Wave Propagation Simulations Grid Sets

For GS1-GS4, in each grid set, four systematically refined grids are considered which are determined by the refinement levels $n = 0.50$ (coarsest), 1.00, 1.50 and 2.00 (finest). Trimmed hexahedral meshes (isotropic volume meshes) are generated in both background and overset regions. For isotropic volume meshes, every two neighbouring cells with the same size in the grid $n = 1.00$ are converted into $2n$ cells in each direction (X, Y and Z), hence substituted by $2n^3$ cells. Strict cautions were taken into account for defining the dimensions of different local refinement zones and the number of neighbouring similar cells in each direction in each local refinement zone in order to fit integer number of cells in each direction as a result of multiplication $2n$ and force the local refinements to occur exactly in the defined local refinement zones. Moreover, the refinement ratios between such local refinement zones are defined in order to prevent any missing/extra refinements from the grid generator.

All the effort was made to control the automatic grid generator and eliminate any undesired transition zone between two local refinement zones, hence deriving "geometrically similar" sets of grids. Figure 5.9 shows the grids ($n = 1.00$ and 1.50) in GS2 in FW-3D domain where different local refinement zones are illustrated by different colors. It should be noticed that the wave propagation simulations are carried out in SW-3D domain and Figure 5.9 with FW-3D domain is shown only because of the illustration purposes. As the result of strict cautions in generating geometrically similar grids, the total number of

cells in SW-3D domain in each grid in GS1, GS2 and GS3 (equal to GS4) is **precisely** 984384, 4122656 and 5777696 multiplied by n^3, respectively.

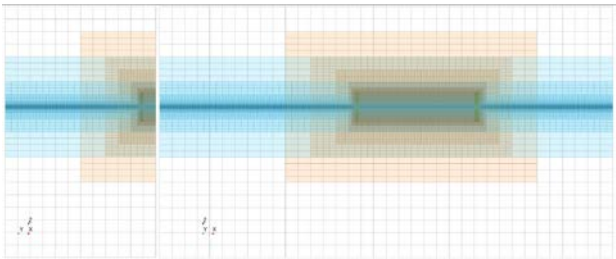

(a) $n = 1.00$, front and side view.

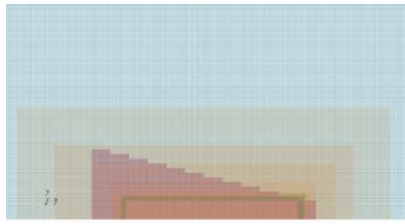

(b) $n = 1.00$, top view.

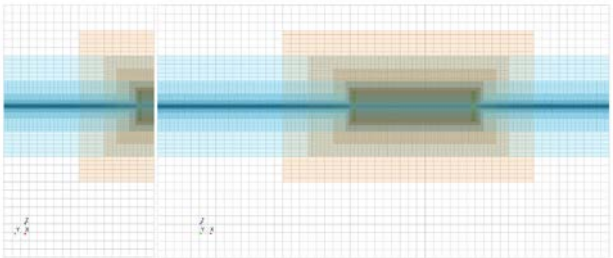

(c) $n = 1.50$, front and side view.

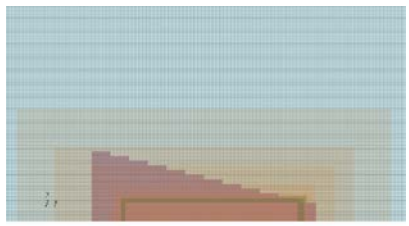

(d) $n = 1.50$, top view.

Figure 5.9: Overview of Free Surface Around Overset Overlapping Kelvin Wedge local refinement zones in $n = 1.00$ and $n = 1.50$ for GS2 in FW-3D domain.

From the free surface local refinement zone, based on the refinements in the vertical Z direction, $10n$ cells per wave height is considered for each grid. The cell aspect ratio of 4 in longitudinal X and transversal Y directions are considered in relative to the vertical Z direction. Consequently, there are $10n\lambda/(4H)$ cells per wave length for each wave in each grid.

Hull Performance Simulations Grid Set

For GS5 in which hull performance simulations carried out, there are two extra systematically refined grids added to the previous grid refinement levels and the six refinement levels are $n = 0.50$, 0.75, 1.00, 1.25, 1.50 and 2.00. In the wave propagation simulations in GS1-GS4, it was decided to have a factor of 2 similar cells in each direction in each local refinement zones to have integer number of cells generated as a result of $2n$ for $n = 0.50$, 1.00, 1.50, and 2.00, which worked totally fine. Thus, at some locations, directions and local refinement zones there placed only 2 similar cells. Consequently, at those locations there won't be integer number of cells generated from the grid generator for grids $n = 0.75$ and 1.25 in GS5 and there will be some undesired transition zones in the isotropic volume meshes. Consequently, these two extra refinement levels $n = 0.75$ and 1.25 are not exactly

geometrically similar (but marginally different) to the other ones in terms of the isotropic volume meshes.

On the other hand, in order to achieve geometrically similar anisotropic sub-layer (prism layer) meshes, the methodology presented by Crepier (2017) is complied. In this method, the total thickness of prism layers remains the same between the grids but both the first layer cell thickness Th and the growth ratio between the layers Gr are adjusted accordingly as,

$$Th_n = Th_1 \frac{1 - Gr_1{}^{\frac{1}{n}}}{1 - Gr_1}, \qquad Gr_n = Gr_1{}^{\frac{1}{n}}, \tag{5.1}$$

in which Th_1 and Gr_1 are the first layer cell thickness and the growth ratio for the grid $n = 1.00$. As a result, the total number of layers in each grid will be $N_n = nN_1$, in which N_1 is the total number of layers for grid $n = 1.00$. It was thus very important to choose a proper N_1 to have integer number of layers for all grids in GS5 from nN_1. An overview of the grids near the hull in GS5 and for two refinement levels are shown in Figure 5.10.

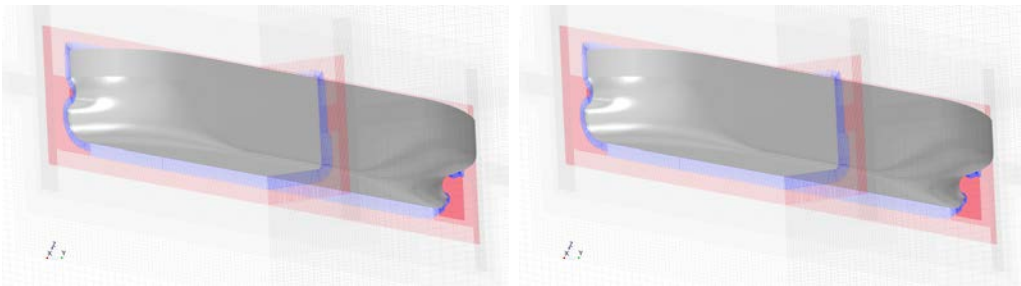

(a) n = 1.00. (b) n = 1.50.

Figure 5.10: Overview of the grids near the hull in GS5. Gray lines represents the mesh in the background region. Blue and red colors represent the isotropic and prism layer meshes in the overset region, respectively. Local refinement zones inside the overset can also be observed.

Furthermore, the prism layers are generated such that the non-dimensional wall distance y^+ remains above 30 and under 300 over the major part of the hull wetted surface area during the ship performance simulations (for all grids in GS5), hence a wall function is utilized for treatment of the near-wall region.

Although the effort has been made to generate geometrically similar isotropic and anisotropic sets of grids, the undesired transition zone between the prism layers and their neighbouring isotropic cells are inevitable in GS5. Therefore, the grids are "as geometrically similar as possible". Consequently, the total number of cells are 987823, 3591204, 7868343, 16101857 , 26542361 and 62866494 for $n = 0.50$, 0.75, 1.00, 1.25, 1.50 and 2.00, respectively, and they are **not** a factor of n^3. The calm water simulations as well as the simulations in regular head waves of $\lambda/L = 0.6$ and 1.1 are carried out in all six refinement levels n of GS5, while the simulations for the longest wave $\lambda/L = 1.6$ is only carried out in grid $n = 1.00$.

5.4.3 Computational Domain

An overview of the computational domain size and the imposed boundary conditions are shown in Figure 5.11. In order to analyze the numerical wave elevation, 16 wave probes (located at 4 X-positions and 4 Y-positions) are introduced and also shown in this figure. The longitudinal location of probes are, (1) at the end of wave forcing zone, (2) before the overset region, (3) within the overlapping zone and, (4) inside the overset region close to the hull fore perpendicular. Notice that the hull was not present in the wave propagation simulations in GS1-GS4 and the computational domain width was SW-3D.

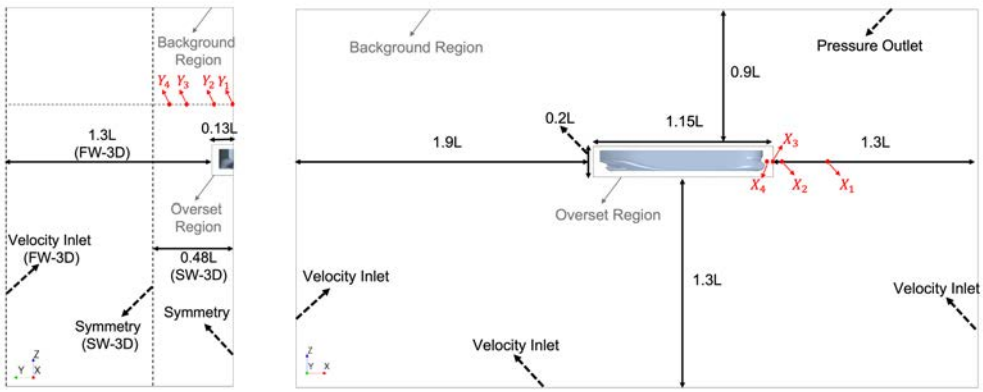

Figure 5.11: Computational domain size, applied boundary conditions and wave probes locations.

A wave forcing function is used in the vicinity (distance equal to L) of all vertical boundaries with velocity inlet boundary conditions in order to force the solution of the discretized Navier-Stokes equations, for wave propagation and hull performance simulations in regular head waves, towards the theoretical 5th order Stokes wave solution, and for calm water simulations, towards the still water solution, hence minimizing the wave reflection from the boundaries.

In a preliminary investigations, a Distance Weighted overset interpolation scheme was employed. However, later it was found that the interpolations quality was rather low and nonphysical vortices were generated at the overlapping regions which significantly affected the predicted forces acting on the hull. It was then found that higher order schemes are required for a better quality of interpolations, Lemaire et al. (2021). Therefore, the Least Square interpolation scheme were employed within the overset topology which marginally increases the required computational costs but introduces higher accuracy interpolations compared to the Distance Weighted scheme. More details can be found in STAR-CCM+ User Guide.

5.4.4 Time Step

An implicit unsteady solver is used with a second order temporal discretizational scheme (time step $t = 0.003/n$, hence similar Courant number between the grids in each grid set) for calm water and regular head wave simulations. The chosen time step results in Courant

numbers smaller than 0.3-0.4 on the free surface which is inline with the best practices for numerical wave propagation and also fulfills the ITTC (2014) recommendations. Last but not least, 20 maximum number of inner iterations for each unsteady time step is considered.

It should be noticed that the uncertainty analysis in this thesis is carried out in terms of grid convergence study, while a complete uncertainty analysis would include the combination of iterative and grid convergence studies. Therefore, conservative values are chosen for the time step size and maximum number of inner iterations to eliminate significant accumulating effects from the iterative convergence errors through keeping the Courant number constant between the grids, a conservative grid convergence analysis carried out. In order to confirm that the chosen time step size was conservative, some selective operational conditions and grids in GS5 were studied with a much smaller time step size in which no significant changes in the solutions were seen.

5.4.5 Uncertainty Analysis Method

The classical method for quantifying the uncertainty in a grid convergence study is Grid Convergence Index (GCI) by Roache (1998), which is the basis for many other verification methods (e.g., Stern et al. (2001), Xing and Stern (2010) and Eça et al. (2010)). The GCI method starts by determination of the grid convergence by Richardson Extrapolation (RE) in which the discretization error in a numerical solution expressed as power series. Two well-known verification methods in the ship hydrodynamic community are Factor of Safety (FS) by Xing and Stern (2011) and Least Square Root (LSR) by Eça et al. (2010). Both Methods are based on GCI and RE, while LSR takes into account the scatter in numerical solutions.

In this thesis the LSR method is employed to carry out the grid convergence study of ship responses in calm water and regular head waves. In this method, the order of accuracy and numerical error are determined by a curve fitting process which is designed for computations with a theoretical second order accuracy which is typically true in CFD computations of ship hydrodynamics. The numerical uncertainty analysis tool developed by Eça and Hoekstra (2014) and Eça et al. (2019) is used in this thesis. It is constructed for a formally second-order accurate method and it relies preferably on Richardson extrapolation (RE) and the Grid Convergence Index (GCI) to obtain the numerical uncertainty. The estimation of discretization error using RE is presented as,

$$\Phi_i - \Phi_0 = \alpha {h_i}^p, \tag{5.2}$$

in which Φ_i is the solution of grid i and h_i is the typical cell size, i.e., for 3D grids of this thesis defined as $h_i/h_1 = \sqrt[3]{No_{cell1}/No_{cell\,i}}$ where No_{cell1} is the number of cells for the finest grid. Then the estimation of discretization error requires the determination of the estimated exact solution Φ_0, observed order of grid convergence p and a constant for multiplication α. Such values are supposed to be derived in the least squares sense using data from at least 4 grids. The grids must be in the "asymptotic range" to guarantee that the leading term of the power series expansion (high order terms are neglected) is sufficient to estimate the error. Moreover, the grids should be geometrically similar, i.e., the grid refinement ratio must be constant in the complete field and grid properties

like the deviation from orthogonality, skewness, etc., must remain unaffected. In the current method, Eça and Hoekstra (2014) introduced three alternative error estimators. More information about the tool and the implemented methodology can be found in the respective references.

5.4.6 Post-Processing Techniques

Before post-processing the results of ship hydrodynamic responses in CFD computations, proper convergence should be achieved in order to ensure reliable CFD solution. In the case of implicit computations, convergence should be achieved not only within each time step, but also during the whole simulation time. The level of convergence can be assessed by monitoring the history of residual variations for the mass and momentum equations, ITTC (2014). Residuals indicate how far the present approximate solution is away from the perfect conservation of mass and momentum, hence quantifies the imbalance between the left and the right hand side of equations over all the computational points in the discritized equations.

For the simulations carried out in this thesis, a proper level of convergence achieved within each time step considering the conservative choice of maximum number of inner iterations for each time step. The recommended criterion for assessing the convergence in the whole simulation time is the drop of scaled residuals by several orders of magnitude off their initial values, ITTC (2014). However, in the investigations of ship hydrodynamic performance in calm water and regular head waves, the residuals exhibit an oscillatory behavior during the solution time due to the complexity of problem, hence such criterion may not be satisfied. Moreover, residuals do not necessarily relate to quantities of engineering interest in the simulation such as hydrodynamic forces and ship motion responses. Therefore, in this thesis, besides monitoring the residuals, the convergence is mainly assessed for the computed ship resistance. Therefore, different convergence criteria based on the ship resistance are defined at each operational point of the ship.

Convergence Criterion for Calm Water Simulations

In calm water simulations, the oscillatory behavior of the resistance signal (and also motions signals) should ideally vanish and the solution should converge to a single value. However, due to the unsteady nature of the problem this may never be achieved. Although the wake of the ship in calm water simulations can be unsteady, only the last time step of each simulation is used for wake comparison. This was because the unsteady effects were deemed insignificant in comparison to that of highly dynamic regular head waves. Moreover, the convergence to a single value not only requires an extremely long simulation time (high computational costs), but also from some point onward, it may not introduce any significant changes into the magnitude of the final value.

Therefore, a convergence criterion on the resistance signal is defined in order to estimate a trustworthy value of resistance and other responses while keeping the computational costs low. A calm water simulation is deemed converged when the Standard Deviation (STD) of the total resistance time history is below 2% of its Root Mean Square (RMS) for a defined time window of the signal tail. The choice of time window is dependent on

the signal oscillations. In Figure 5.12 a representative plot is shown for a resistance signal sample in calm water simulations.

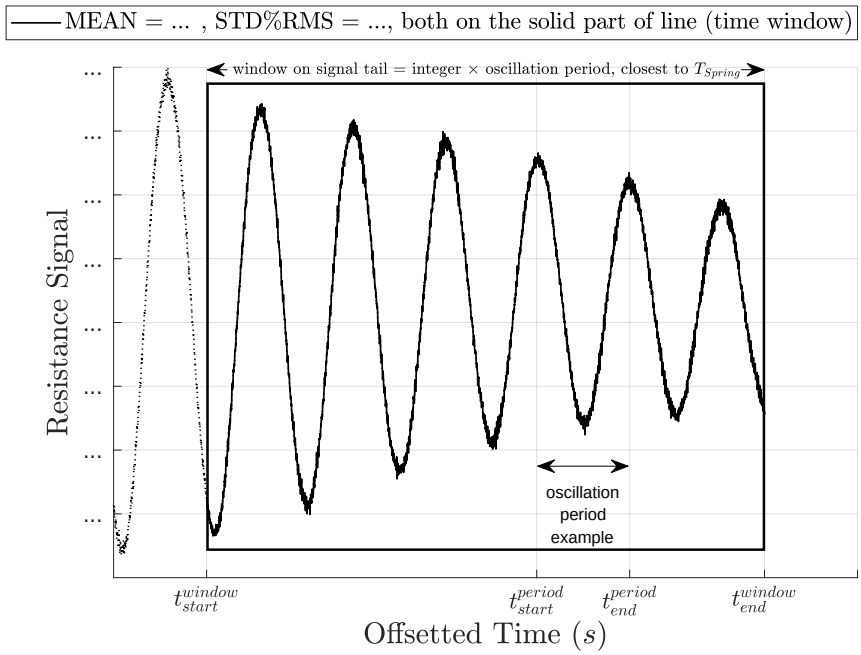

Figure 5.12: A representative resistance signal plot for explaining the convergence criteria and post-processing techniques in calm water.

The horizontal axis shows the offsetted time to see only the tail of the computed signal (more important part) and eliminate the initial part. A time window is selected on the signal tail and shown with a black rectangle. The signal consists a dashed line part starting arbitrarily at some instances of time and a solid line part starting from the start time of the selected time window and ending at the end of the signal which is also the end of the selected time window. In the plot legend, the mean value (MEAN) as well as the Standard Deviation in terms of percentage of Root Mean Square (STD%RMS) both calculated on the solid part of the line (i.e., the selected time window) are shown. Based on the defined criterion, if the STD%RMS is smaller than 2, then the simulation deemed converged and thus the MEAN value represents the calm water resistance value of the signal.

As it can be seen, the resistance signal exhibits an oscillatory behavior while the amplitude of oscillations decay when moving forward in time. However, the oscillations are rather periodic in time. An example of such oscillation period is shown in Figure 5.12. Therefore, proper time window can be a multiplication of an integer number to the oscillation period. Then there is a lower uncertainty involved in the calculation of the

MEAN value.

For calm water simulations, the oscillation period is approximately 2 s. On the other hand, the resistance signal in free surge condition is affected by the spring. The natural period of the spring is $T_{Spring} \approx 11.25$ s. Therefore, in order to partly include the effects of spring, a time window of $6 \times 2 = 12$ s is chosen which is rather close to the spring natural period.

Convergence Criterion for Regular Wave Simulations

In regular head waves simulations, the oscillatory behavior of the resistance signal (and also motions signals) should ideally become periodic (harmonic) with respect to the wave encounter frequency with consistent harmonic amplitudes. However, due to the unsteady nature of the problem, as well as other contributing factors such as the change of actual incident wave and the presence of the spring, this may never be achieved.

Therefore, a convergence criterion on the resistance signal is defined in order to estimate trustworthy outcomes from the computations of ship responses in regular head waves. The convergence criterion is defined on the "periodic moving average" of the total resistance time history, however, the hydrodynamics analysis of the time series is carried out for the original signal. The periodic moving average is a signal derived from the original resistance signal, in which its value at each instance of time is the average of the resistance signal values over a moving average window before that instance of time. In Figure 5.13 a representative plot is shown for a resistance signal sample and its periodic moving average signal in regular head waves simulations.

The horizontal axis shows the offsetted time to see only the tail of the computed signal (more important part) and eliminate the initial part. The black line is the original resistance signal. A moving average window (blue rectangle) is selected in order to derive the periodic moving average signal (blue line). A proper choice of the moving average window can be a multiplication of an integer number to the wave encounter period T_E in each wave length. Based on the the preliminary investigations and in order to keep the computational costs low, here, it is decided to define the moving average window as $2 \times T_E$ for each respective wave length.

Thereafter, a time window is selected on the signal tail and shown with a black rectangle. The original signal consists a dashed line part starting arbitrarily at some instances of time and a solid line part starting from the start time of the selected time window and ending at the end of the signal which is also the end of the selected time window.

A regular head wave simulation is deemed converged when the Standard Deviation (STD) of the periodic moving average signal (blue line) for the defined moving average window (blue rectangle) is below 2% of its Root Mean Square (RMS) over a selected time window (black rectangle). In the plot legend, the Standard Deviation in terms of percentage of Root Mean Square (STD%RMS) calculated on the periodic moving average signal (blue line) on the selected time window is shown. Based on the defined criterion, if the STD%RMS is smaller than 2, then the simulation deemed converged, however, the post-processing of the original signal is then carried out for the selected time window on the original signal tail. The Fourier analysis performed on the ship responses similar

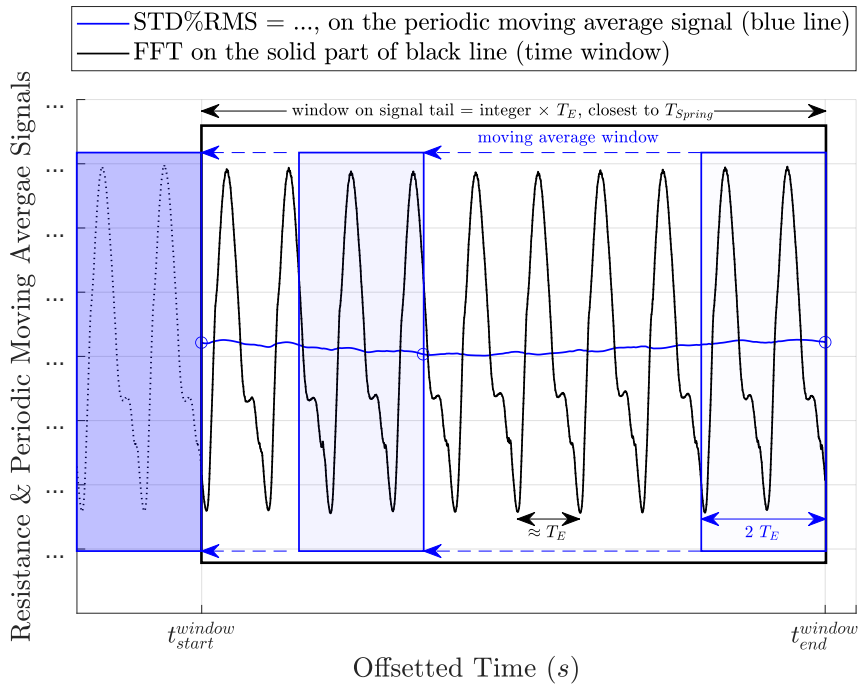

Figure 5.13: A representative resistance signal together with its periodic moving average signal plot for explaining the convergence criteria and post-processing techniques in regular head waves.

to the techniques explained in Section 4.3.7. Although a good choice of time window shall include several spring natural periods, this is not feasible due to the extremely large required computational costs. Therefore, for each wave length, the time window is selected in a way to have an integer number of T_E which is closest to spring natural period T_{Spring} in order to include partly the spring effects. The reason behind choosing an integer number of T_E is to minimize the spectral leakage in the Fourier analysis. Those integer numbers are given in Section 5.7. In the representative resistance plot shown in Figure 5.13, the spring effects can be observed in the periodic moving average signal (blue line).

Wake Analysis Methods

As discussed in Section 5.3, the SPIV measurements were carried out for carriage-fixed planes, however, it is more beneficial to study the ship nominal wake on the hull-fixed propeller plane. Therefore, although the wake validation is performed for the carriage-fixed planes similar to the SPIV measurements, the analysis of wake is carried out on the hull-fixed propeller disc.

The analysis of wake includes the investigations of three dimensional/non-dimensional

components of flow velocity (axial u or u/U and transversal v or v/U and w or w/U) on the propeller disc located at the propeller center and moving with the hull during the motion responses. The disk radius is equal to the propeller radius. Such velocity components are time-averaged $\bar{\cdot}$ and/or surface-averaged $\tilde{\cdot}$ in distinct ways in order to extract and present the main features of the flow.

Surface averaging of wake is carried out in two ways, one over the whole propeller disc surface area and the other for a number of equally distanced (in radial direction) circumferential surface areas derived from the propeller disc. Such circumferential surface areas are derived from the division of propeller disk (excluding the hub) into 10 circumferential stripes with the first strip starting at the hub edge to a radius of $R_{Hub} + (R_{Propeller} - R_{Hub})/10$ with an assumed center of $r_1 = R_{Hub} + (R_{Propeller} - R_{Hub})/20$, See Figure 5.14. The remaining 9 circumferential stripes are considered in the same way of radial stepping where the outer part of the tenth surface is the propeller tip radius $R_{Propeller}$. The averaged wake on these surface areas are called "circumferentially averaged wake", henceforth.

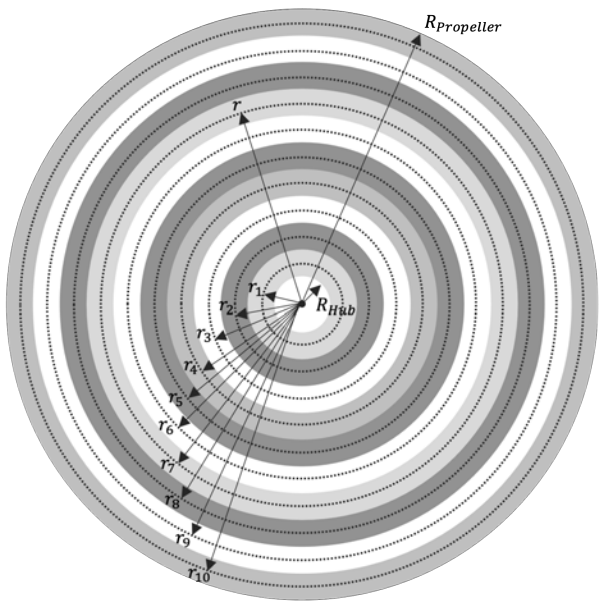

Figure 5.14: Circumferential stripes defined on propeller disc for wake analysis.

On the other hand, time averaging of wake over an specific time period of response can be carried out for each point on the propeller disc surface area to be able to present it as a contour plot, or for the surface averaged wake $\tilde{u}$ over the whole propeller disc during such time period to be able to derive wake fraction $W = 1 - \bar{\tilde{u}}/U$. Moreover, the time averaging can be performed on the circumferentially averaged wake during such time period at different radii to be presented as a line plot. The time period for time averaging wake in the regular wave simulations is mainly considered as an integer times T_E in each wave length.

5.5 Wave Propagation Results

The wave propagation simulations are carried out only for $\lambda/L = 0.6$ as the steepest and hence most critical wave length for numerical propagation. The numerical wave elevation ζ and its error (relative to the analytical representation of the 5th order Stokes wave) after 30 encountered waves are presented for GS1 (in SW-3D domain) in Figure 5.15a. Moreover, the longitudinally averaged absolute error (in percentage of the wave height) for Laminar and Turbulent flow ($k-\omega$ SST) simulations are presented in Figure 5.15b. The results of the turbulent flow simulations are similar to that of laminar flow. Wave propagation is a laminar phenomenon by its nature, while turbulent simulations are required when the hull performance is being studied. Therefore, only turbulent flow simulations are investigated henceforth.

The averaged absolute error is rather low for both laminar and turbulent flow simulations in GS1. Moreover, the error converges approximately after a few encountered wave periods. Therefore, the simulations deemed converged after 12 encountered waves and the Fourier analysis of the wave elevation at the probes are carried out for GS1-GS4 over the 12-20 encountered wave periods time window. However, for the hull performance simulations in GS5, the time window in which the post-processing of the signals carried out is placed much later than the initial 12 encountered waves, hence no significant error development is expected in terms of wave propagation. It is assumed the error is reached to a rather stable state.

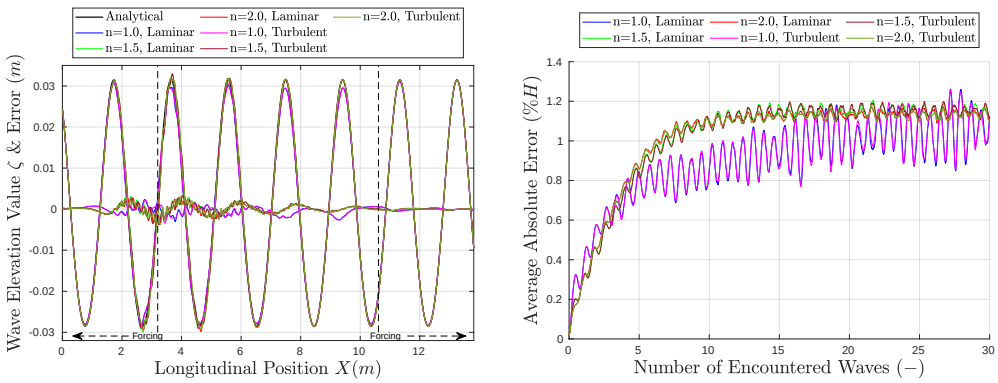

(a) Wave elevation after 30 T_E.

(b) Monitored averaged absolute error.

Figure 5.15: Wave elevation near symmetry plane (Y_1) and its error with respect to the analytical wave elevation for GS1 in SW-3D domain for $\lambda/L = 0.6$.

The 1st harmonic of the wave amplitude, as a dominant component, is shown in Figure 5.16. It should be noted that the magnitudes of the higher harmonic components are very small, thereby small differences yield large errors.

It can be clearly seen that for all the grid sets and all the probes, the magnitude of the error for $n = 0.50$ is considerably larger than the finer grids. For X_1 probes (located

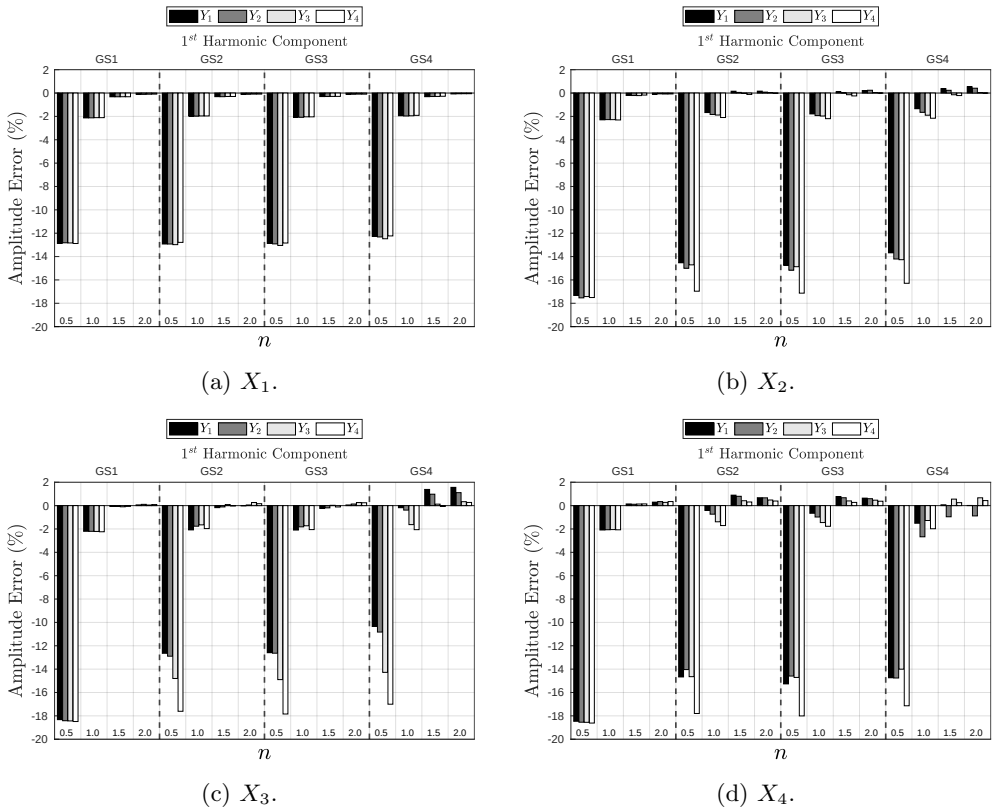

(a) X_1. (b) X_2.

(c) X_3. (d) X_4.

Figure 5.16: The Fourier analysis results of the wave elevation at the probes for turbulent flow simulations in SW-3D. The probes locations can be seen in Figure 5.11.

at the end of forcing zone), shown in Figure 5.16a, the magnitudes of errors decrease from coarsest to finer grids in all grid sets. Moreover, the results for different grid sets and an specific refinement level are very similar, hence no significant effects from the local refinements and overset region at that longitudinal location are observed. The results are also similar for different Y probes in each refinement level.

For X_2 probes (before the overset region), shown in Figure 5.16b, the magnitude of error for GS1 decreases from coarser grids towards finer grids, while for GS2, GS3 and GS4 the behavior varies depending on the grid refinement and the probes Y location. On the other hand, the magnitude of the error is relatively smaller for $n = 1.50, 2.00$ compared to the coarser grids. Interestingly, for GS4 in all refinement levels for Y_1 and Y_2 (located closer to the pitching overset region) the change of error is towards positive values which results in decreased error in $n = 0.50, 1.00$ and increased error in $n = 1.50, 2.00$ (although negligible).

For X_3 probes (only Y_1 and Y_2 are located within the overlapping zone for the grid sets including overlapping refinement), shown in Figure 5.16c, almost similar trend as of

X_2 probes is seen, however, with a more pronounced change of errors in Y_1 and Y_2 for GS4. This may imply that the overset interpolations are affected more significantly in the case of the existing pitch motion than the restrained overset region in GS3. For probes located at X_4 (only Y_1 and Y_2 are located inside the overset region after the overlapping zone), shown in Figure 5.16d, the change of error between different refinement levels is towards positive values in all grid sets with more pronounced effects on Y_1 and Y_2 probes.

In general, larger errors are seen in each grid set and for X probes further away from the inlet (X_1 to X_4). To a large extent, GS2 and GS3 in all X probes are similar in each refinement level showing better interpolations between the overset and the background regions for the restrained overset. The errors in Y_3 (and respectively Y_4) in GS4, GS3 and to some extent also GS2 for each specific X probe are almost similar, which imply that the results are affected less from the refinements related to the overset region. The errors of $n = 2.00, 1.50$, and to some extent $n = 1.00$, in X_4 and GS1 in all Y probes are larger than those of X_3, possibly because the error moves towards positive values from X_1 to X_3, hence in X_3 the error magnitude becomes smaller and then for X_4 the errors are become positive. On the other hand, for $n = 0.50$ the error increases in negative values. It should be mentioned that no significant wave encounter period change is seen in the wave propagation simulations and it remains below 0.2% of the wave encounter period.

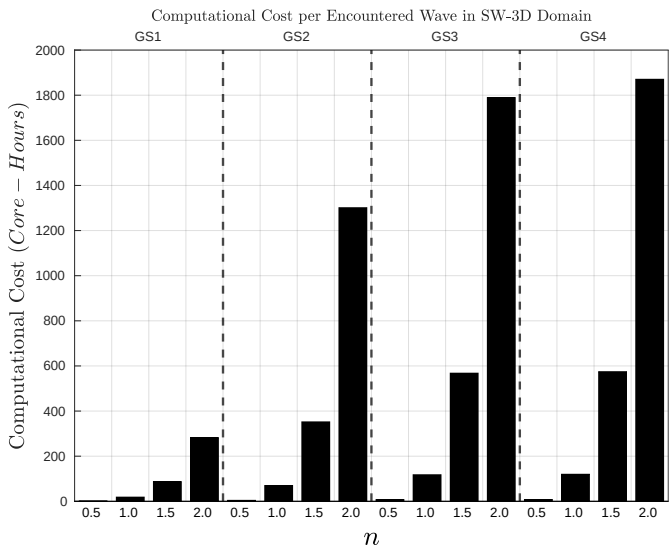

Figure 5.17: Computational costs per encountered wave period of simulation.

The most important conclusions from the wave propagation study are summarized here. Firstly, the grid $n = 0.50$ is not capable of modeling the propagation of the considered wave due to the very large discrepancies with respect to the analytical wave. Secondly, the error in wave amplitude (time-averaged deviation from the analytical wave amplitude) for grids $n = 1.00$, 2.50 and 2.00 is mostly lower than 3%. Therefore, the results of

grid $n = 0.50$ in hull performance simulations are not included in the verification and validation studies further in the thesis. The computational costs per each encountered wave period in terms of $Core - Hours$ are provided in Figure 5.17. The computational costs are significantly higher for the finer grids in each grid set.

5.6 Calm Water Results V&V

In this section, the calm water results are provided including an extensive verification and validation analysis of the ship hydrodynamic responses and its wake. The analysis of results with respect to the hydrodynamic performance of the ship are provided in Chapter 5.8.

The calm water simulations are carried out in both fixed and free surge (2DOF and 3DOF) conditions in all of the considered grids, i.e., $n = 0.50$, 0.75, 1.00, 1.25, 1.50 and 2.00. However, the results of the coarsest grid $n = 0.50$ are drastically off in comparison to the other grids. Therefore, the results from this grid are just given in the manuscript and not included in the plots and the verification studies. Below, different hydrodynamic responses of the ship and its wake are investigated. First, the convergence of simulations are discussed and then the verification and validation of results are carried out.

5.6.1 Responses

The calm water resistance in free and fixed surge conditions are shown in Figure 5.18. There is a factor of 2 multiplied to the resistance results from the simulations with symmetry boundary conditions in order to represent the full hull results. The convergence criterion for calm water simulations is explained in Section 5.4.6. The selected time window for calm water simulations is $6 \times 2\ s = 12\ s$. The convergence is confirmed in all of grids in both fixed and free surge conditions.

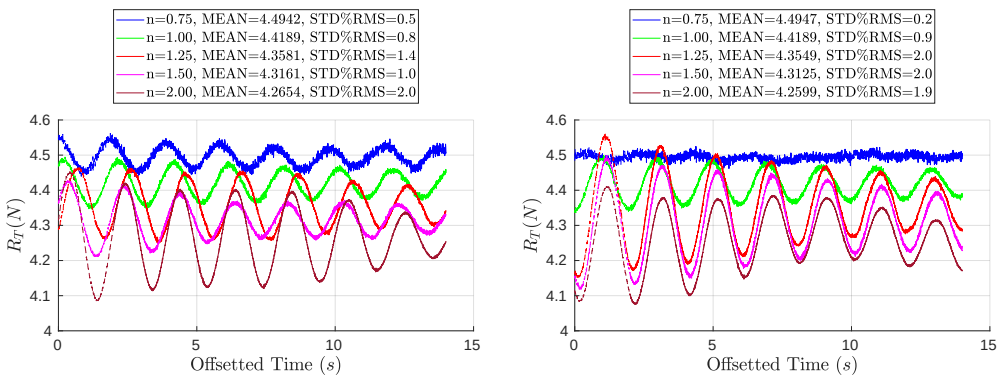

(a) Fixed surge.

(b) Free surge.

Figure 5.18: Resistance results in fixed and free surge calm water simulations.

The presented MEAN values in Figure 5.18 are the computed total resistance from each grid. Some marginal effects from the spring on the resistance signal can be observed in the free surge condition, however, the MEAN resistance value is rather similar in fixed and free surge conditions for the chosen time window. The computed resistance in grid $n = 0.50$ is about 3.74 N in both free and fixed conditions. As mentioned earlier, this grid is too coarse and cannot capture the flow physics correctly and thus excluded in the following analyses. The verification analysis is then only carried out for the free surge condition and it is shown in Figure 5.19a. The asymptotic resistance obtained from the convergence study is predicted to be almost 4 N and the uncertainty of the finest grid is about 8.8%.

The computed resistance values in all grids are relatively similar which are also close to the EFD data. On the other hand, the fitted line using the Least Square method is very sensitive to the small changes of magnitude. In order to show such sensitivities, the resistance value for the finest grid $n = 2.00$ is manipulated (increased by 0.02 N) and the verification is repeated, see the results in Figure 5.19b. The uncertainty of the finest grid is now reduced from 8.8% to 3.4% with the final asymptotic value around 4.2 N and a relatively linear fitted line. This may encourage a linear line fitting for the situations in which the data points are relatively close in magnitude.

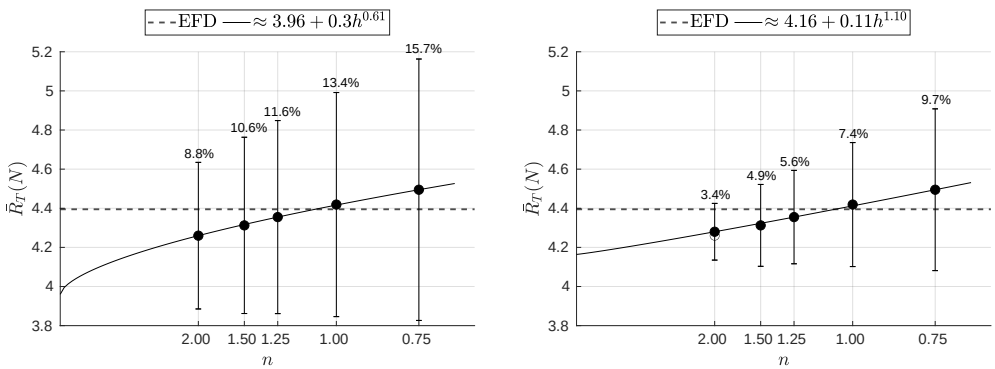

(a) Original verification.

(b) Manipulated verification.

Figure 5.19: V&V for the original and manipulated data points on free surge calm water simulations.

The computed surge in all grids for the calm water simulations in free surge conditions is very close to zero (-0.0008 to 0.0016 m). It should be noticed that the fixed and free surge should not change the steady state values of responses in calm water, but their transient values. Therefore, the surge value depends mainly on the external force F_0 and the spring stiffness. Considering zero surge acceleration $\ddot{x} \approx 0$ in calm water, then the resistance can be estimated as $R_T \approx F_0 - Kx$. The external force from EFD data is not available, but since the surge motion is given as $x_{EFD} = -0.01242$ m, then the estimated experimental $F_0 \approx 3.17$ N. In the simulations, the constant external force of $F_0/2 = 2.206$ N is considered (/2 is for symmetry boundary condition).

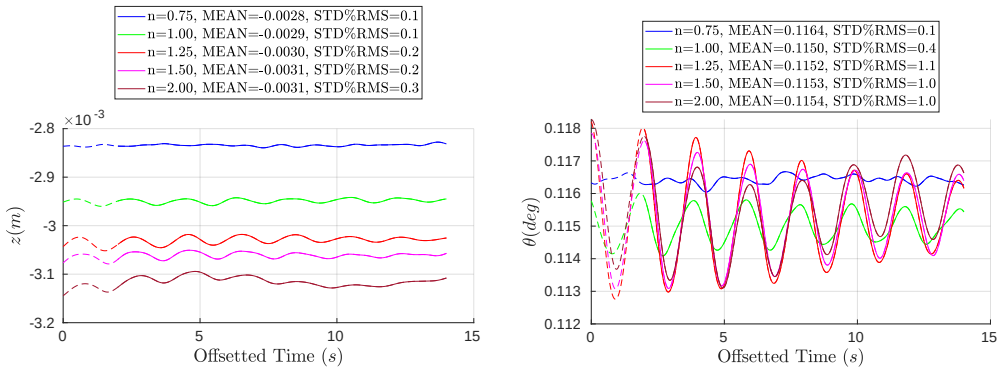

(a) Heave. (b) Pitch.

Figure 5.20: Computed heave and pitch in free surge calm water simulations.

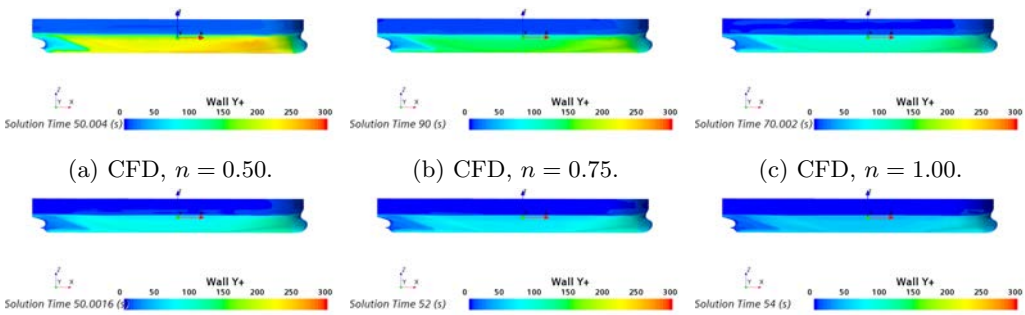

(a) CFD, $n = 0.50$. (b) CFD, $n = 0.75$. (c) CFD, $n = 1.00$.

(d) CFD, $n = 1.25$. (e) CFD, $n = 1.50$. (f) CFD, $n = 2.00$.

Figure 5.21: Wall y^+ in each grid at the last time step in free surge calm water simulations.

The computed heave and pitch responses in calm water (sinkage and trim but at COG) are shown in Figure 5.20. The same time window is considered as of resistance response. The computed values are rather similar considering the very small differences in terms of magnitude (up to ≈ 0.0003 m and 0.001 deg). Therefore, the grid convergence study is not carried out for heave and pitch responses. The computed heave and pitch (in both free and fixed conditions) in grid $n = 0.50$ are about -0.0084 m and 0.150 deg, respectively, which are quite different from the computed values in the other grids. The experimental value of heave and pitch in calm water are $z_{EFD} = -0.00317$ m and $\theta_{EFD} = 0.129$ deg, hence very small errors in terms of magnitude are seen in all grids with respect to the experimental values.

The wall y^+ in each grid at the last time step in free surge calm water simulations are shown in Figure 5.21. The surface averaged $\tilde{y}^+$ values on the wetted surface area of the hull are approximately 202, 133, 99, 78, 65 and 48 for the coarsest grid to the finest one. The wetted surface area of the hull S is about 2.78 m^2 from all the grids.

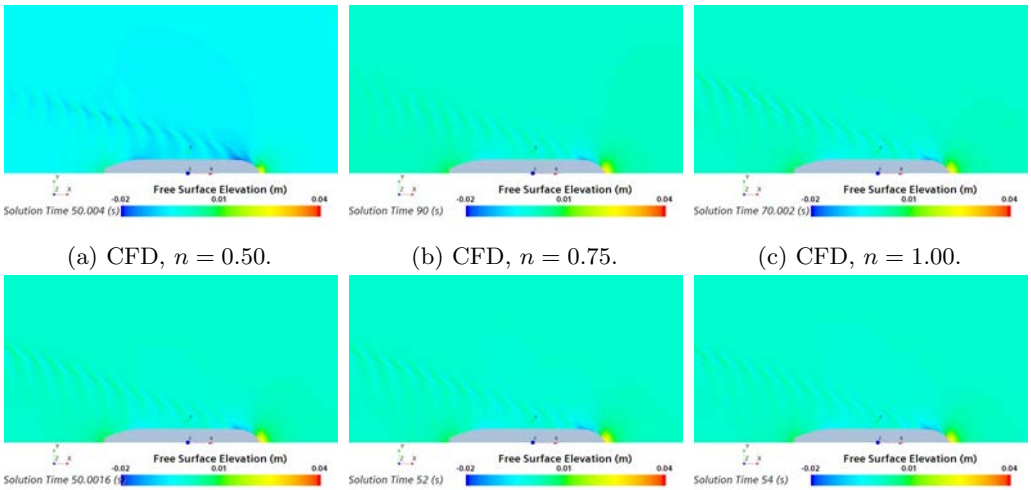

(a) CFD, $n = 0.50$. (b) CFD, $n = 0.75$. (c) CFD, $n = 1.00$.

(d) CFD, $n = 1.25$. (e) CFD, $n = 1.50$. (f) CFD, $n = 2.00$.

Figure 5.22: Free surface elevation in each grid at the last time step in free surge calm water simulations.

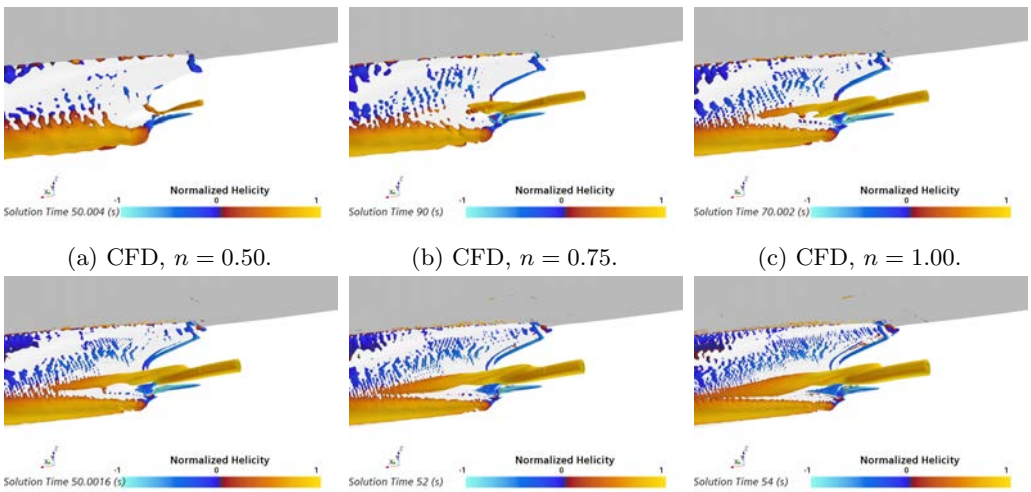

(a) CFD, $n = 0.50$. (b) CFD, $n = 0.75$. (c) CFD, $n = 1.00$.

(d) CFD, $n = 1.25$. (e) CFD, $n = 1.50$. (f) CFD, $n = 2.00$.

Figure 5.23: The bilge vortex (colored by normalized helicity) found by Q-criterion = 10 $/s^2$ in each grid at the last time step in free surge calm water simulations.

Free surface elevation is shown in Figure 5.22. The zero surface elevation is missed in grid $n = 0.50$ due to its very course grid distribution near the free surface. On the other hand, the Kelvin wedge is well captured in the finer grids with the highest quality in the finest grid $n = 2.00$. The bilge vortex found by the same Q-criterion in different

grids is shown in Fig. 5.23. A smaller vortex is also generated under the hub cap region that swirls opposite to the bilge vortices (shown by the normalized helicity). The vortical structures are obviously captured with a higher resolution in finer grids. The position where the bilge vortices hit the propeller disk in calm water is more and less stationary.

5.6.2 Wake

The free surge calm water surface-averaged nominal wake computed on the hull-fixed propeller disc for different grids as well as the grid convergence study performed on the axial velocity component are shown in Figure 5.24.

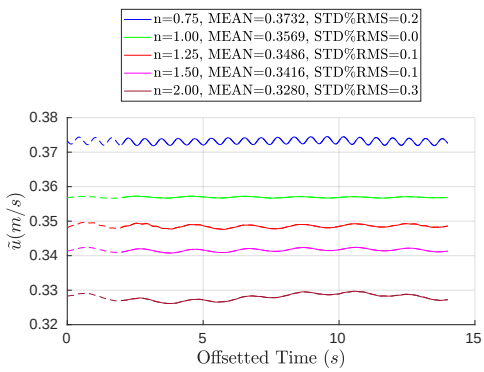

(a) Axial component.

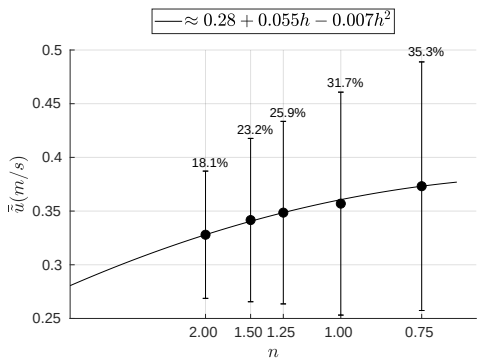

(b) Verification of axial component.

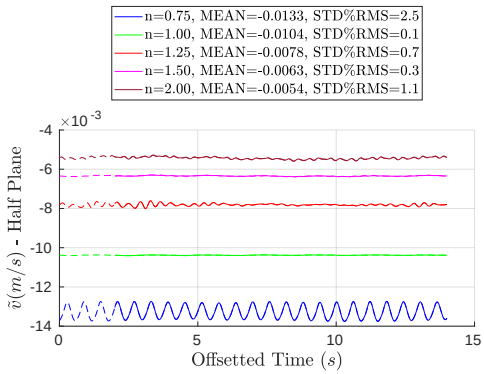

(c) Tangential Y component.

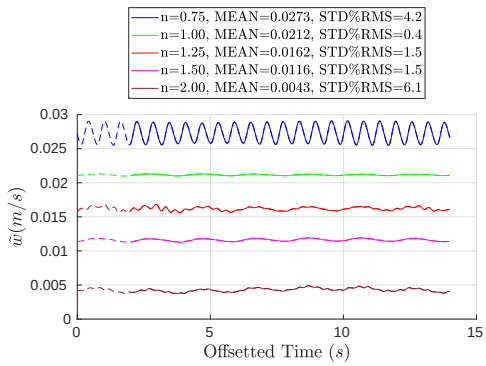

(d) Tangential Z component.

Figure 5.24: Surface-averaged velocity components on hull-fixed propeller disc and verification of axial velocity component in the free surge calm water simulations.

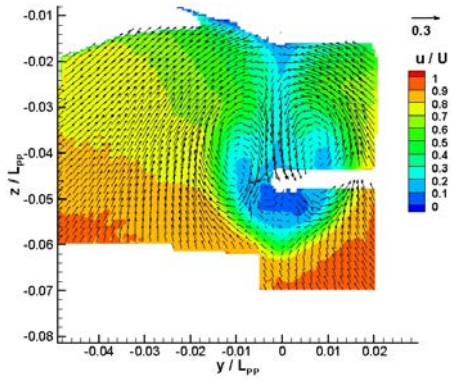

Figure 5.25: EFD wake (SPIV) in carriage-fixed plane at the initial position of propeller plane in free surge calm water experiments.

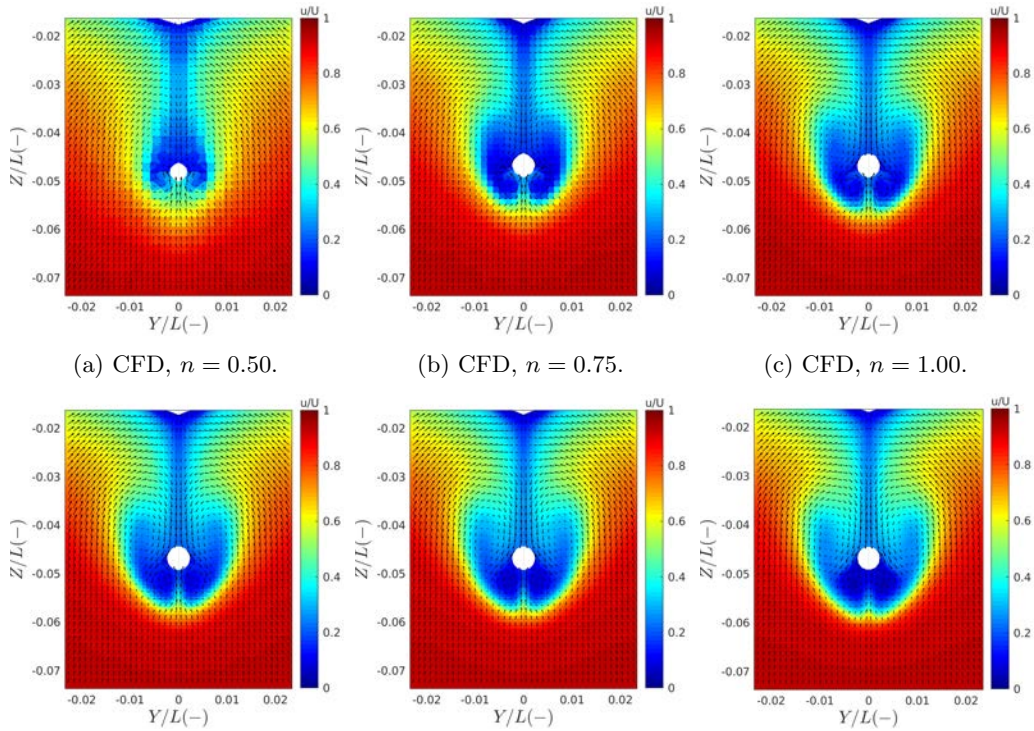

(a) CFD, $n = 0.50$. (b) CFD, $n = 0.75$. (c) CFD, $n = 1.00$.

(d) CFD, $n = 1.25$. (e) CFD, $n = 1.50$. (f) CFD, $n = 2.00$.

Figure 5.26: CFD wake (at the last time step) in carriage-fixed plane at the initial position of propeller plane in free surge calm water simulations.

The fixed surge wake is very similar to the free surge wake, thus fixed surge wake is not provided. Although the surface-averaged velocity components exhibit oscillatory behavior in time, the magnitude of the oscillations are insignificant, therefore, only the computed wake in the last time step of simulations in calm water is analyzed. The MEAN (time-averaged) values are given in the plot legend for each grid. The MEAN value for the axial component for grid $n = 0.50$ is about 0.43. The MEAN values of the axial velocity shows a monotonic convergence as the refinement level increases. The numerical uncertainly of the axial wake varies between 35% and 18% from the coarsest to the finest grid. This indicates the significance of grid refinement level on the predicted wake in calm water.

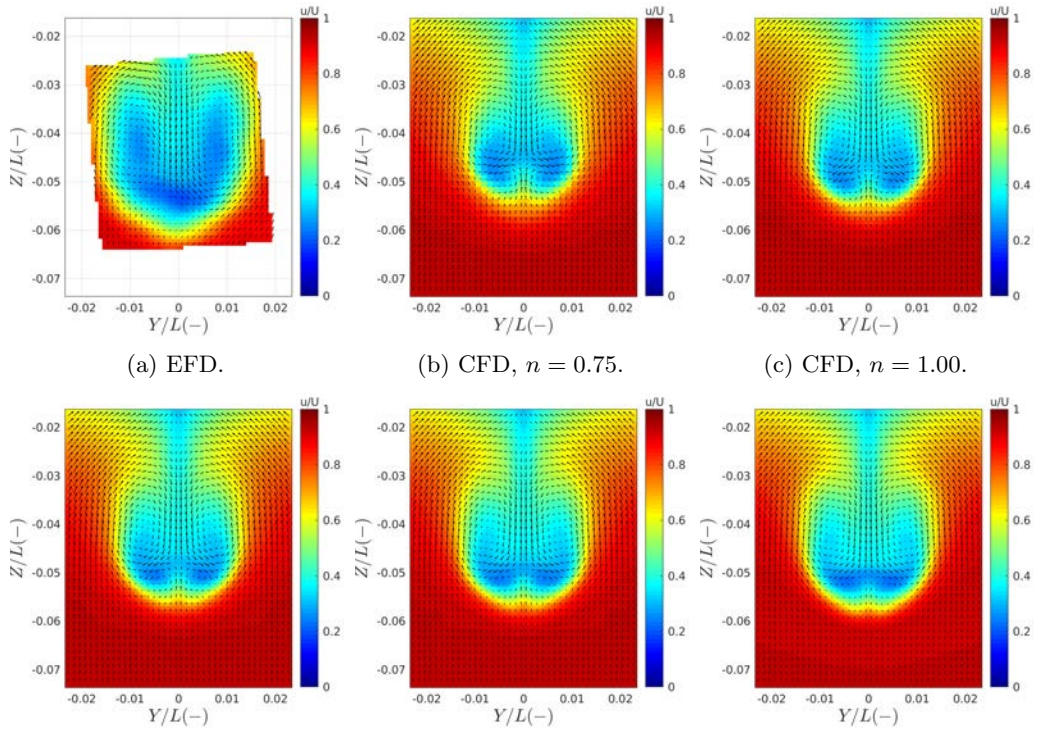

(a) EFD. (b) CFD, $n = 0.75$. (c) CFD, $n = 1.00$.

(d) CFD, $n = 1.25$. (e) CFD, $n = 1.50$. (f) CFD, $n = 2.00$.

Figure 5.27: EFD and CFD (at the last time step) wake in carriage-fixed plane at the aft perpendicular in fixed surge calm water condition.

The SPIV measurements and hence the wake validation were carried out in carriage-fixed planes. The SPIV measurements of calm water wake were carried out in EFD_1 at a plane located at the initial position of propeller on the carriage in free surge condition (where the raw data is not provided and only a screenshot is available) and in EFD_2 at aft perpendicular (AP) in fixed surge condition. In Section 5.3 a detailed explanation of SPIV measurements is provided.

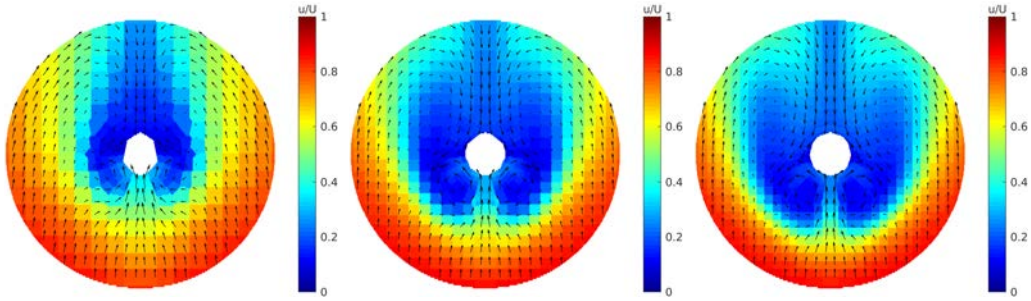

(a) CFD, $n = 0.50$. (b) CFD, $n = 0.75$. (c) CFD, $n = 1.00$.

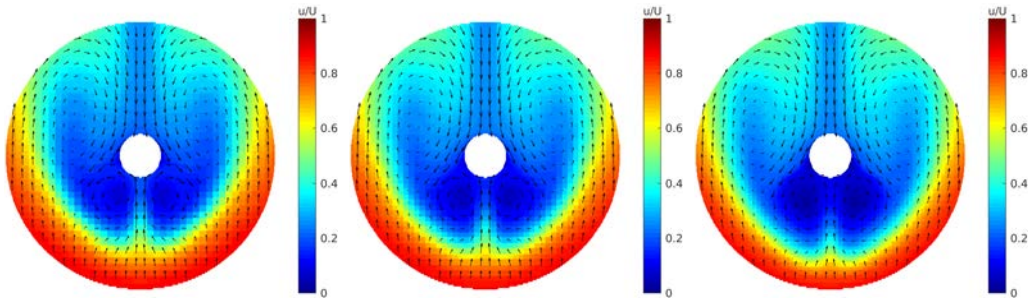

(d) CFD, $n = 1.25$. (e) CFD, $n = 1.50$. (f) CFD, $n = 2.00$.

Figure 5.28: CFD wake on hull-fixed propeller disc at the last time step in free surge calm water simulations.

The free surge calm water experimental wake at propeller plane (PP) is shown in Figure 5.25. The computed wake in the same condition with different grids are given in Figure 5.26. The plot axes Y/L and Z/L are defined in the carriage-fixed coordinate system at initial position of propeller plane with origin located at initial free surface position, see Figure 5.6. The non-dimensional axial velocity u/U is represented by contour plots and the non-dimensional transversal component of wake (tangential to the plane of study) are represented by vectors.

Since the color map of the EFD and CFD contour plots shown in Figure 5.25 are different (no raw data available for the EFD data), a one-to-one comparison between the calm water EFD and CFD plots cannot be done. Moreover, validation of wake in this case involves an important potential source of discrepancy. The external force F_0, and hence the amount of spring stretch/compress, i.e., surge motion of the ship, were different between EFD and CFD, therefore, the longitudinal location of the shown contour plots might be different. However, the main flow features are still comparable. The coarsest grid $n = 0.50$ is incapable of capturing the main wake features. It is obvious that the flow details and the hook shape bilge vortex are captured much better in the finer grids.

The fixed surge hull's calm water wake comparison at the aft perpendicular plane is shown in Figure 5.27. The results of the coarsest grid are eliminated. The hook shape bilge vortex seen in EFD wake is mostly missing in CFD computations in all grids except

in the finest grid $n = 2.00$. The comparison of calm water wake from CFD and this EFD data set can only be carried out qualitatively, considering the probable sources of discrepancy.

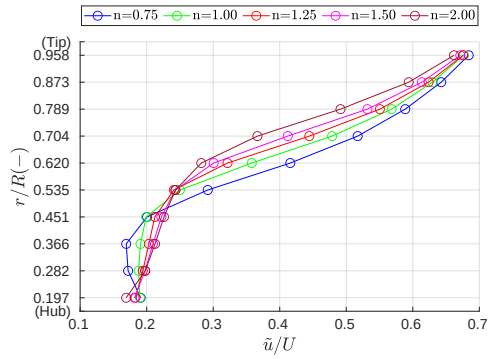

Figure 5.29: Circumferentially averaged CFD wake axial component on hull-fixed propeller disc at the last time step in free surge calm water simulations.

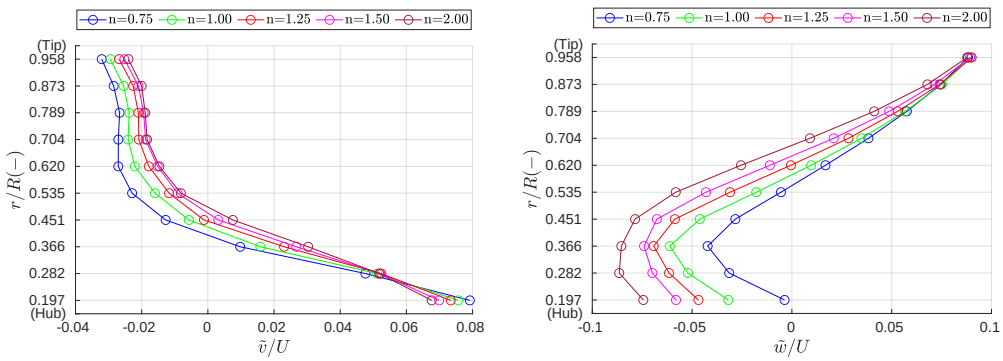

(a) Tangential Y component.

(b) Tangential Z component.

Figure 5.30: Circumferentially averaged CFD wake tangential components on hull-fixed propeller disc at the last time step in free surge calm water simulations.

The nominal wake on the propeller disc obtained from different grids are shown in Figure 5.28. Since the surge, heave and pitch responses in free surge calm water simulations are very small, the wake on the hull-fixed propeller disc is very similar to that of carriage-fixed wake at initial position of propeller plane in the same condition. The captured bilge vortex is stronger in the finer grids and the extent of the vortical structures under the hub and particularly the size of the low axial velocity region are larger for the finer grids.

Propeller designers often use a Circumferentially averaged wake for designing the

particulars of a wake adapted propeller. Such a wake, represents an averaged flow encountered by propeller blade at each radii in one revolution. Figures 5.29 and 5.30 show the computed circumferentially averaged wake obtained from different grids. A rather significant change in the magnitude and profile of the wake components is observed between different grids. In case a propeller is supposed to be designed based on computed wake from CFD, the resultant wake adapted design will be very different depending on the employed wake.

5.7 Regular Wave Results V&V

In this section, the regular head wave results are provided including an extensive verification and validation analysis of the ship hydrodynamic responses and its wake. The analysis of results with respect to the hydrodynamic performance of the ship are provided in Section 5.8.

The CFD simulations in regular head waves are carried out solely in free surge (3DOF) condition. The simulations are carried out for all grids, i.e., $n = 0.50$, 0.75, 1.00, 1.25, 1.50 and 2.00, in wave lengths $\lambda/L = 0.6$ and 1.1, however, only the grid $n = 1.00$ is considered for the hull performance simulations in the longest wave $\lambda/L = 1.6$, without carrying out a grid dependence study in this wave length. The results of the coarsest grid $n = 0.50$ are drastically off in comparison to the other grids. Therefore, the results from this grid are just given in the manuscript and not included in the plots and the grid convergence studies.

In the studies carried out in Chapter 4, both the dimensional and non-dimensional responses are validated and analyzed. It is found that the effects of actual incident wave on the resistance and motion responses of the ship are significant. When the effects of actual measured wave height in model tests are taken into account, the validation errors for the non-dimensional responses considerably decrease in comparison to the dimensional ones. This is mainly a result of difference between the actual incident wave during the tests and the intended wave, caused by the wave generator in the towing tank. In the current investigations for KVLCC2, only the dimensional analyses are performed, except for the analysis of wake velocities, in which the non-dimensionalization is based on the ship velocity U, and hence regardless of the actual wave height. Therefore, for the current dimensional analyses, the potential effects from the actual incident wave height should not be overlooked.

In this section, different hydrodynamic responses of the ship and its wake are investigated. First, the convergence of simulations are discussed and then the verification and validation of results are carried out. The results are provided separately for each wave length.

5.7.1 Responses

$\boldsymbol{\lambda/L = 0.6}$

The resistance results in regular head wave $\lambda/L = 0.6$ is shown in Figure 5.31. The convergence criterion for regular head wave simulations is explained in Section 5.4.6. The

selected time window for $\lambda/L = 0.6$ is $15 \times T_E \approx 11.39\ s$ which is close to the spring natural period $T_{Spring} \approx 11.25$. The STD%RMS value for the periodic moving average with a moving window of $2T_E$ for all grids confirms the convergence based on the defined criterion. The MEAN values are calculated on a $15T_E$ time window. Fourier analysis of time series is also performed on the same time window.

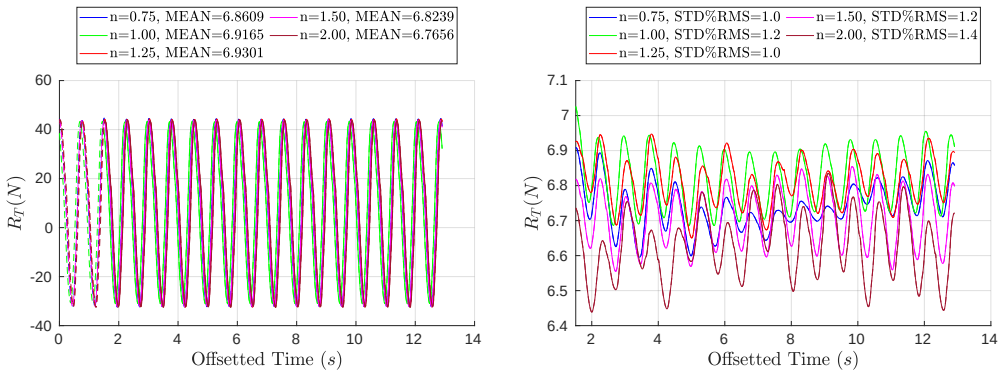

(a) Resistance time series.

(b) Resistance periodic moving average.

Figure 5.31: Resistance time series (a) and its periodic moving average (on a $2T_E$ moving window) (b) in $\lambda/L = 0.6$. The MEAN values are derived from a $15T_E$ time window.

The Fast Fourier Transform (FFT) results as well as the grid convergence study of the 0th, 1st and 2nd harmonic amplitudes (HAs) of resistance are shown in Figure 5.32. Higher harmonics are relatively smaller than the aforementioned components, hence they are not included in the grid convergence studied. The Fourier analysis in Figure 5.32a shows that the ship resistance response is a harmonic function of the encounter wave frequency, as the dominating FFT amplitudes are seen at the integer harmonic phase components (i.e., the ratio of FFT frequencies to the wave encounter frequency). The 0th harmonic amplitudes of resistance are identical to the absolute of MEAN values $\bar{R}_T$ given in the legend of Figure 5.31a. The MEAN value for the grid $n = 0.50$ is 6.25 N which is lower than the values seen in other grids. The added resistance due to waves can be calculated by subtracting the MEAN value of calm water resistance from the MEAN value of total resistance in waves, however, in the current investigations the MEAN value of total resistance is under study not the added resistance due to waves. The verification and validation of $\bar{R}_T$ is shown in Figure 5.32b.

In the experiments, the hydrodynamic force excluding the inertial force was recorded by a dynamometer, as explained in Section 5.3, and the mean of measured force (i.e., 6.85 N in EFD_1 and 6.847 N in EFD_2) is presented as the total resistance in waves. The MEAN of total resistance in CFD simulations in $\lambda/L = 0.6$ in all grids is rather similar and close to the the EFD data, however, the predicted asymptotic value through a second order Richardson extrapolation is much lower. A linear line fitting may be a better candidate for this condition, similar to what is seen in calm water resistance grid convergence study.

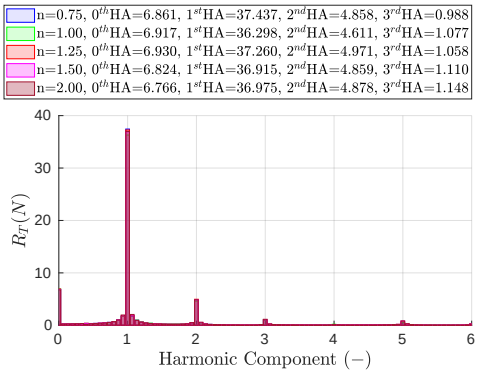

(a) FFT results.

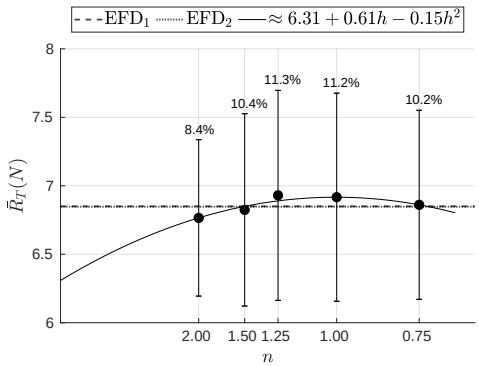

(b) V&V for the 0th HA of R_T.

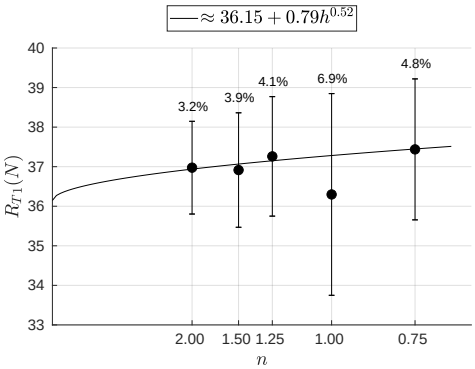

(c) Verification of the 1st HA of R_T.

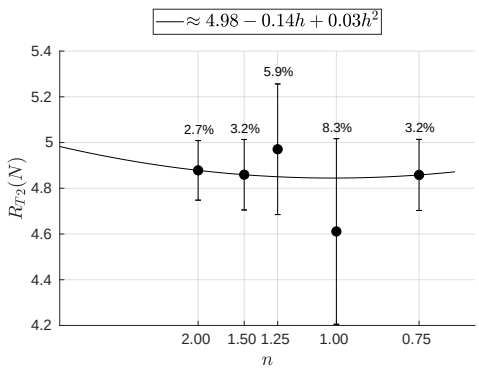

(d) Verification of the 2nd HA of R_T.

Figure 5.32: Fourier analysis results and grid convergence study on the total resistance harmonic amplitudes in $\lambda/L = 0.6$.

Moreover, the grid convergence study is carried out for the 1st and 2nd harmonic amplitudes (R_{T1} and R_{T2}) as the dominating components in the ship resistance response. The numerical uncertainties for these quantities are lower than the ones seen for $\bar{R}_T$.

Since the 1st harmonic amplitude of motions is the dominating component in the Fourier analysis of motion responses, there is no significant gain of providing the motions time series or their FFT bar graphs. Therefore, the verification and validation of motion responses is carried out only for the 1st harmonic amplitudes of the responses. Moreover, since the surge motion response of the ship in regular head waves consists a frequency close to the spring natural frequency in conjunction with the wave encounter frequency, the surge motion time series are provided which will be helpful to understand the instantaneous location of the carriage-fixed planes at the time of wake computations later on.

The time history of the surge motion and the results of uncertainty analysis of the 1st harmonic amplitude of motion responses are shown in Figure 5.33. Despite the marginal

magnitude of the 1st harmonic amplitude of the motion, the numerical uncertainties for all the grids are relatively small, and comparable to the numerical uncertainties of the 1st and the 2st harmonic amplitudes of the total resistance. The 1st harmonic amplitude of surge, heave and pitch motions for the coarsest grid $n = 0.5$ are 0.0014 m, 0.0017 m and 0.100 deg, respectively, which are rather off from the other grids.

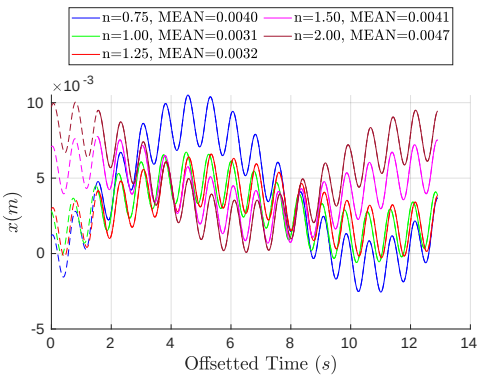

(a) Surge motion time series.

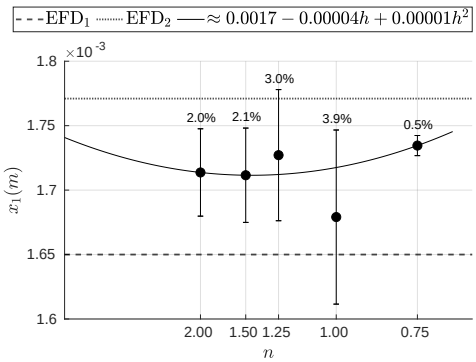

(b) V&V for the 1st HA of surge x_1.

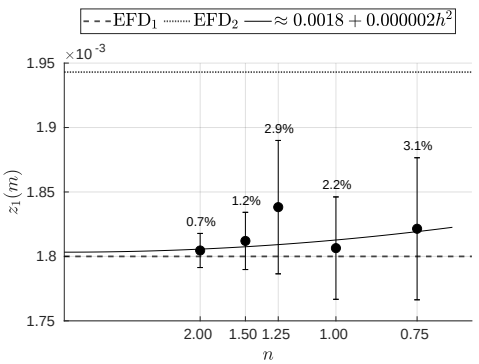

(c) V&V for the 1st HA of heave z_1.

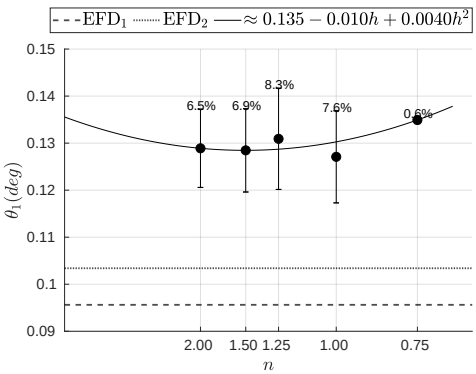

(d) V&V for the 1st HA of pitch θ_1.

Figure 5.33: V&V on the motion responses 1st harmonic amplitudes in regular head wave $\lambda/L = 0.6$.

Through the FFT analyses it is found that the surge motion amplitude at the natural frequency of spring in the experimental model tests EFD_1 was 0.0054 m. The equivalent response amplitude at the natural frequency of spring in the CFD computations for grids $n = 0.75$ to $n = 2.00$ are 0.0049, 0.0020, 0.0017, 0.0018 and 0.0030 m, respectively. The differences in terms of magnitude are insignificant.

The experimental mean heave from EFD_1 and EFD_2 were -0.00314 and -0.00322 m, respectively. The MEAN value of heave for the grids $n = 0.5$ to $n = 2.00$ are -0.01010,

-0.00178, -0.00374, -0.00333, -0.00325 and -0.00327 m, which are close to the calm water heave (sinkage at COG given in 5.20a) for most of the grids except for the coarsest ones. Moreover, the computed mean values of heave are close to the EFD data.

The experimental mean pitch from EFD_1 and EFD_2 were 0.1240 and -0.125 deg, respectively. A negative mean pitch is measured in EFD_2 contrary to EFD_1. The MEAN value of pitch for the grids $n = 0.5$ to $n = 2.00$ are 0.1313, 0.1065, 0.1054, 0.1051, 0.1049 and 0.1052 deg, which are close to the calm water pitch (trim at COG given in 5.20b) as well as EFD_1 data considering the very small magnitudes in deg.

The measured wave height in EFD_1 was about 0.078 m which is larger than target wave height $H = 0.06$ m. On the other hand, the measured wave height in EFD_2 was 0.053 m which is rather close to the target wave height. The deviation of wave height in EFD_1 from the target value may influence the ship responses. Although the wave height was larger than H in EFD_1 and smaller in EFD_2, the measured resistance is very similar between these data sets, as shown in Figure 5.32b. The uncertainty of the experimental measurements should not be forgotten, however, no further information is available from the model tests, which makes is hard to carry out a more in depth comparison.

The MEAN (time-averaged over $15T_E$ time window) of surface averaged $\bar{y}^+$ over the wetted surface area of the ship (i.e., $\bar{\bar{y}}^+$) for the grids $n = 0.50$ to $n = 2.00$ are approximately 210, 136, 101, 80, 66 and 49, which are close to the calm water values in each respective grid. The MEAN of wetted surface area in all grids are approximately 2.79 m^2, which is close to the calm water value (2.78 m^2).

$\boldsymbol{\lambda/L = 1.1}$

The resistance results in regular head wave $\lambda/L = 1.1$ is shown in Figure 5.34. The selected time window for $\lambda/L = 1.1$ is $10 \times T_E \approx 11.20$ s which is close to the spring natural period $T_{Spring} \approx 11.25$. The STD%RMS value for the periodic moving average with a moving window of $2T_E$ for all grids confirms the convergence based on the defined criterion. The MEAN values are calculated on a $10T_E$ time window. Fourier analysis of time series is also performed on the same time window.

The FFT results as well as the grid convergence study of the 0th, 1st and 2nd harmonic amplitudes of resistance are shown in Figure 5.35. Contrary to $\lambda/L = 0.6$, the higher harmonic amplitudes are not negligible in $\lambda/L = 1.1$, but similar to the shorter wave length, the verification study is only constrained to the 0th, 1st and 2nd harmonic amplitudes. However, the higher harmonic amplitudes are presented and discussed in Section 5.8. The 0th harmonic amplitudes of resistance are identical to the absolute of MEAN values $\bar{R}_T$ given in the legend of Figure 5.34a. The MEAN value for the grid $n = 0.50$ is 10.15 N which is significantly lower than the other grids. The verification and validation of $\bar{R}_T$ is shown in Figure 5.35b. The numerical uncertainties of the 0th harmonic amplitude of resistance for all the grids are below 10% which is smaller than the ones obtained from the simulations in the shorter wave length. The 0th amplitude of the measured resistance from EFD_1 is within the numerical uncertainty range of the computed values from all the grids.

The mean of measured force by dynamometer (i.e., representing $\bar{R}_T$ in model tests) was 10.39 N in EFD_1 and 10.18 N in EFD_2. The MEAN of total resistance in CFD

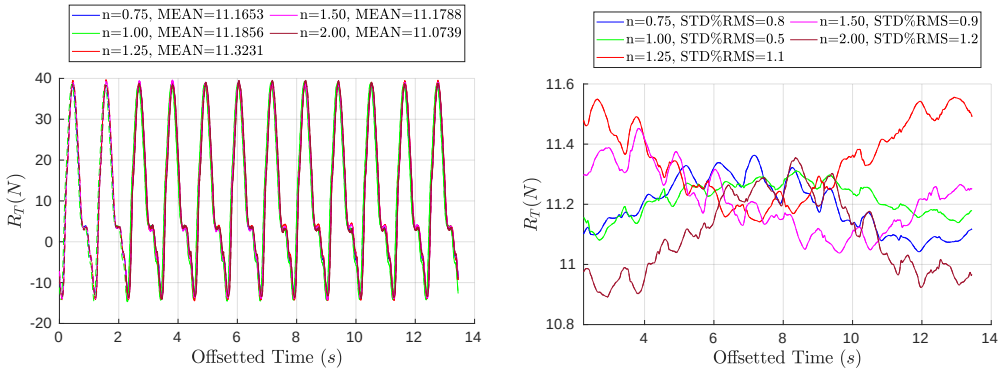

(a) Resistance time series.

(b) Resistance periodic moving average.

Figure 5.34: Resistance time series and its periodic moving average (on a $2T_E$ moving window) in $\lambda/L = 1.1$. The MEAN values are derived on a $10T_E$ time window.

simulations in $\lambda/L = 1.1$ in all grids is rather similar, but over-predicted by approximately $6 - 11\%$ compared to the EFD data. The measured wave height in EFD_1 and EFD_2 were about 0.056 and 0.059 m, respectively. Similar to the calm water resistance as well as the mean total resistance in $\lambda/L = 0.6$, a linear line fitting may be a better candidate for the grid convergence study in $\lambda/L = 1.1$, as the computed values are close in all grids. Moreover, the grid convergence study is carried out for the 1st and 2nd harmonic amplitudes (R_{T1} and R_{T2}) as the dominating components in the ship resistance response. The uncertainty of results seen for R_{T1} are lower than the ones seen for $\bar{R}_T$, while the values for R_{T2} are approximately close to $\bar{R}_T$.

The verification and validation of motion responses is carried out by only providing the 1st harmonic amplitudes, while the surge motion time series are also provided to understand the location of the carriage-fixed planes at the time of wake computations later on. The results are shown in Figure 5.36. The numerical uncertainties of the 1st harmonic amplitude of surge in $\lambda/L = 1.1$, are as large as 23% and the largest numerical uncertainties obtained so far. Contrarily, the numerical uncertainty of the 1st harmonic amplitudes of heave and pitch motions are considerably smaller (less than 7%) and in the same level as the corresponding values obtained from the shorter wave length simulations.

The 1st harmonic amplitude of surge, heave and pitch motions for grid $n = 0.5$ are 0.00218 m 0.02134 m and 1.66 deg, respectively, which are rather close to other grids. The surge motion amplitude at the natural frequency of spring in the experimental model tests EFD_1 was 0.00957 m. Such response amplitude at the natural frequency of spring in the CFD computations for grids $n = 0.75$ to $n = 2.00$ are 0.0119, 0.0079, 0.0145, 0.0144 and 0.0163 m, respectively. The differences in terms of magnitude are insignificant.

The experimental mean heave were -0.0032 and -0.0030 m, respectively for EFD_1 and EFD_2. The MEAN value of heave for the grids $n = 0.5$ to $n = 2.00$ are -0.00660, -0.00203, -0.00347, -0.00323, -0.00308 and -0.00316 m, which are close to the calm water heave (sinkage at COG) and close to EFD data for most of grids except the coarsest

ones.

The experimental mean pitch were 0.134 and -0.319 deg, respectively for EFD_1 and EFD_2, in which negative mean pitch is measured in EFD_2 contrary to the other EFD_1 and similar to what is seen in $\lambda/L = 0.6$. The MEAN value of pitch for the grids $n = 0.5$ to $n = 2.00$ are 0.1372, 0.1333, 0.1310, 0.1316, 0.1308 and 0.1318 deg, which are close to the calm water pitch (trim at COG) and the EFD_1 data considering the magnitudes in deg.

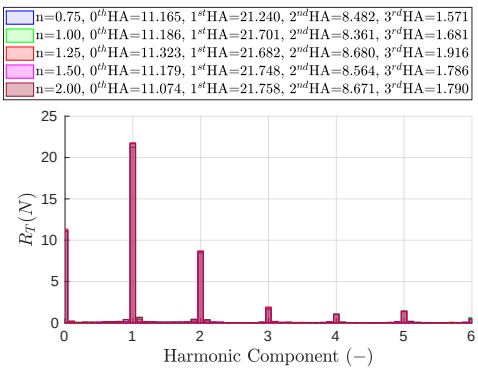

(a) FFT results.

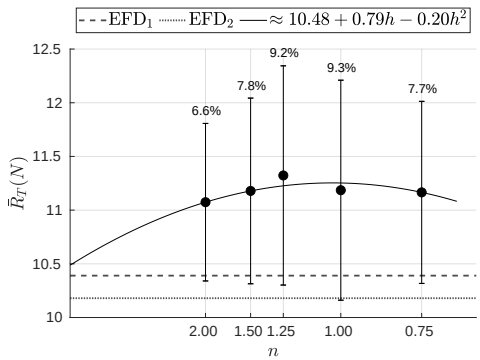

(b) V&V for the 0th HA of R_T.

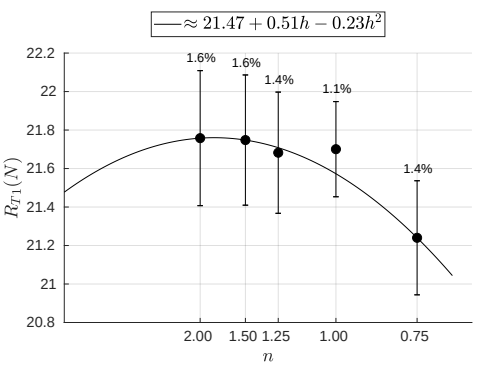

(c) Verification of the 1st HA of R_T.

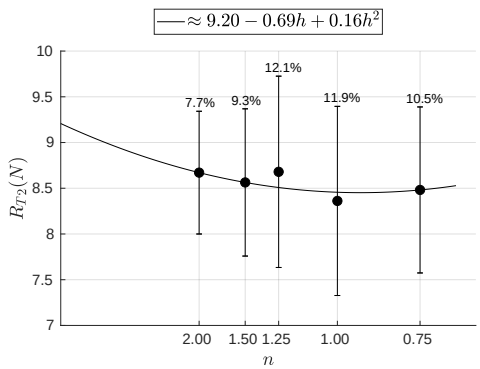

(d) Verification of the 2nd HA of R_T.

Figure 5.35: Fourier analysis results and grid convergence study on the total resistance harmonic amplitudes in regular head wave $\lambda/L = 1.1$.

The MEAN (time-averaged over $10T_E$ time window) of surface averaged $\bar{y}^+$ over the wetted surface area of the ship (i.e., $\bar{\bar{y}}^+$) for the grids $n = 0.50$ to $n = 2.00$ are approximately 214, 139, 103, 82, 68 and 50, which are close to the calm water values in each grid. The MEAN of wetted surface area in all grids are approximately 2.79 m^2 which is close to the calm water value as well as the corresponding value from the shortest studies wave length.

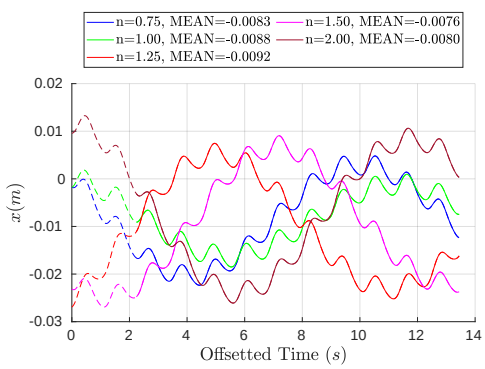

(a) Surge motion time series.

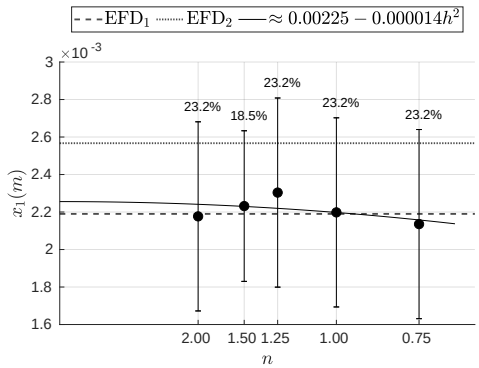

(b) V&V for the 1st HA of surge x_1.

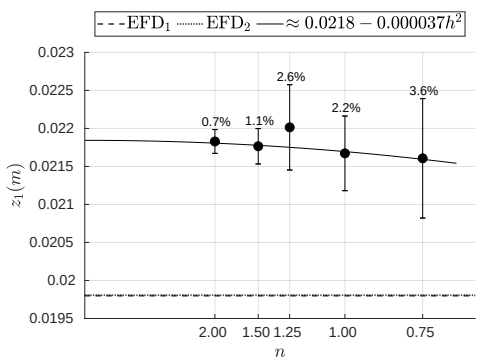

(c) V&V for the 1st HA of heave z_1.

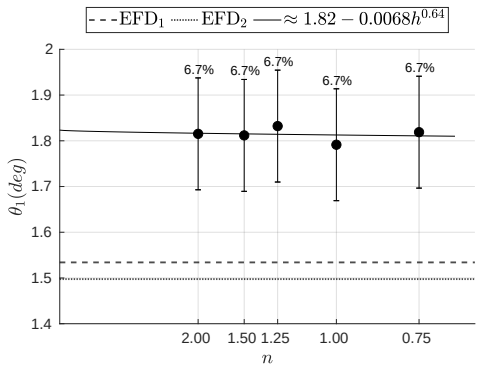

(d) V&V for the 1st HA of pitch θ_1.

Figure 5.36: V&V on the motion responses 1st harmonic amplitudes in regular head wave $\lambda/L = 1.1$.

$\lambda/L = 1.6$

Only the grid $n = 1.00$ is considered in the CFD simulations of ship responses in $\lambda/L = 1.6$, therefore, there is no grid convergence study performed for this wave. The resistance time series and its moving average are shown in Figure 5.37.

The selected time window for $\lambda/L = 1.6$ is $8 \times T_E \approx 11.30\ s$ which is close to the spring natural period $T_{Spring} \approx 11.25$. Unfortunately, the defined convergence criterion is not satisfied in this wave length as the STD%RMS $> 2\%$ for the periodic moving average with a moving window of $2T_E$, even after running the simulation for a long physical time. This may reflect that the defined convergence criterion is too conservative for this wave length as the effects of spring are seen on the moving average of resistance time series, see Figure 5.37b. The MEAN values are calculated on a $8T_E$ time window. Fourier analysis of time series is also performed on the same time window.

The FFT results of resistance as well as the time series of surge motion are shown

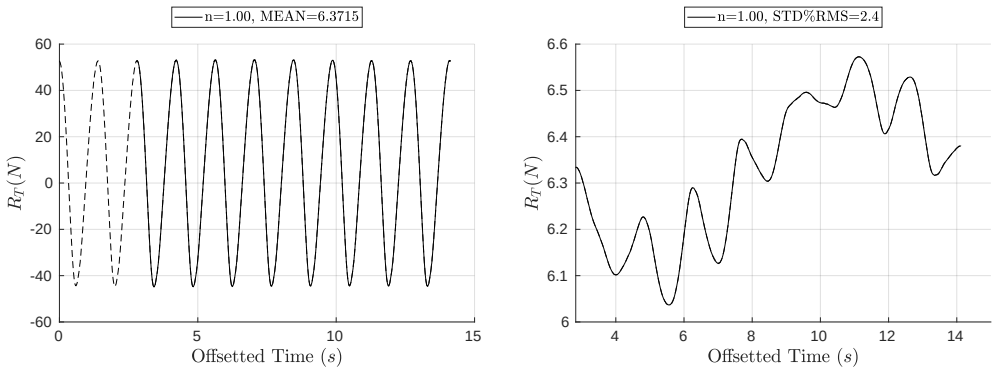

(a) Resistance time series.

(b) Resistance periodic moving average.

Figure 5.37: Resistance time series and its periodic moving average (on a $2T_E$ moving window) in $\lambda/L = 1.6$. The MEAN values are derived on a $8T_E$ time window.

in Figure 5.38. The dominating harmonic amplitudes of resistance are the 0th, 1st and 2nd component. The 0th harmonic amplitude of resistance is identical to the absolute of MEAN values $\bar{R}_T$ given in the legend of Figure 5.37a.

The mean of the measured force by dynamometer (i.e., representing $\bar{R}_T$ in model tests) was 5.98 N in EFD_1 and 6.13 N in EFD_2. The MEAN of total resistance in the current wave simulation computed to be 6.37 N which is comparable to the EFD data. The measured wave height in EFD_1 and EFD_2 were about 0.056 and 0.057 m, respectively, which are close to the target wave height $H = 0.06$ m.

A large surge motion amplitude in the spring natural frequency can be seen in the surge motion time series shown in Figure 5.38b. Therefore, the location of carriage-fixed planes with respect to the hull can change significantly during the ship response. This may introduce a potential source of discrepancy for EFD and CFD wake comparison, especially in the case of different EFD and CFD external force F_0 consideration which results in different mean surge values. Unfortunately, there is no information available about the mean surge in experimental data.

The 1st harmonic amplitude of surge in EFD_1 and EFD_2 are 0.0072 and 0.0073 m. The 1st harmonic amplitude of heave in EFD_1 and EFD_2 are 0.0264 and 0.0260 m. The 1st harmonic amplitude of pitch in EFD_1 and EFD_2 are 1.793 and 1.747 deg. The 1st harmonic amplitude of surge, heave and pitch motions for grid $n = 1.00$ are 0.0078 m 0.0278 m and 2.128 deg, respectively, which are close to the EFD data except for the pitch motion.

The surge motion amplitude at the natural frequency of spring in the experimental model tests EFD_1 was 0.0093 m. The corresponding value from the CFD computations for grids $n = 1.00$ is 0.0167 m.

The experimental mean heave was -0.0028 and -0.0023 m, respectively for EFD_1 and EFD_2. The MEAN value of heave for the grid $n = 1.00$ is -0.0032 m, which is close to the calm water heave (sinkage at COG) and close to the EFD data. The experimental mean

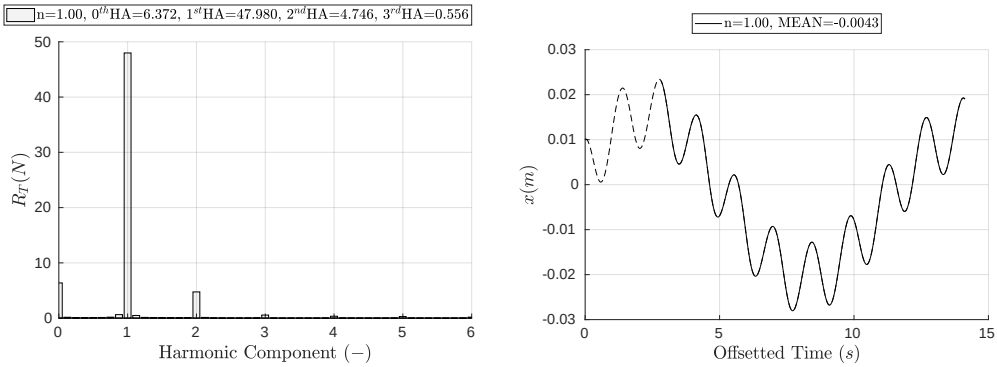

(a) FFT results of resistance.

(b) Surge motion time series.

Figure 5.38: Fourier analysis results of resistance together with time series of surge motion in $\lambda/L = 1.6$.

pitch were 0.134 and -0.177 *deg*, respectively for EFD_1 and EFD_2, in which negative mean pitch is measured contrary to other experimental data and similar to what is seen in $\lambda/L = 0.6$ and 1.1. The MEAN value of pitch for the grid $n = 1.00$ is 0.116 *deg*, which is close to the calm water pitch (trim at COG) and the EFD data considering the magnitudes in *deg*.

The MEAN (time-averaged over $8T_E$ time window) of surface averaged $\bar{y}^+$ over the wetted surface area of ship for the grid $n = 1.00$ is approximately 100 which is close to the calm water value in the same grid. The MEAN of wetted surface area is approximately 2.78 m^2 which is close to the calm water value. The deviation of the computed wetted surface area in all the studies waves from the calm water value is insignificant.

5.7.2 Wake

In this section, the verification and validation of wake is carried out for the simulations in regular head waves. Moreover, in order to have a better understanding of the time instances of which the wake computations and SPIV measurements considered, the reconstructed time series of the important responses are provided for both EFD and CFD.

The reconstruction of time series is carried out using the Fourier series, Equation 4.13, in order to generate the time series of responses for 1 encountered wave period T_E in each wave condition. In such Fourier series, the harmonic amplitudes and phases derived from the FFT calculations (in the chosen time window in each wave condition) are used. In order to make all the reconstructed time series compatible for EFD and CFD, the origin of time $t/T_E = 0$ in the reconstructed time series is defined as when the wave crest is at the initial position of the ship fore perpendicular.

It should be noted that the CFD wake is only recorded for the last encountered wave in each simulation. In order to make sure that the reconstructed responses also represent the responses obtained from the last wave encounter period, the time series

of different responses in the last encountered wave in each simulation is also compared to the reconstructed time series based on the FFT results in the chosen time window. However, the last encountered wave in each simulation does not necessarily start from the time when the incident wave crest is at the initial position of ship fore perpendicular. Therefore, the origin of time ($t/T_E = 0$) for the time series of the last encountered wave in each simulation should be synced with the time origin of the reconstructed time series (i.e., when the wave crest is at the initial position of fore perpendicular). To achieve this, first, each of the time series of the last encountered wave is divided into two parts; part one from the beginning of the time series to the time in which the wave crest is at the initial position of fore perpendicular, and part two from the time in which the wave crest is at the initial position of fore perpendicular to the end of signal. Then these parts are swapped, hence the part two starts from a synced $t/T_E = 0$ and part one is simply attached to the end of part two. The attachment point is mainly overlap for most of the responses because the behavior of the ship is harmonized with the encountered wave period. However, this is not true for the surge motion response in which (due to the presence of spring) the ship experience an extra harmonic behavior at the spring natural period. Therefore, the attachment point often does not overlap for the surge motion in the synced last T_E time series.

The wave elevation in CFD is monitored at the probe $Y1$ and longitudinal location $X1$, see Figure 5.11, hence in the vicinity of forcing zone. Notice that the wave elevation close to the hull for the hull performance simulations is affected by the hull, therefore, it is not feasible to use the monitored wave elevation at other locations closer to the hull. The monitored wave elevation is then offsetted in time in order to estimate the expected wave at the initial position of ship fore perpendicular using the 5th order Stokes wave mean velocity and the ship velocity. However, based on the wave propagation simulations investigations in Section 5.5, it is seen that the wave elevation may be affected by different local refinement zones and the moving overset region in different simulations for the probes closer to the hull. This might be counted as another source of discrepancy as there is no practical way to estimate the exact wave elevation at the ship fore perpendicular in the hull performance simulations. However, it should be reminded that the wave elevation error mainly remained insignificant (i.e., under 3%) for the grids $n = 1.00$, $n = 1.50$ and $n = 2.00$ based on the wave propagation simulation results. The wave elevation measurements in the towing tank tests is also carried out at some distance in front of the hull, explained in Section 5.3, and then offsetted in time in order to represent the wave elevation at ship fore perpendicular.

Although the harmonic amplitudes of different responses are analyzed in Section 5.7.1, the harmonic phases are disregarded. In this section, a qualitative analysis can be performed on the harmonic phases based on the reconstructed time series. The time origin for both the CFD and EFD data are now overlap, hence the harmonic phases can be qualitatively understood based on the phase differences in the reconstructed time series.

It should be noticed that the instantaneous position of the carriage-fixed planes with respect to the hull may vary between different grids as the hull is subjected to different instantaneous surge values (due to the presence of spring) in each grid. In other words, the hull moves in longitudinal direction due to its surge motion and since the instantaneous surge values are different between different grids, the instantaneous position of the carriage-

fixed planes with respect to the hull may vary between different grids. This should be highlighted as an important source of discrepancy in the wake comparisons. The difference in Reynolds number for different data sets should not be overlooked as well. Moreover, the CFD wake is only recorded at the computed time steps, therefore, there might be a small time difference between the EFD and CFD wake. In the following sections, the wake analysis is carried out for each wave length.

$\lambda/L = 0.6$

The surface-averaged nominal wake computed on the hull-fixed propeller disc for different grids in $\lambda/L = 0.6$ is shown in Figure 5.39. In this figure, the time series of each velocity component of the nominal wake as well as the Fourier analysis (on a $15T_E$ time window) of the axial velocity component for different grids are shown.

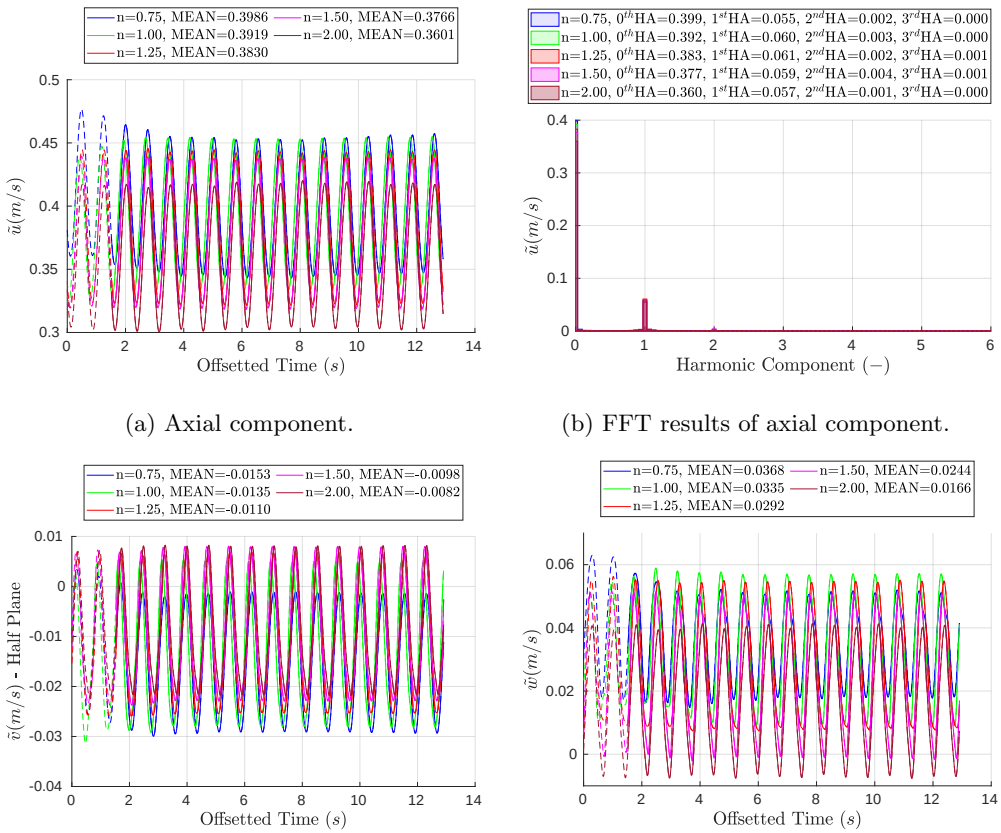

(a) Axial component.

(b) FFT results of axial component.

(c) Tangential Y component.

(d) Tangential Z component.

Figure 5.39: CFD time series of the surface-averaged nominal wake velocity components on the hull-fixed propeller disc and FFT analysis of the axial velocity component in a $15T_E$ time window in $\lambda/L = 0.6$.

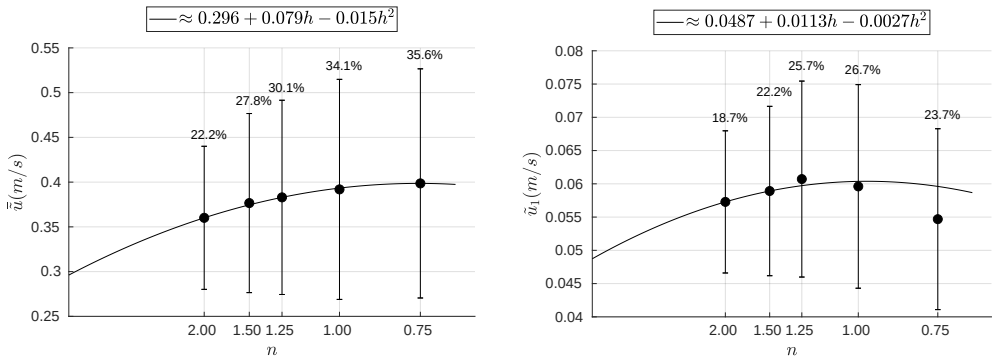

(a) MEAN of axial component. (b) 1st harmonic amplitude of axial component.

Figure 5.40: Grid convergence study of MEAN and 1st harmonic amplitude of the axial velocity component derived from a $15T_E$ time window in $\lambda/L = 0.6$.

The dominant FFT amplitudes for the axial velocity component are shown in Figure 5.39b. The time series of the axial velocity component in Figures 5.39a exhibit a harmonic behavior with respect to the wave encounter frequency, hence the analysis of the last encountered wave in the simulations can be generalized for the whole time window.

The MEAN values are given in the plot legends in Figures 5.39a, 5.39c and 5.39d for each grid and velocity component for the chosen time window. The magnitude of the MEAN values for all three velocity components for all the grids are larger than the corresponding calm water values shown in Figure 5.24, which indicate a fuller wake in this wave length relative to calm water. Similar to the trend observed from calm water simulations, the MEAN axial velocity decreases as the refinement level increases. The comparison between the wake in calm water and in regular head waves is carried out in Section 5.8. The MEAN values of $\tilde{u}$, $\tilde{v}$ and $\tilde{w}$ for grid $n = 0.50$ are about 0.442, -0.022 and 0.049 m/s, respectively, which are quite different from the other grids.

The FFT results of the axial component, given in Figure 5.39b, show that the 0th harmonic amplitude (i.e., equal to the MEAN value in each respective grid) and the 1st harmonic amplitude are the dominating components in this wave length. Therefore, the grid convergence study is carried out for these components and the results are shown in Figure 5.40. The grid convergence study for the tangential velocity components are planed to be done in future. The numerical uncertainties of the 0th and the 1st harmonic amplitude of the MEAN axial velocity component are between 18% and 36%, which are relatively large in comparison to the numerical uncertainty of the motion and resistance responses in this wave length, however, relatively similar to the numerical uncertainties of the calm water MEAN axial velocity.

Before comparing the EFD and CFD wake, it is crucial to understand what are the exact instances of time for SPIV measurements, to be able to find an equivalent time instances in the CFD computations. As it is mentioned before, it is decided to study the reconstructed time series as well as the synced last encountered wave time series (in which the CFD wake is recorded in the simulations) for different responses to figure out the

SPIV time instances. Such time series are shown in Figures 5.41 and 5.42. Different CFD responses are reconstructed up to different harmonic components (HCs, i.e., harmonic amplitudes and phases) using the Fourier series. These are given in the sub-figure captions for each respective reconstructed response time series. The time series from EFD_1 are reconstructed only up to the 1st harmonic components since higher harmonic components are not available from this data set. However, the reconstruction in EFD_2 is performed using up to the 2nd harmonic components as the dominating harmonic amplitudes in the respective FFT analysis.

The wave elevation at fore perpendicular is shown in Figure 5.41a. As it was mentioned before, the measured wave height in EFD_1 in $\lambda/L = 0.6$ was much larger than the target value $H = 0.06\ m$. The wave elevation for EFD_2 is slightly lower than H. On the other hand, the CFD wave elevation in all grids are relatively similar to the analytical wave. Moreover, the instantaneous ship velocity in Figure 5.41b exhibit almost similar trend in all grids.

In Figure 5.41c, the EFD surge motion in both experimental data has $\approx 180\ deg$ phase difference compared to the CFD data in all the grids. The same discrepancy is seen from the other wave lengths. More information from the towing tank tests is needed to understand this difference. However, the author's hypothesis is that the difference between the surge motion coordinate and a misleading surge definition are the main cause of this discrepancy. Other than that, the surge motion is relatively similar in terms of the 1st harmonic amplitude between EFD and CFD, as it is seen in Figure 5.33b. The discontinuity of surge motion response for the last T_E time series is due to the surge response in the spring natural frequency as explained in Section 5.7.2. Due to the same reason, the last T_E time series do not match the reconstructed time series of surge motion.

The EFD and CFD heave motion time series in Figure 5.41d are comparable in all cases except for EFD_1 which is $\approx 10 - 20\ deg$ out of phase in comparison to CFD and EFD_2 data. Moreover, the mean surge of grid $n = 0.75$ is different from the other grids and both EFD data. In Figure 5.41e, the pitch responses in CFD are well aligned for all grids, however, both experimental data are rather different. There is $\approx 10 - 20\ deg$ phase difference in EFD_1 compared to CFD and EFD_2 similar to the heave response.

The phase difference of $\approx 10 - 20 deg$ in EFD_1 in comparison to EFD_2 and CFD might originate from the fact that the initial position of ship fore perpendicular is used to offset the measured and computed wave elevation and not the instantaneous one. The ship motion responses are measured at the ship COG, consequently, if the mean surge of the ship is not zero, then the longitudinal position of COG with respect to the carriage (on which the wave probe is mounted on) would be different. This means that the longitudinal distance between the wave probe and the ship fore perpendicular is not equal to its initial value. As a result, there will be a phase shift for the motions responses at the ship COG. If, for instance, the external force F_0 is different, then the mean value of surge (i.e., mean value of spring stretch/compression) during the ship responses in regular head waves would be different. Then offsetting the wave elevation time series based on the initial position of the ship fore perpendicular does not include the actual position of the ship COG, hence the motions phases at COG are not correctly offsetted. This is one of the complex effects from the spring and there is no straightforward way (due to the limited information from the model tests) to include such effects into the current investigations.

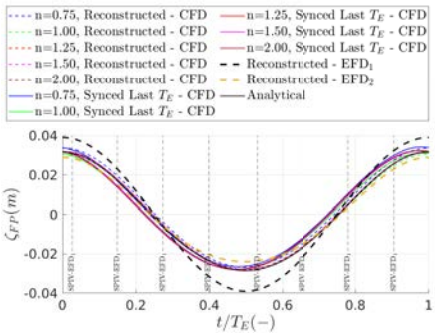

(a) Reconstructed CFD up to 5th HCs.

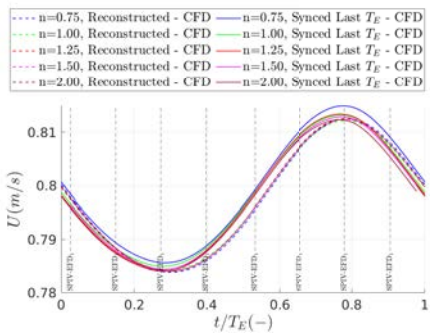

(b) Reconstructed CFD up to 2nd HCs.

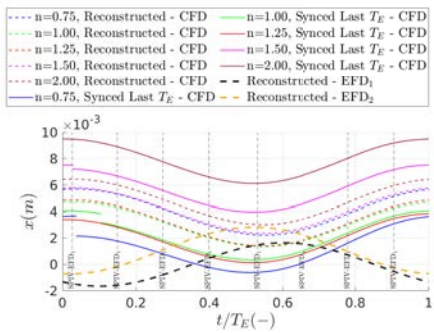

(c) Reconstructed CFD up to 2nd HCs.

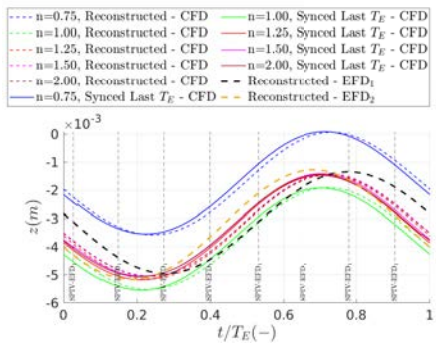

(d) Reconstructed CFD up to 2nd HCs.

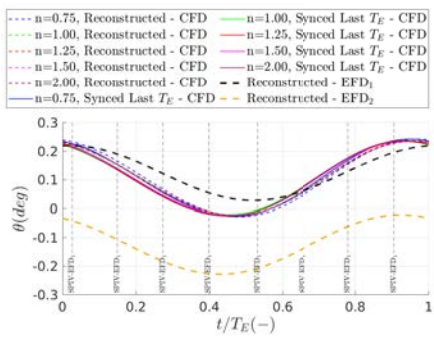

(e) Reconstructed CFD up to 2nd HCs.

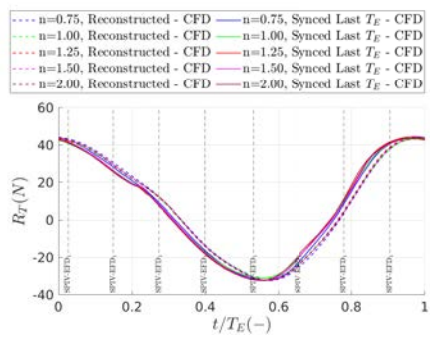

(f) Reconstructed CFD up to 5th HCs.

Figure 5.41: Reconstructed and synced last T_E time series of (a) wave elevation at fore perpendicular, (b) actual ship velocity, (c) surge, (d) heave, (e) pitch and (f) total resistance in $\lambda/L = 0.6$. EFD$_1$ and EFD$_2$ are reconstructed up to the 1st and 2nd HCs, respectively. SPIV time instances are represented by black vertical lines.

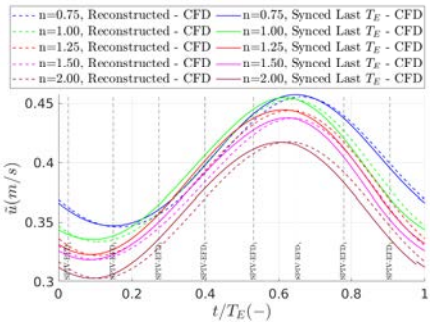

(a) Reconstructed CFD up to 2nd HCs.

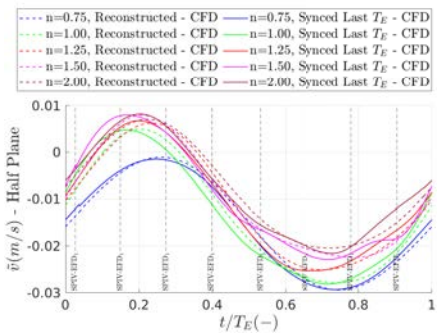

(b) Reconstructed CFD up to 2nd HCs.

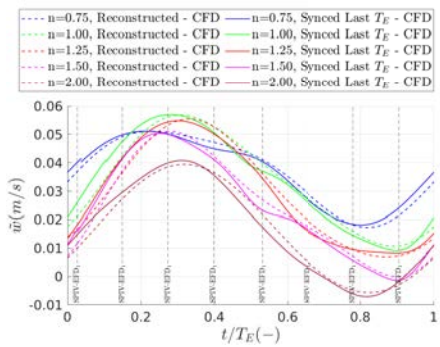

(c) Reconstructed CFD up to 2nd HCs.

Figure 5.42: Reconstructed and synced last T_E time series of (a) axial velocity component, (b) tangential Y velocity component and (c) tangential Z velocity component in $\lambda/L = 0.6$. SPIV time instances are represented by black vertical lines.

Therefore, this effect is accounted as one of potential sources of discrepancy in this study.

The reconstructed pitch obtained from EFD_2 is an outlier and has a negative mean value. Despite the observed discrepancies between the computed and measured wave elevations, motions and hull speed, the resistance time series for all CFD grids are rather similar, see Figure 5.41f, which suggest that the total resistance is insensitive to the reported discrepancies.

The surface averaged wake velocities on the propeller disc are shown in Figure 5.42. Opposite to the conclusions made for the total resistance, the surface averaged wake velocity components obtained from different grids deviate from each other, which shows a considerable dependency on the hull motions and speed.

The CFD and EFD wake comparison is shown in Figures 5.43 and 5.44. The SPIV measurements in $\lambda/L = 0.6$ is only carried out in EFD_1. Besides the possible sources of discrepancy mentioned in Section 5.3.1, there is also a phase difference between EFD_1 responses and CFD that can affect the consistency of actual t/T_E between CFD and EFD.

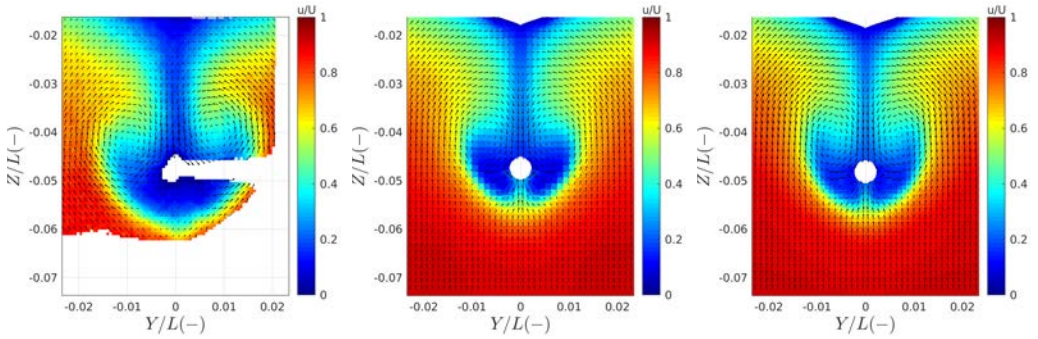

(a) EFD_1, $t/T_E = 0.274$. (b) $n = 0.75$, $t/T_E = 0.274$. (c) $n = 1.00$, $t/T_E = 0.273$.

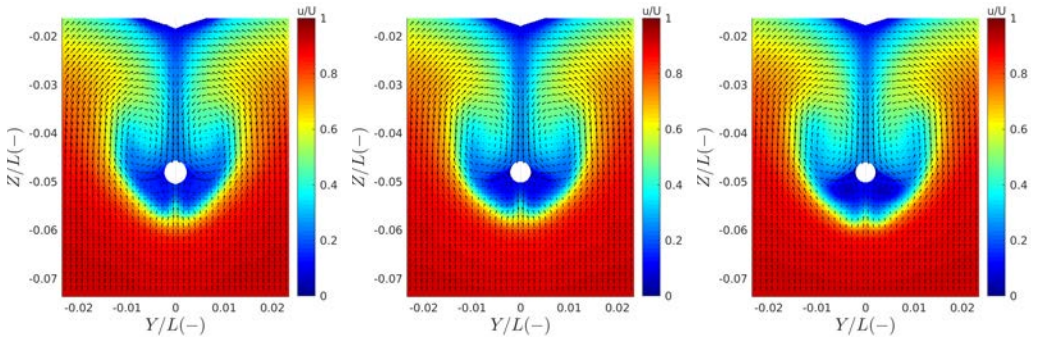

(d) $n = 1.25$, $t/T_E = 0.275$. (e) $n = 1.50$, $t/T_E = 0.274$. (f) $n = 2.00$, $t/T_E = 0.275$.

Figure 5.43: EFD and CFD wake comparison in the carriage-fixed plane at the initial position of propeller plane in $\lambda/L = 0.6$ at $t/T_E \approx 0.274$.

Therefore, there is no straightforward way to quantitatively validate the computed wave against experimental one, hence only a visualization comparison can be performed. On the other hand, inclusion of all SPIV time instances in the this thesis and comparison with the data from all grids is not inline with the defined objectives. Therefore, it is decided to compare the wake for all grids only in some selective time instances t/T_E. Moreover, the CFD t/T_E is not exactly the same as EFD time instances due to the time discretization (time step size) in the simulations.

One obvious difference between the EFD and CFD wake in both t/T_E instances is the computed wake under the hub in all grids. It is clear that the symmetry boundary condition defined in the CFD simulations forced the normal flow velocities across the symmetry plane to zero. However, this is not the case in model tests as the flow can commute to different sides due to the asymmetric nature of the problem. Moreover, in both t/T_E, the finer grids predicted larger bilge vortex in comparison to the coarser ones and it can be seen that the CFD wake in finer grids are becoming more similar to the SPIV wake. In both of the presented time instances, a secondary vortex is generated under the hub due to the moving shaft. The secondary vortex is less pronounced in the SPIV wake.

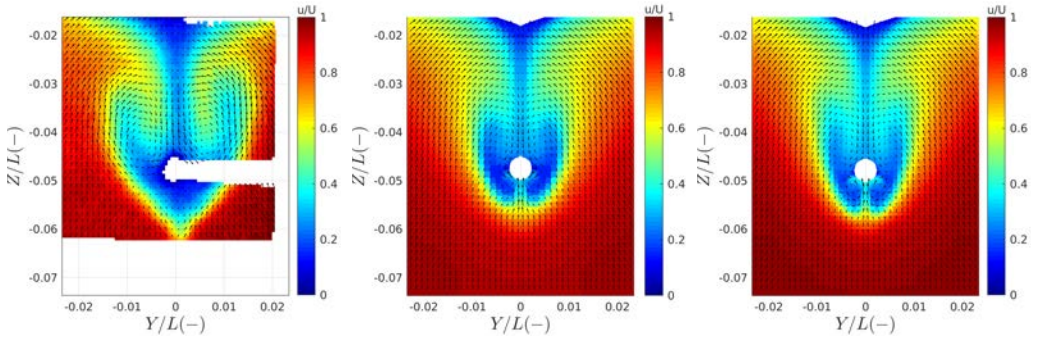

(a) EFD$_1$, $t/T_E = 0.532$. (b) $n = 0.75$, $t/T_E = 0.532$. (c) $n = 1.00$, $t/T_E = 0.533$.

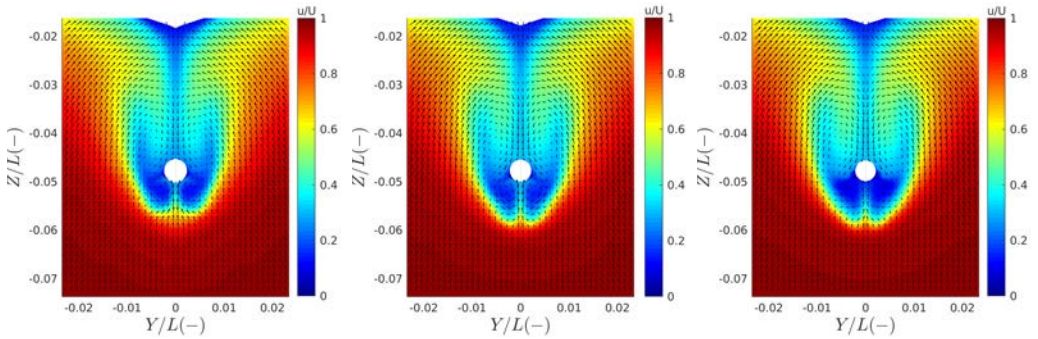

(d) $n = 1.25$, $t/T_E = 0.531$. (e) $n = 1.50$, $t/T_E = 0.532$. (f) $n = 2.00$, $t/T_E = 0.531$.

Figure 5.44: EFD and CFD wake comparison in the carriage-fixed plane at the initial position of propeller plane in $\lambda/L = 0.6$ at $t/T_E \approx 0.532$.

$\lambda/L = 1.1$

The surface-averaged nominal wake computed on the hull-fixed propeller disc for different grids in $\lambda/L = 1.1$ is shown in Figure 5.45. The Fourier analysis results (on a $10T_E$ time window) for the axial velocity component, shown in Figure 5.45b, confirm a harmonic behavior with respect to the wave encounter frequency, similar to $\lambda/L = 0.6$.

The MEAN values are given in the plot legends in Figures 5.45a, 5.45c and 5.45d for each grid and velocity component for the chosen time window. Similar to $\lambda/L = 0.6$, the MEAN values (in terms of magnitude) for all three velocity components for each grid are larger than the calm water values in the respective grid seen in Figure 5.24. The comparison between the wake in calm water and in regular head waves is carried out in Section 5.8. The MEAN values of $\tilde{u}$, $\tilde{v}$ for grid $n = 0.50$ are about 0.469, -0.026, respectively, which are rather close to the other grids, while the MEAN of $\tilde{w}$ is 0.047 m/s which is different from the other grids.

The FFT results of the axial component, given in Figure 5.45b, show that the 0th, 1st, 2nd and 3rd harmonic amplitudes are the dominating components in this wave length. Therefore, the grid convergence study is carried out for these components and the results

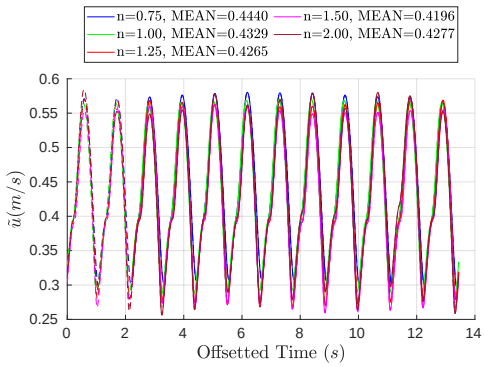

(a) Axial component.

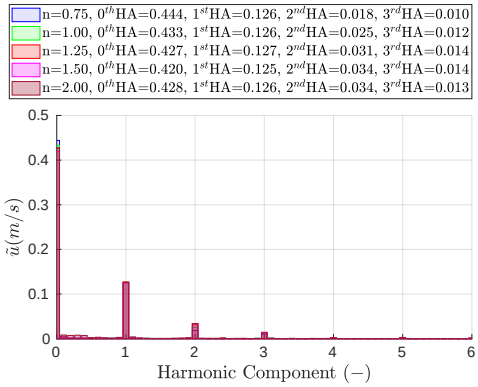

(b) FFT results of axial component.

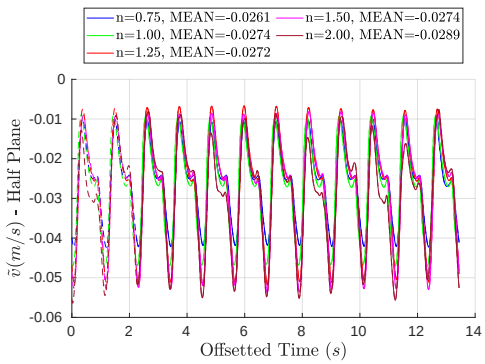

(c) Tangential Y component.

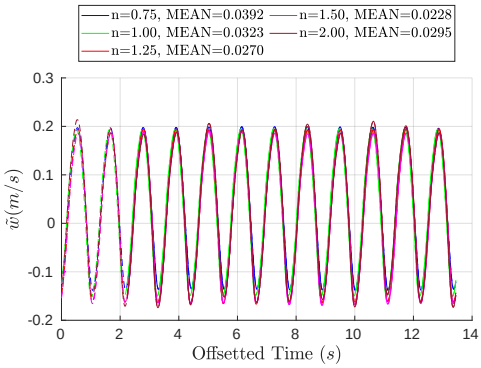

(d) Tangential Z component.

Figure 5.45: CFD time series of the surface-averaged nominal wake velocity components on the hull-fixed propeller disc and FFT analysis of the axial velocity component in a $10T_E$ time window in $\lambda/L = 1.1$.

are shown in Figure 5.46. Opposite to the large numerical uncertainties obtained for the MEAN of axial velocity component and its 1st harmonic amplitude from the shorter wave length simulations (Figure 5.40), the numerical uncertainties of these two quantities are considerably smaller.

The reconstructed time series as well as the synced last encountered wave time series (in which the CFD wake is recorded in the simulations) for different responses in $\lambda/L = 1.1$ are shown in Figures 5.47 and 5.48. The considered harmonic components in the reconstructed time series in $\lambda/L = 1.1$ is similar to the ones used in $\lambda/L = 0.6$. The wave elevation at fore perpendicular is shown in Figure 5.47a. As it was mentioned before, the measured wave height in both EFD data in $\lambda/L = 1.1$ were close to the target value $H = 0.06\ m$. The CFD wave elevation in all grids are relatively similar to the analytical wave.

The instantaneous ship velocity in Figure 5.47b exhibit almost similar trend in all

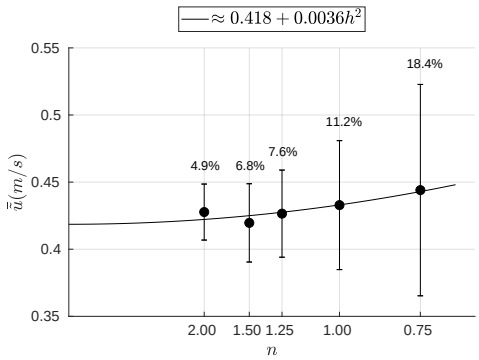

(a) MEAN of axial component.

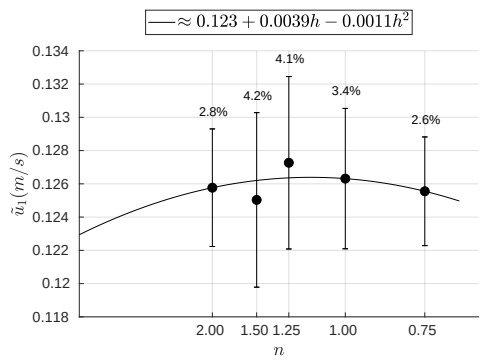

(b) 1st harmonic amplitude of axial component.

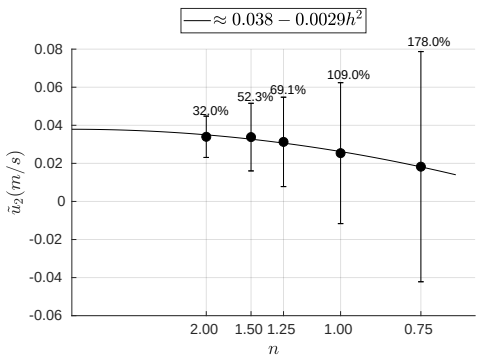

(c) 2nd harmonic amplitude of axial component.

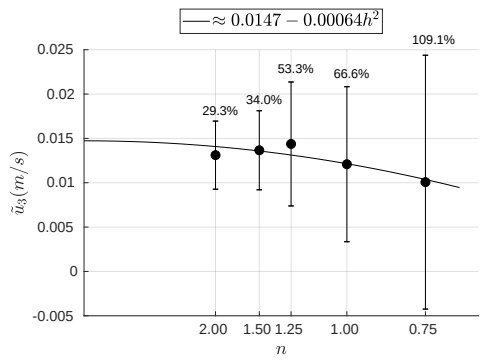

(d) 3rd harmonic amplitude of axial component.

Figure 5.46: Grid convergence study of MEAN, 1st, 2nd and 3rd harmonic amplitudes of the axial velocity component derived from a $10T_E$ time window in $\lambda/L = 1.1$.

grids for the reconstructed time series. However, the last T_E time series are relatively different. The main reason for such differences lies in the instantaneous surge motion at the last encountered wave of simulation for each grid. In Figure 5.36a, the surge motion time series of different grids are shown. Surge motion for each grid during the last T_E behave differently, see Figure 5.47c. For instance, the surge motion values for the grids $n = 1.25$ and $n = 1.50$ are negative with almost large magnitudes meaning that the spring is stretched to a large extent. Therefore, negative surge values result in positive $-Kx$ values, hence the spring force applied to the ship center of gravity is towards its forward direction resulting in an increased ship velocity. The actual ship velocity during the simulations for both $\lambda/L = 0.6$ and 1.1 are shown in Figure 5.49. As it can be seen, the spring effects are insignificant in $\lambda/L = 0.6$, while in $\lambda/L = 1.1$ such effects are notable. It should be mentioned that the MEAN values in the plots legends (i.e., computed for time windows of $15T_E$ in $\lambda/L = 0.6$ and $10T_E$ in $\lambda/L = 1.1$) are relatively similar in all grids.

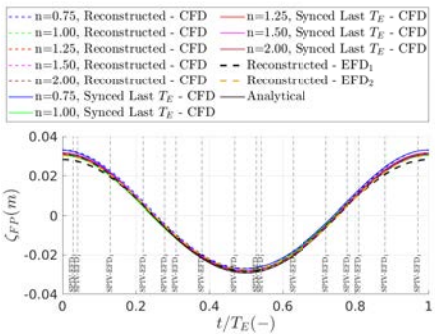

(a) Reconstructed CFD up to 5th HCs.

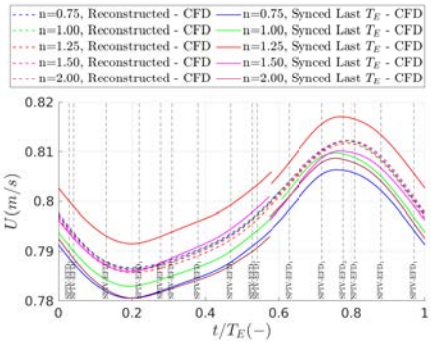

(b) Reconstructed CFD up to 2nd HCs.

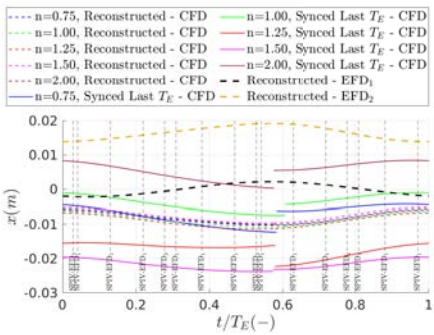

(c) Reconstructed CFD up to 2nd HCs.

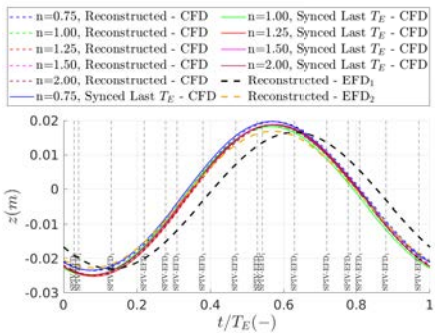

(d) Reconstructed CFD up to 2nd HCs.

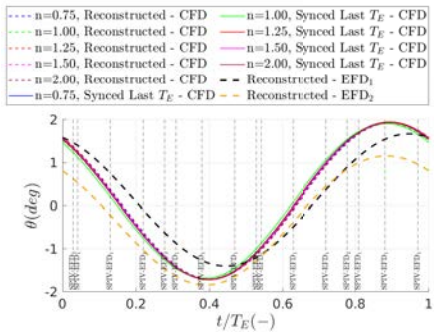

(e) Reconstructed CFD up to 2nd HCs.

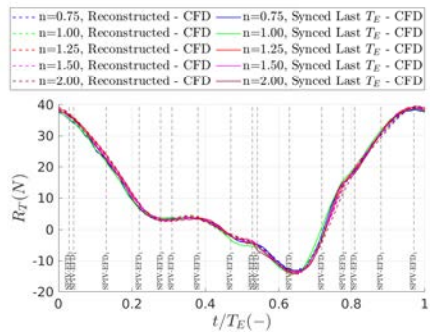

(f) Reconstructed CFD up to 5th HCs.

Figure 5.47: Reconstructed and synced last T_E time series of (a) wave elevation at fore perpendicular, (b) actual ship velocity, (c) surge, (d) heave, (e) pitch and (f) total resistance in $\lambda/L = 1.1$. EFD$_1$ and EFD$_2$ are reconstructed up to the 1st and 2nd HCs, respectively. SPIV time instances are represented by black vertical lines.

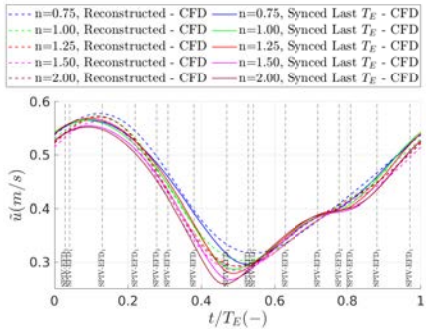

(a) Reconstructed CFD up to 2nd HCs.

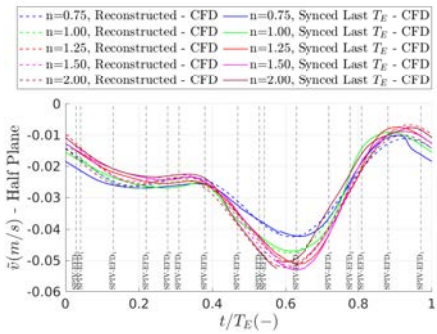

(b) Reconstructed CFD up to 2nd HCs.

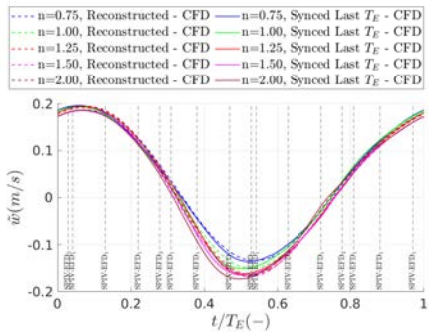

(c) Reconstructed CFD up to 2nd HCs.

Figure 5.48: Reconstructed and synced last T_E time series of (a) axial velocity component, (b) tangential Y velocity component and (c) tangential Z velocity component in $\lambda/L = 1.1$. SPIV time instances are represented by black vertical lines.

In Figure 5.47c, the EFD surge motion in both experimental data has ≈ 180 *deg* phase difference compared to the CFD data in all grids. Such differences are also seen in $\lambda/L = 0.6$. The computed 1st harmonic amplitudes are comparable to the EFD data, as it is seen in Figure 5.36b. The discontinuity of the surge motion is explained before.

The EFD and CFD heave and pitch motions time series in Figures 5.47d and 5.47e are comparable in all cases except for EFD_1 which is $\approx 10-20$ *deg* out of phase in comparison to CFD and EFD_2 data which is discussed under the results of $\lambda/L = 0.6$. Moreover, there is a negative mean pitch in EFD_2 and the pitch 1st harmonic amplitudes in both EFD data sets are lower than CFD data, as it also seen in Figure 5.36d. The resistance time series for all CFD grids are rather similar, see Figure 5.47f. The surface averaged wake velocities on the propeller disc, shown in Figure 5.48, exhibit a very similar trend in different grids, except the coarsest grid $n = 0.75$. Similar to the conclusion made in the shorter wave length, the total resistance is rather insensitive to the small deviations in the motions and ship speed obtained from different grids.

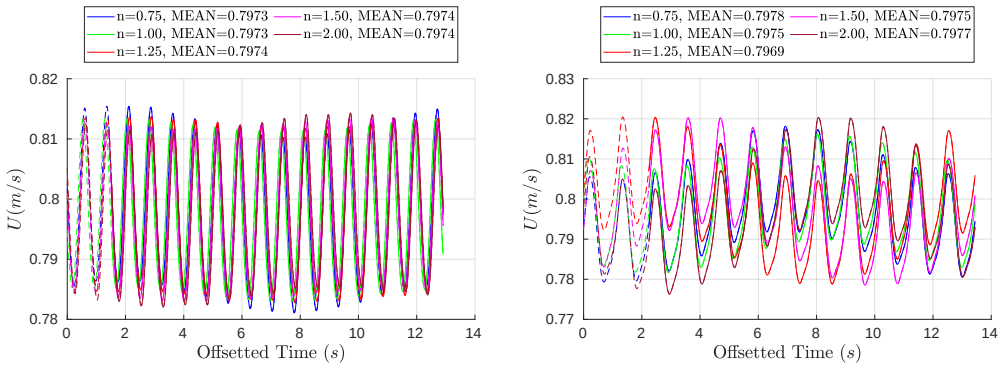

(a) Instantaneous ship velocity in $\lambda/L = 0.6$. (b) Instantaneous ship velocity in $\lambda/L = 1.1$.

Figure 5.49: Instantaneous ship velocity in CFD simulations in $\lambda/L = 0.6$ and 1.1.

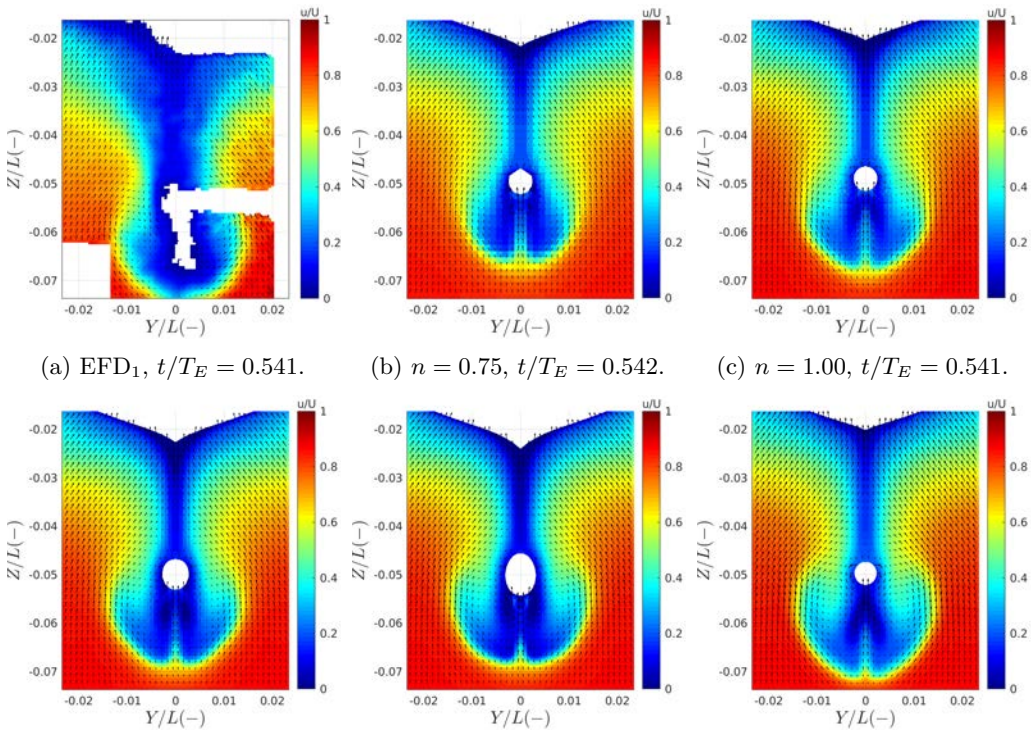

(a) EFD_1, $t/T_E = 0.541$. (b) $n = 0.75$, $t/T_E = 0.542$. (c) $n = 1.00$, $t/T_E = 0.541$.

(d) $n = 1.25$, $t/T_E = 0.542$. (e) $n = 1.50$, $t/T_E = 0.541$. (f) $n = 2.00$, $t/T_E = 0.541$.

Figure 5.50: EFD_1 and CFD wake comparison in the carriage-fixed plane at the initial position of propeller plane in $\lambda/L = 1.1$ at $t/T_E \approx 0.541$.

The CFD and EFD wake comparisons shown in Figures 5.50 and 5.51. The SPIV measurements in $\lambda/L = 1.1$ is carried out in both EFD_1 (in the carriage-fixed plane at the initial position of propeller plane) and EFD_2 (in the carriage-fixed plane at the initial position of aft perpendicular). Based on the mentioned potential sources of discrepancies, only a qualitative comparison of the EFD and CFD wakes is carried out only for two selected instances of time t/T_E.

The wake difference between EFD and CFD under the hub due to the symmetry boundary conditions in the CFD simulations is observed, similar to $\lambda/L = 0.6$. As it was mentioned before, the surge values for the grids $n = 1.25$ and $n = 1.50$ are rather large negative values, and since the plane is fixed on the carriage, the hull is closer to the plane in these grids. Therefore, the hub region in the wake contour plots in Figures 5.50d and 5.50e are larger meaning that the hull has moved backwards and penetrate more into the carriage-fixed plane. In both t/T_E, the finer grids predicted larger bilge vortex in comparison to the coarser ones.

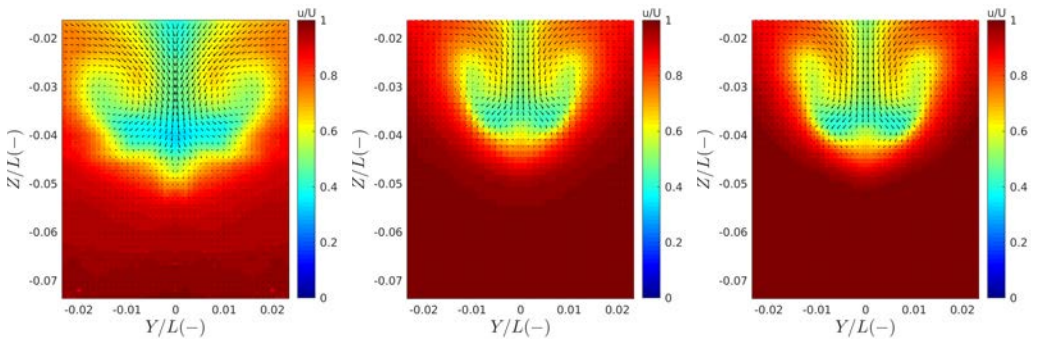

(a) EFD_2, $t/T_E = 0.028$. (b) $n = 0.75$, $t/T_E = 0.029$. (c) $n = 1.00$, $t/T_E = 0.027$.

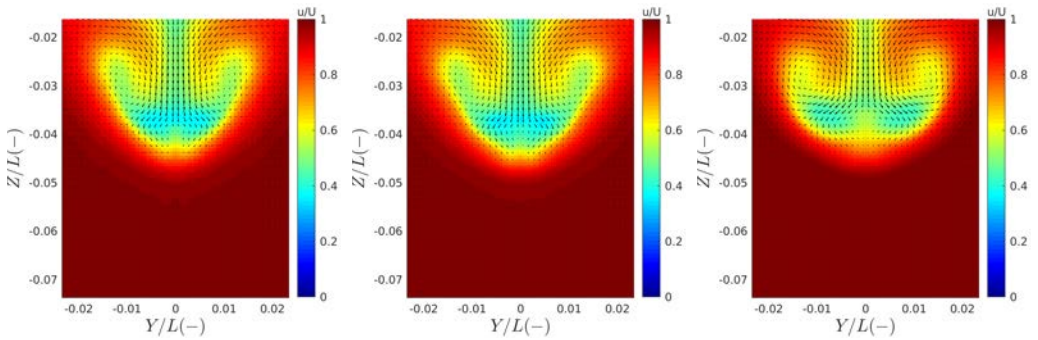

(d) $n = 1.25$, $t/T_E = 0.028$. (e) $n = 1.50$, $t/T_E = 0.029$. (f) $n = 2.00$, $t/T_E = 0.028$.

Figure 5.51: EFD_2 and CFD wake comparison in the carriage-fixed plane at the initial position of aft perpendicular in $\lambda/L = 1.1$ at $t/T_E \approx 0.028$.

$\lambda/L = 1.6$

The surface-averaged nominal wake computed on the hull-fixed propeller disc in $\lambda/L = 1.6$ is shown in Figure 5.52. The CFD computations in this wave length are only carried out in grid $n = 1.00$. The Fourier analysis results (on a $8T_E$ time window) for the axial velocity component, shown in Figure 5.52b, confirm a harmonic behavior with respect to the wave encounter frequency, similar to $\lambda/L = 0.6$ and 1.1.

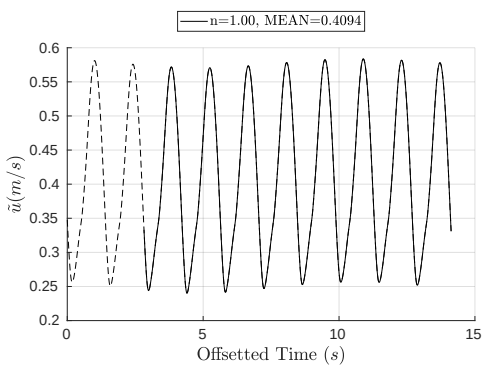

(a) Axial component.

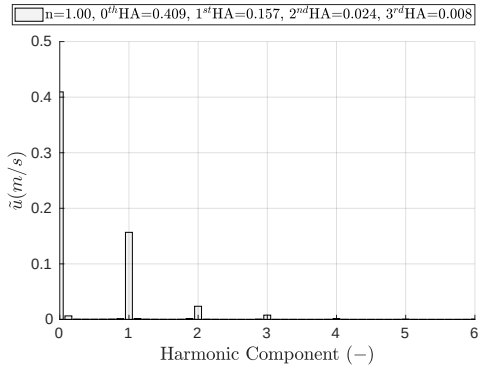

(b) FFT results of axial component.

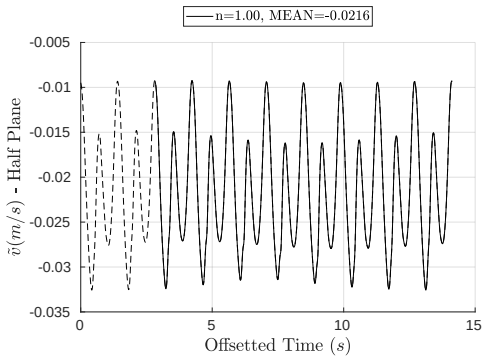

(c) Tangential Y component.

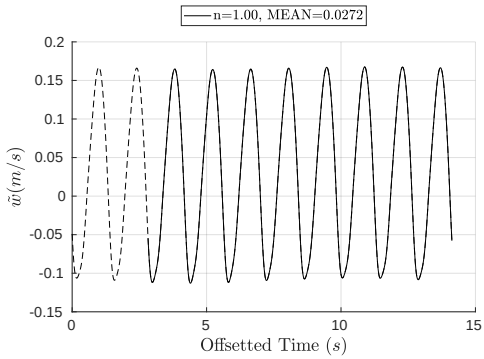

(d) Tangential Z component.

Figure 5.52: CFD time series of the surface-averaged nominal wake velocity components on the hull-fixed propeller disc and FFT analysis of the axial velocity component in a $8T_E$ time window in $\lambda/L = 1.6$.

The MEAN values are given in the plot legends in Figures 5.52a, 5.52c and 5.52d for each velocity component for the chosen time window. Similar to $\lambda/L = 0.6$ and 1.1, the MEAN values (in terms of magnitude) for all three velocity components are larger than the calm water values in the grid $n = 1.00$ seen in Figure 5.24. The comparison between the wake in calm water and in regular head waves is carried out in Section 5.8.

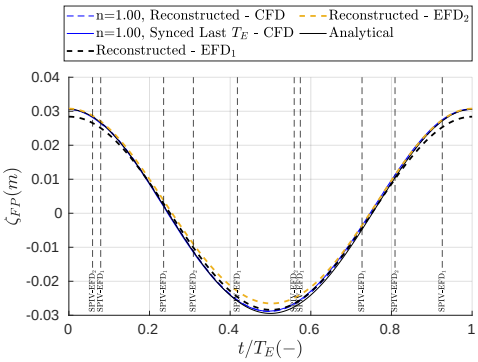

(a) Reconstructed CFD up to 5th HCs.

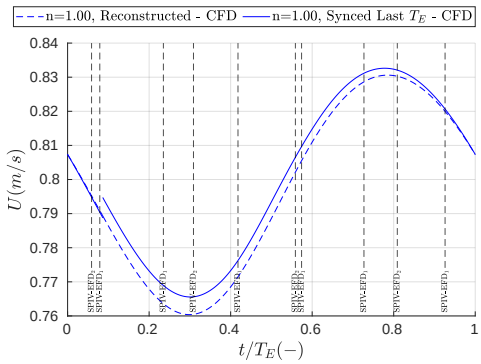

(b) Reconstructed CFD up to 2nd HCs.

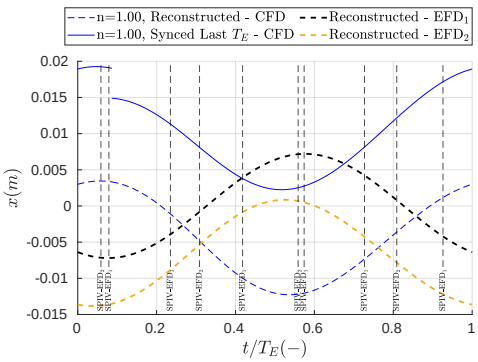

(c) Reconstructed CFD up to 2nd HCs.

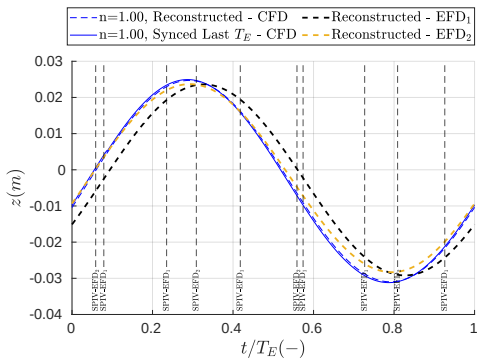

(d) Reconstructed CFD up to 2nd HCs.

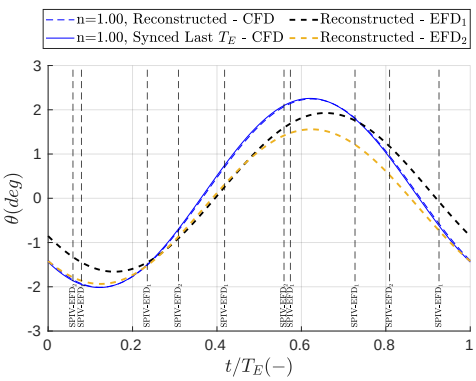

(e) Reconstructed CFD up to 2nd HCs.

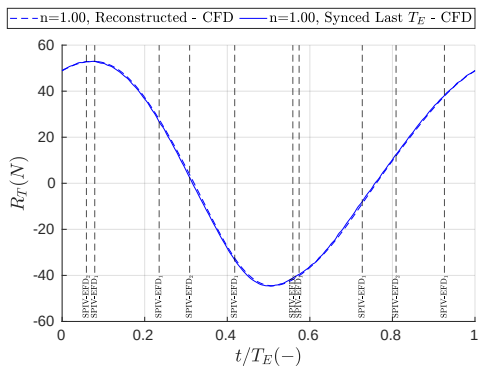

(f) Reconstructed CFD up to 5th HCs.

Figure 5.53: Reconstructed and synced last T_E time series of (a) wave elevation at fore perpendicular, (b) actual ship velocity, (c) surge, (d) heave, (e) pitch and (f) total resistance in $\lambda/L = 1.6$. EFD$_1$ and EFD$_2$ are reconstructed up to the 1st and 2nd HCs, respectively. SPIV time instances are represented by black vertical lines.

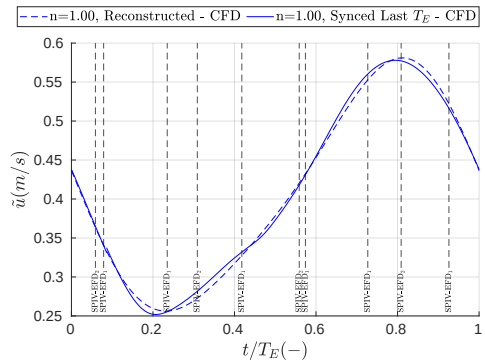

(a) Reconstructed CFD up to 2nd HCs.

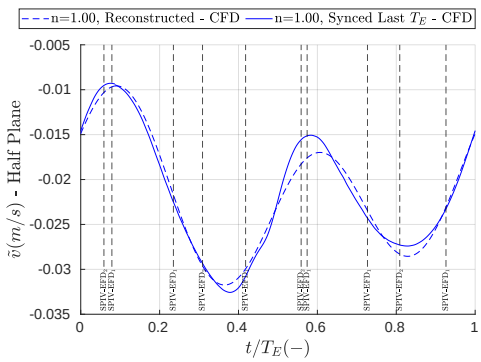

(b) Reconstructed CFD up to 2nd HCs.

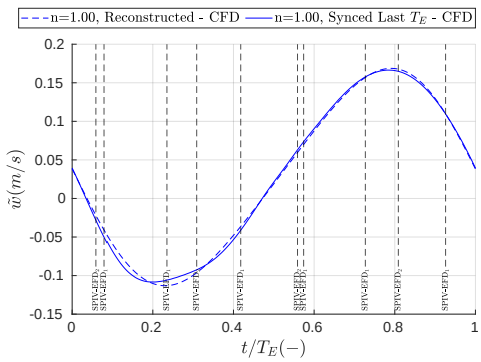

(c) Reconstructed CFD up to 2nd HCs.

Figure 5.54: Reconstructed and synced last T_E time series of (a) axial velocity component, (b) tangential Y velocity component and (c) tangential Z velocity component in $\lambda/L = 1.6$. SPIV time instances are represented by black vertical lines.

The FFT results of the axial component, given in Figure 5.52b, show that the 0th, 1st, 2nd and, to some extent, the 3rd harmonic amplitudes are the dominating components in this wave length.

The reconstructed time series as well as the synced last encountered wave time series (in which the CFD wake is recorded in the simulations) for different responses in $\lambda/L = 1.6$ are shown in Figures 5.53 and 5.54. The considered harmonic components in the reconstructed time series in $\lambda/L = 1.6$ is similar to the ones used in $\lambda/L = 0.6$ and 1.1. The wave elevation at fore perpendicular is shown in Figure 5.53a. As it was mentioned before, the measured wave height in both EFD data in $\lambda/L = 1.6$ were close to the target value $H = 0.06\ m$. The CFD wave elevation is also relatively similar to the analytical wave.

The instantaneous ship velocity is shown in Figure 5.53b. It is worth mentioning that the instantaneous velocity in $\lambda/L = 1.6$ is also affected by the spring similar to $\lambda/L = 1.1$, due to the large magnitude surge motions in the natural frequency of the spring (the plots

are not provided). Similar to $\lambda/L = 0.6$ and $\lambda/L = 1.1$, a phase difference ≈ 180 *deg* is observed in the surge motion responses in CFD versus both EFD data in Figure 5.53c, however, a good agreement is seen for the 1st harmonic amplitude of surge.

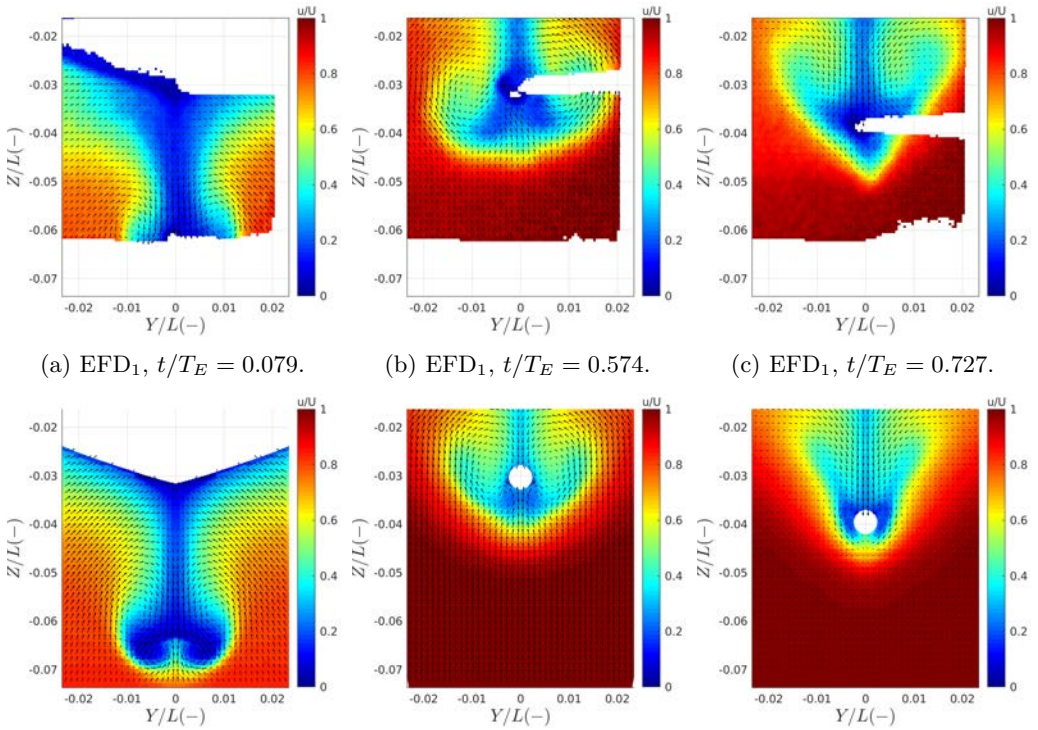

(a) EFD_1, $t/T_E = 0.079$. (b) EFD_1, $t/T_E = 0.574$. (c) EFD_1, $t/T_E = 0.727$.

(d) $n = 1.00$, $t/T_E = 0.078$. (e) $n = 1.00$, $t/T_E = 0.573$. (f) $n = 1.00$, $t/T_E = 0.726$.

Figure 5.55: EFD_1 and CFD wake comparison in the carriage-fixed plane at the initial position of propeller plane in $\lambda/L = 1.6$ at $t/T_E \approx 0.079$, 0.574 and 0.727.

The EFD and CFD heave motion time series in Figure 5.53d are comparable except for EFD_1 which is $\approx 10 - 20$ *deg* out of phase in comparison to CFD and EFD_2 data which is discussed under the results of $\lambda/L = 0.6$. On the other hand, as was seen before, the pitch motion 1st harmonic amplitude in CFD is over-predicted in comparison to both EFD data sets, see Figure 5.53e. Moreover, there is a negative mean pitch in EFD_2. Furthermore, the resistance time series as well as the surface averaged wake velocities on the propeller disc for the last T_E and the reconstructed time series are rather similar in Figures 5.53f and 5.54.

The CFD and EFD wake comparisons shown in Figures 5.55 and 5.56. The SPIV measurements in $\lambda/L = 1.6$ is carried out in both EFD_1 (in the carriage-fixed plane at the initial position of propeller plane) and EFD_2 (in the carriage-fixed plane at the initial position of aft perpendicular). Based on the mentioned potential sources of discrepancies, a qualitative wake comparison is carried out between EFD and CFD and only for a few

selective instances of time t/T_E.

The wake difference between EFD and CFD under the hub due to the symmetry boundary conditions in the CFD simulations is observed, similar to $\lambda/L = 0.6$ and 1.1. The surge value for the grid $n = 1.00$ at $t/T_E = 0.078$ is rather large positive value, and since the plane is fixed on the carriage, the hull is located further in front of the the plane at this instance of time and thus the hub does not penetrate the plane, as seen in Figure 5.55d. On the other hand, this is not the case for time instances $t/T_E = 0.573$ and 0.726 in Figures 5.55e and 5.55f, see the instantaneous surge value in Figure 5.53c for the last T_E in which the CFD wake is extracted from the simulations.

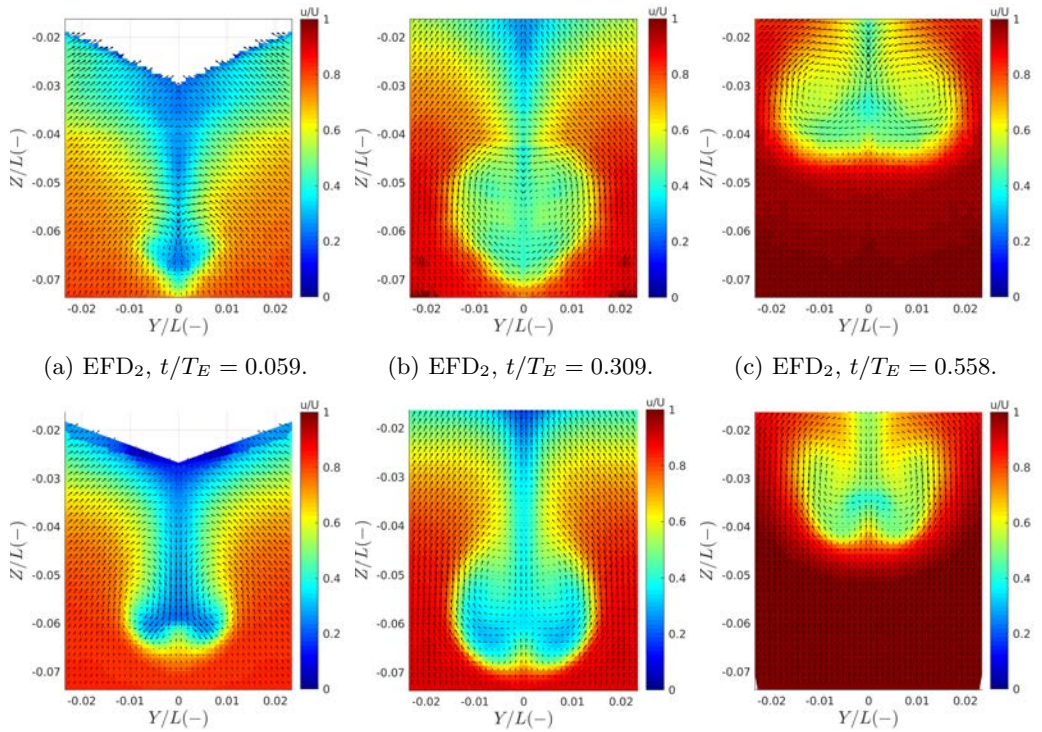

(a) EFD$_2$, $t/T_E = 0.059$. (b) EFD$_2$, $t/T_E = 0.309$. (c) EFD$_2$, $t/T_E = 0.558$.

(d) $n = 1.00$, $t/T_E = 0.059$. (e) $n = 1.00$, $t/T_E = 0.308$. (f) $n = 1.00$, $t/T_E = 0.558$.

Figure 5.56: EFD$_2$ and CFD wake comparison in the carriage-fixed plane at the initial position of aft perpendicular in $\lambda/L = 1.6$ at $t/T_E \approx 0.059$, 0.309 and 0.558.

5.8 Analyses and Discussions

In Sections 5.6 and 5.7, the verification and validation analysis is performed for the hull performance simulations in calm water and regular head waves. In this section, the ship performance in these conditions is analyzed. To this end, the results of free surge simulations (3DOF) in calm water and three regular head waves only in the grid $n = 1.00$ is studied. The reconstructed time series as well as the synced last T_E time series in the simulations in regular head waves (all three studied wave lengths) are combined with the calm water simulations results and shown in Figures 5.57, 5.58 and 5.59.

As it was seen before, the wave elevation at the ship fore perpendicular, shown in Figure 5.57a, is well predicted in the CFD simulations. It should be reminded the wave elevation is recorded at the wave probe Y_1 in the longitudinal location X_1, and then offsetted in time based on the theoretical 5th order Stokes wave mean velocity and ship velocity in order to represent the wave elevation at the initial position of the ship fore perpendicular. Based on the wave propagation simulations provided in Section 5.5, there is a potential discrepancy in comparison to the theoretical wave due to the local refinement zones and overset interpolations. However, such discrepancies are deemed insignificant as the wave propagation studies are carried out for the steepest wave $\lambda/L = 0.6$ and the observed discrepancies are mainly remain lower than 3%.

The instantaneous ship velocity in the CFD simulations are shown in Figure 5.57b. Although the variation of the ship velocity during one encounter period is significant, especially for the longest wave $\lambda/L = 1.6$, the averaged values over such period are rather close to the design speed $U = 0.797\ m/s$ which is also seen in calm water simulations.

The last T_E time series, given in Figure 5.57c, shows that the x_1 is relatively larger in $\lambda/L = 1.6$ compared to the other waves. Since the wake investigations in this section mainly concerns the hull-fixed propeller disc, such surge motion differences may not have a large contribution in the analysis of physical phenomenon related to the wake at propeller plane. On the other hand, the heave and pitch motions 1st harmonic amplitudes in $\lambda/L = 1.1$ and 1.6 are relatively large which may have significant effects on the ship nominal wake. The 1st harmonic phase difference between heave and pitch motions $z_{\varepsilon 1} - \theta_{\varepsilon 1}$ in $\lambda/L = 0.6$, 1.1 and 1.6 are 84, 114 and 120 deg, respectively.

As can be seen in Figure 5.57f, higher harmonics of resistance play a crucial role in the resistance time series. It is seen that the mean of total resistance in $\lambda/L = 1.1$ is larger than the other two waves. Based on this figure, it can be seen that the behavior of the R_T is relatively similar for all three waves considering the time t/T_E. Although the departure of the transient total resistance in $\lambda/L = 1.1$ from its time averaged value is smaller in comparison to the shorter and longer wave lengths, but its mean value is the largest. Actually, this is due to the higher harmonics effects on the total resistance in the vicinity of $t/T_E \approx 0.5$ causing a smaller decrease in resistance in comparison to $\lambda/L = 0.6$ and $\lambda/L = 1.6$, thus resulting in larger mean value. Interestingly, this means that although the propeller of a self-propelled hull in $\lambda/L = 1.1$ has to deliver a larger averaged thrust in comparison to the other wave lengths, but the load variation and consequently the maximum and minimum loading conditions on the propeller will be more severe in the shorter and longer wave lengths. Such a load variation can impose several design constrains both for the propeller and also the machinery system.

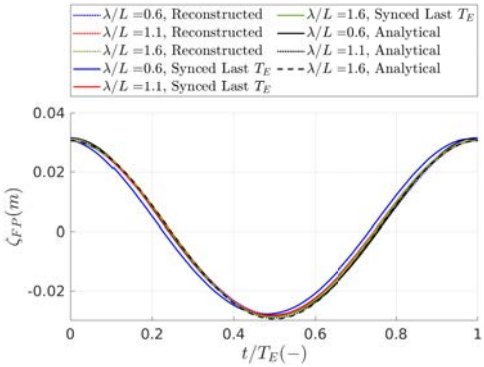

(a) Reconstructed CFD up to 5th HCs.

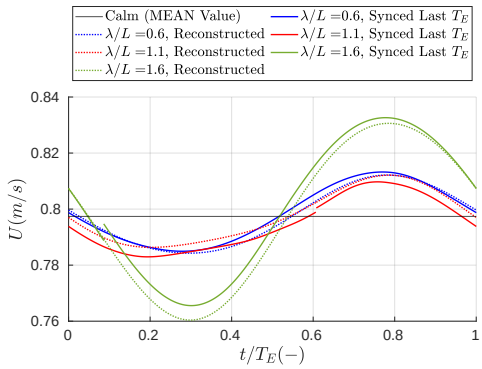

(b) Reconstructed CFD up to 2nd HCs.

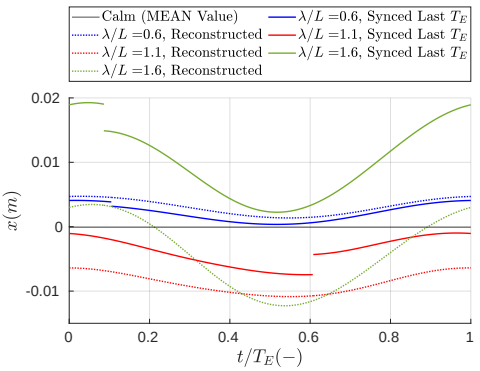

(c) Reconstructed CFD up to 2nd HCs.

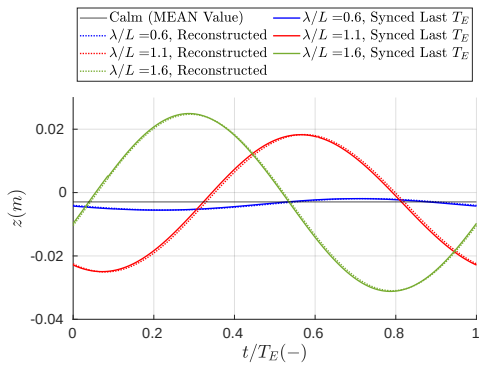

(d) Reconstructed CFD up to 2nd HCs.

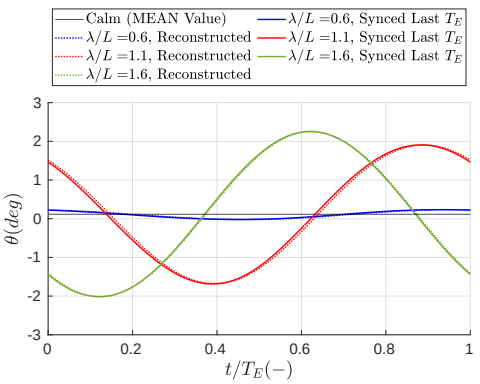

(e) Reconstructed CFD up to 2nd HCs.

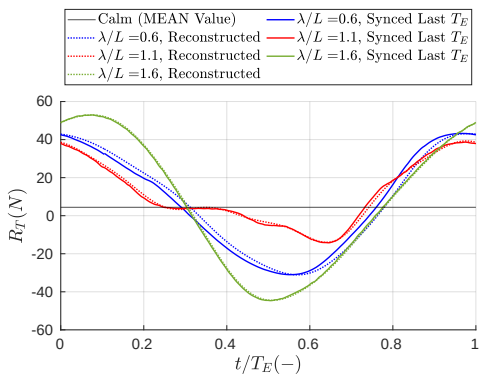

(f) Reconstructed CFD up to 5th HCs.

Figure 5.57: Calm water CFD results against the reconstructed and synced last T_E time series of (a) wave elevation at fore perpendicular, (b) actual ship velocity, (c) surge, (d) heave, (e) pitch and (f) total resistance in regular head waves in grid $n = 1.00$.

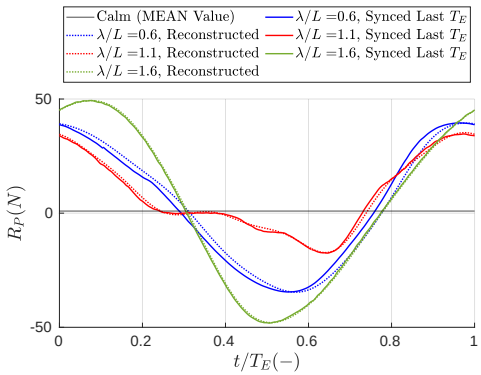

(a) Reconstructed CFD up to 5th HCs.

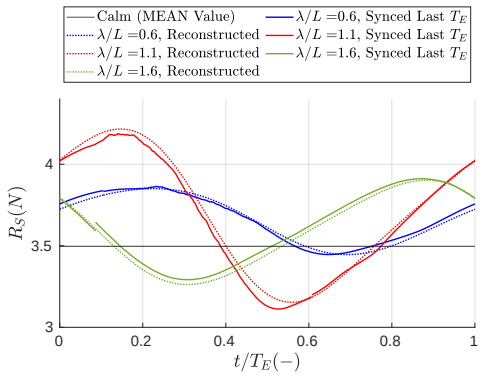

(b) Reconstructed CFD up to 2nd HCs.

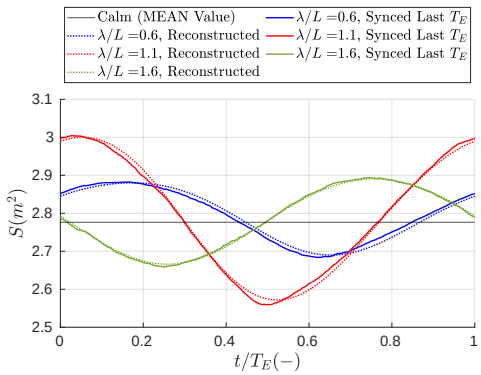

(c) Reconstructed CFD up to 2nd HCs.

Figure 5.58: Calm water CFD results against the reconstructed and synced last T_E time series of (a) pressure resistance component, (b) shear resistance component and (c) wetted surface area of the ship in regular head waves in grid $n = 1.00$.

In order to investigate the reasons behind the smaller variations in the transient total resistance in $\lambda/L = 1.1$, the resistance components, i.e., pressure resistance and shear resistance are extracted and shown in Figures 5.58a and 5.58b, respectively. As expected, the pressure resistance is the dominant resistance component in comparison to the shear resistance component for the simulations at this speed, hence the trend of total resistance mainly follows the pressure resistance component trend.

The wetted surface area of the ship is shown in Figure 5.58c. It can be seen that the shear resistance component and the wetted surface area have similar trends. One of the questions remaining from chapter 4 was to study the deviation of mean shear resistance in regular head wave from that of calm water. In the simulations carried out in this Chapter, this question can be answered. The MEAN shear resistance in calm water (3DOF) for grids $n = 0.75$ to $n = 2.00$ are 3.55, 3.49, 3.44, 3.41 and 3.36 N, respectively. For the

simulations in $\lambda/L = 0.6$, the MEAN shear resistance in the chosen time window $15T_E$, for the same grids are 3.63, 3.66, 3.59, 3.54 and 3.49 N, which are all higher than the respective calm water values. In $\lambda/L = 1.1$ and in the chosen time window $10T_E$ for the same grids the MEAN shear resistance is 3.68, 3.69, 3.63, 3.58 and 3.54 N, which are all higher than both calm water as well as $\lambda/L = 0.6$. However, in $\lambda/L = 1.6$ and in the chosen time window $8T_E$ for the grid $n = 1.00$ it is 3.58 N, which is higher than calm water but lower than $\lambda/L = 0.6$ and 1.1 for the respective grid $n = 1.00$. It should be noted that although the shear resistance component in different waves slightly deviates from the calm water value, the magnitude of the differences are negligible in comparison to the magnitude of total resistance.

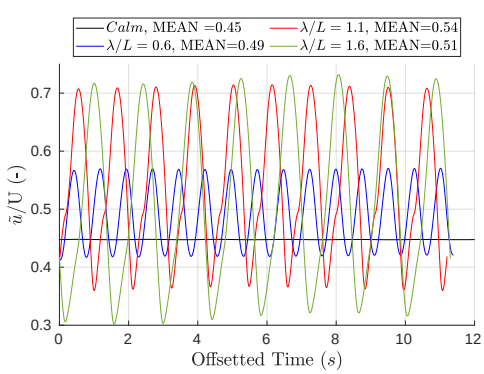

(a) Axial velocity at the propeller disc.

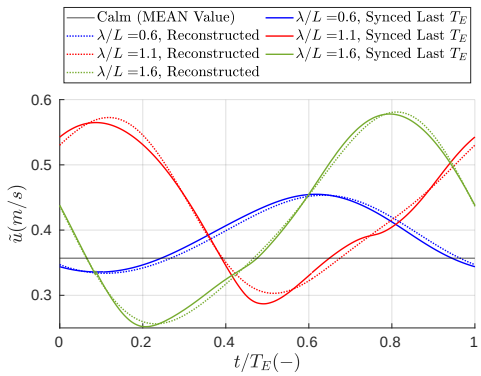

(b) Reconstructed CFD up to 2nd HCs.

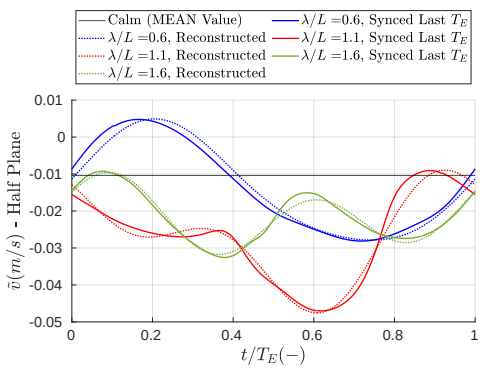

(c) Reconstructed CFD up to 2nd HCs.

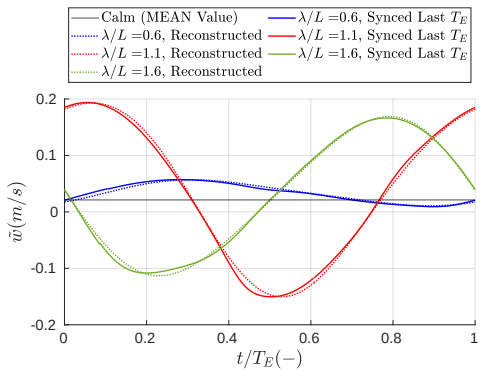

(d) Reconstructed CFD up to 2nd HCs.

Figure 5.59: Comparison of CFD results for (a) time series of the surface-averaged axial velocity component on the hull-fixed propeller disc in the chosen time window in each operational condition as well as the reconstructed and synced last T_E time series of (b) axial velocity component, (c) tangential Y velocity component and (d) tangential Z velocity component in regular head waves in grid $n = 1.00$

In Figure 5.59, the nominal wake at the hull-fixed propeller disc is shown in calm water and regular head waves. In Figure 5.59a, the CFD simulations time series of non-dimensional axial velocity is shown over a time window in calm water and regular head waves. It can be seen that the chosen time windows in the three wave lengths are relatively similar, and also close to the spring natural period $T_{Spring} \approx 11.25$. In the plot legend, the MEAN value of each case is computed on the chosen time window. The mean values of non-dimensional axial velocity in all three waves are larger than calm water value. Although the 1st harmonic amplitude of $\tilde{u}/U$ is larger for the longest wave $\lambda/L = 1.6$, the MEAN value in $\lambda/L = 1.1$ is larger.

In Figures 5.59b, 5.59c and 5.59d, the reconstructed and synced last T_E time series of three surface averaged velocity components on the propeller disk are shown. Although the time origin ($t/T_E = 0$) in all three wave lengths represents the time in which the wave crest is at the initial position of the ship fore perpendicular, the trend of velocity components during time is different. In $\lambda/L = 0.6$, the 1st harmonic amplitude of axial velocity component $\tilde{u}$ is the dominating component and it is relatively lower than the other two wave lengths, hence the wake is closer to the calm water wake. The maximum of $\tilde{u}$ in $\lambda/L = 0.6$ occurs at $t/T_E \approx 0.6$ in which the pitch motion value is close to its minimum and increasing (i.e., when the aft ship submergence is close to its maximum and the stern moves upwards) and the heave is increasing towards its maximum value.

On the other hand, $\tilde{u}$ in $\lambda/L = 1.1$ and 1.6 is affected by the higher harmonics. The maximum of $\tilde{u}$ in $\lambda/L = 1.1$ occurs at $t/T_E \approx 0.1$ in which the heave is approximately at it minimum and the pitch decreases (i.e., stern moving downwards). The minimum of $\tilde{u}$ in $\lambda/L = 1.1$ occurs at $t/T_E \approx 0.5$ in which pitch increases from its minimum value towards positive values (i.e., stern is moving upwards from approximately its highest submergence) but the heave increases and moves towards its maximum value.

The maximum of $\tilde{u}$ in $\lambda/L = 1.6$ occurs at $t/T_E \approx 0.8$ in which heave motion is approximately at its minimum and the pitch motion departs from approximately its maximum values and stern moves downwards. The minimum of $\tilde{u}$ in $\lambda/L = 1.6$ occurs at $t/T_E \approx 0.2$ in which pitch just departs its minimum (stern moves upwards from its mostly submerged condition) and heave motion approaches towards its maximum value.

The surface averaged Z velocity component at the propeller plane, $\tilde{w}$, is approximately 180 *deg* out of phase relative to the heave motion in all λ/L. The surface averaged Y velocity component, $\tilde{v}$, is much smaller than the $\tilde{u}$ and $\tilde{w}$ in terms of magnitude. The higher harmonics of $\tilde{w}$ are insignificant. However, the higher harmonics are playing more important role in the behavior of the tangential velocity Y component $\tilde{v}$, especially in the longer waves.

The nominal wake velocity components on the propeller disc are monitored over the disc for one encountered period of response (in all three considered regular head waves only for the grid $n = 1.00$) and then averaged over the time T_E in each wave. Then the calm water nominal wake on the propeller disc (only for the last time step shown in Figure 5.28) is subtracted from such time-averaged contour plots in waves, see Figure 5.60. In general, the nominal wake is a resultant of boundary layer development along the hull. In waves, due to the hull motions and the dynamics of the flow, the boundary layer development and also the formation of the bilge vortices are different than those of calm water.

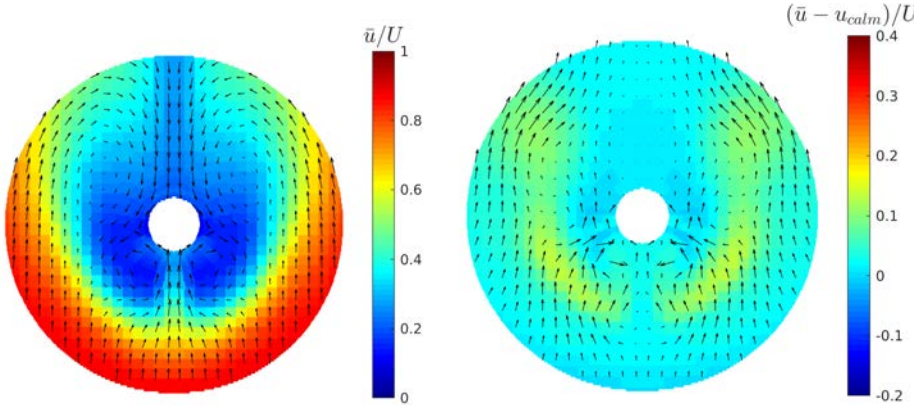

(a) $\lambda/L = 0.6$, averaged over T_E.

(b) $\lambda/L = 0.6$, $\bar{u}$ minus calm.

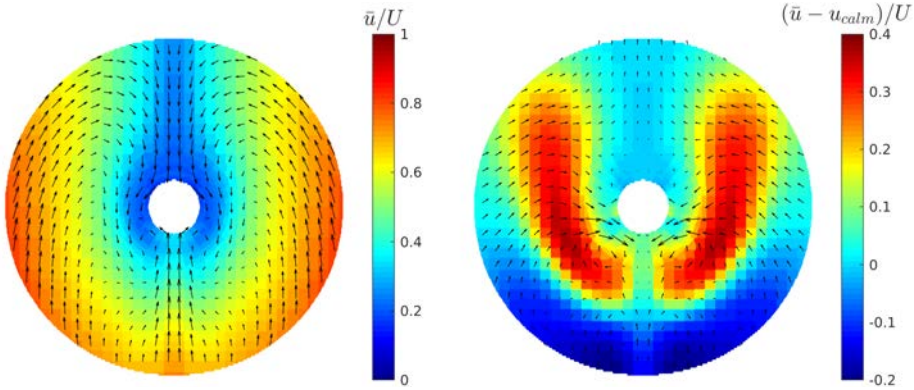

(c) $\lambda/L = 1.1$, averaged over T_E.

(d) $\lambda/L = 1.1$, $\bar{u}$ minus calm.

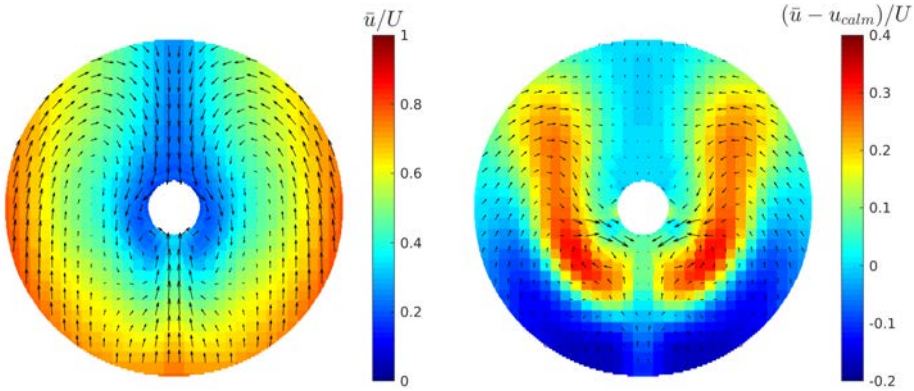

(e) $\lambda/L = 1.6$, averaged over T_E.

(f) $\lambda/L = 1.6$, $\bar{u}$ minus calm.

Figure 5.60: Averaged (over one encounter period T_E) CFD wake on hull-fixed propeller disc for regular head waves simulations as well as the same averaged wake mines calm water wake at the last time step in free surge calm water simulations, all for grid $n = 1.00$.

As presented earlier, the wake becomes fuller in waves in comparison to calm water (also seen in Figure 5.60). The time averaged nominal wake distribution in $\lambda/L = 0.6$ is the closest to the calm water nominal wake, simply because the wave induced motions are the smallest in this wave relative to the other studies waves. However, in the higher wave lengths, the motions increase significantly which in turn alter the formation of the boundary layer and bilge vortex dynamics. In general, bilge vortex tends to move low-speed flow from the inner side of the boundary layer outward, and inward further up. This creates a hook shape in the velocity contour at the propeller plane. The bilge vortex is less dynamic in calm water relative to waves. As a result it stays within a certain range close to the hull. Therefore, in a certain time interval, its effect is concentrated in a limited region. However, the bilge vortex continuously moves up and down in waves, and sometimes even moves out of the propeller plane. As a result, the interaction effect of the bilge vortex and the boundary layer will be less concentrated and thus its capability of moving the low speed flow close to the propeller plane center will be weakened. This results in a fuller nominal wake in waves relative to calm water. Here, the motions in $\lambda/L = 1.1$ are the severest and thus the nominal wake is the fullest. The contour plots of the time averaged wake difference between the waves and the calm water conditions show the regions with velocity deficit and excess in waves relative to calm water. Since a propeller is often designed based on the calm water nominal wake, any deviation from the calm water wake alters the loading distribution on the blade resulting in an adverse effect on the propeller performance.

The circumferentially averaged axial velocity component of the nominal wake in regular waves is compared to that of the calm water (last time step) in Figure 5.61. The curves shown in this plot represents the average flow which each propeller blade section encounters in one full revolution. The radial distribution of the axial component in $\lambda/L = 0.6$ is rather similar to that of calm water, however, in $\lambda/L = 1.1$ and 1.6 the radial distribution of the axial velocity is considerably different than the calm water curve, approximately between $0.282 < r/R < 0.7$.

The variation of the circumferentially averaged axial velocity on the propeller disc in one encounter wave period is also shown in Figures 5.61b, 5.61c and 5.61d for $\lambda/L = 0.6$, 1.1 and 1.6, respectively. These contour plots indicate that the wake significantly varies in time, especially in $\lambda/L = 1.1$ and 1.6 where the motions are larger. This means that the propeller loading while operating in this wake will change significantly in each time incident during one encounter period. However, it should be kept in mind that a circumferentially time averaged wake is a more relevant way of extracting the nominal wake for designing a wake adapted propeller blade for each wave length. Nevertheless, it should not be forgotten that the transient wake and thus propeller load variation in one encounter period should also be studied to avoid any design failure in any of the circumferentially transient nominal wake distributions.

As the final step of the evaluation of the presented RANS method for hull performance in waves, the computational costs in terms of *Core-Hours* for the simulations in calm water and regular head waves are shown in Figure 5.62. The computational costs of simulations in free and fixed calm water simulations for the same grid are very similar as shown in Figure 5.62a in which the computational costs are represented per 1 s of physical time simulation. On the other hand, the computational costs for simulations in regular

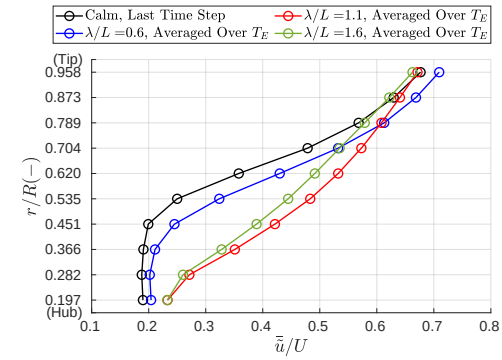

(a) Time averaged axial velocity.

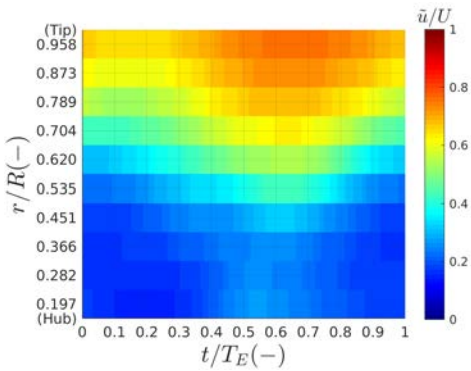

(b) $\lambda/L = 0.6$.

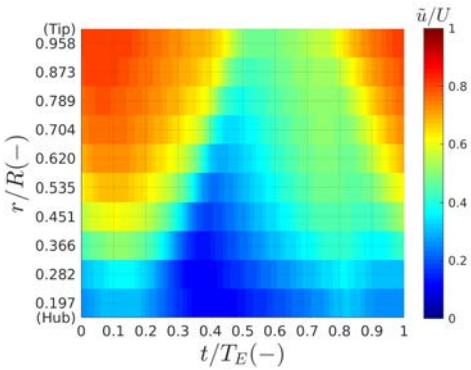

(c) $\lambda/L = 1.1$.

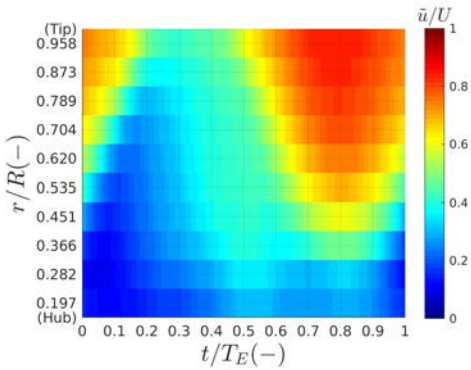

(d) $\lambda/L = 1.6$.

Figure 5.61: Circumferentially averaged axial wake on the hull-fixed propeller disc in calm water and regular head waves, all for grid $n = 1.00$.

head waves in terms of *Core-Hours* per encountered wave period in each wave length are shown in Figure 5.62b. Longer T_E in longer wave lengths means longer physical time of simulation, and hence higher computational costs. One important point is that the computational costs in calm water and regular head waves in terms of the simulation of 1 s physical time for the same grid are almost similar, because the same models and grid disretization (i.e., GS5) are used for the simulation of these two conditions.

For different simulations, different computing resources (clusters) with different types of equipment are used, hence there exist an inconsistency (bias) in the direct comparison of the computational costs in different operational conditions. However, for an overall comparison, the computational costs shown in Figure 5.62 can still be useful. For parallel computations, approximately between 50000 to 90000 cells are allocated to each core in different simulations, except for the grid $n = 1.00$ in $\lambda/L = 0.6$ where less number of cells (≈ 30000) are allocated to each core. It can be seen that the efficiency of such computations are dropped which is resulted in higher computational costs.

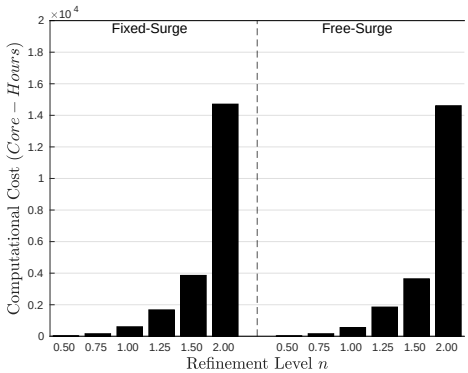

(a) Computational costs for 1 s of physical time calm water simulation.

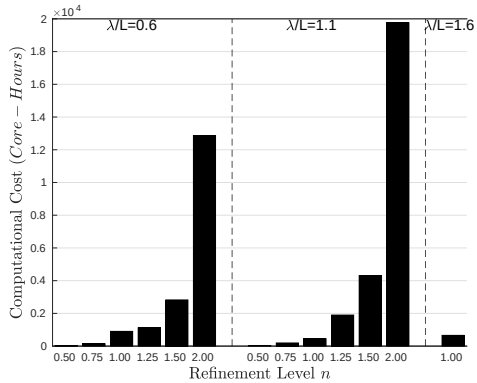

(b) Computational costs for 1 encountered wave (T_E) of regular head wave simulation.

Figure 5.62: Computational costs of hull performance simulation in calm water and regular head waves.

5.9 Conclusions

In this chapter, the hydrodynamic performance of a tanker ship (KVLCC2) was investigated using a viscous flow solver in terms of resistance and motions responses as well as nominal wake in calm water and regular head waves. The hull performance simulations were carried out in four operational conditions at the design speed and in the design loading condition; one in calm water and three in regular head waves with the same wave height and three different wave lengths $\lambda/L = 0.6$, 1.1 and 1.6. In addition, a formal verification and validation (V&V) procedure is applied to understand and control the numerical and modeling errors in the RANS computations. The verification analysis in this chapter concerned the grid convergence study using the method developed by Eça and Hoekstra (2014) based on Least Square curve fitting. The experimental model tests (EFD) were carried out in Osaka University Towing Tank mainly in free surge conditions using a very weak spring system. An external force F_0 is applied in each operational condition to restrict large stretch of the spring.

The CFD wake at different locations are compared to that of experimental SPIV measurements. However, there are several potential sources of discrepancy between CFD and EFD data. EFD wake measurements are carried out on two planes which were fixed on the carriage. Since F_0 was not known from the experiments, a guessed value was used in the CFD simulations. However, the difference between such external force could have had affected the spring behavior resulting in an inconsistency of surge motion between CFD and EFD. As the plane of wake measurements were carriage-fixed, difference in surge would affect the longitudinal position of the plane with respects to the hull, hence introducing a source of discrepancy in the wake comparison. Another potential source of discrepancy was the exact time instances of SPIV measurements in regular head waves as different setups were used to trigger the EFD wake measurements. Based on the analysis

performed in this chapter, such setups could significantly affect the time instances for wake measurements. On the other hand, the measured wave height in EFD data in some operational conditions were different from the target value, therefore, the response of the ship could have been affected, hence this can also be counted as an extra source of discrepancy.

The hull performance simulations were carried out in one grid set but up to six "as geometrically similar as possible" unstructured grids. The calm water simulations included the hull performance in both free and fixed surge conditions in all six grids. The grid convergence study for the calm water resistance and the axial velocity component of the nominal wake on the propeller disc showed relatively large numerical uncertainties. However, it was suggested that since the computed values in different grids were similar, a linear curve fitting could have been a more practical alternative than the second order method in the employed verification tool. The computed resistance and motions in calm water were in a rather good agreement with the measured data and the results of fixed and free surge were similar. Although the wake in calm water simulations were unsteady and shedding, only the last time step of each simulation is used for wake comparison. The reason was that such effects were insignificant in terms of the concerned objectives, i.e., to compare wake in rather stationary calm water simulations to that of highly dynamic regular head waves. Concerning the aforementioned potential sources of discrepancy, the CFD wake resembles well to the EFD SPIV measurements.

In order to examine the quality of numerical wave propagation in the CFD simulations, a broad range of wave propagation simulations in the steepest (most critical) wave was carried out using different geometrically similar unstructured grid sets. In these simulations the effects of refinement levels between the grids in each grid set were studied. Moreover, the effects of different local refinement zones and overset interpolation quality on the numerical wave propagation were investigated. It was found that the numerical wave was rather comparable to the theoretical one and the discrepancies remained mainly under 3% for different grids, except the coarsest grid. The coarsest grid was incapable of capturing the main flow features and hence the results of such grid were drastically off from the other girds and most probably not in the asymptotic range. Therefore, such result were not included in verification and validation analyses in the hull performance simulations.

The same grid set was used for the hull performance simulations in calm water and regular head waves. All six considered grid refinements were used for the simulations in $\lambda/L = 0.6$ and 1.1 and the grid convergence was carried out in these waves. However, only one grid was used for the simulations in $\lambda/L = 1.6$. The numerical uncertainties for the 1st harmonic amplitudes of motions were relatively lower than the mean resistance, except for the cases where the motions magnitudes are small and hence large uncertainties were calculated. The numerical uncertainties of the axial velocity of wake were relatively higher than resistance. However, similar to the calm water grid convergence study, the numerical uncertainties for the cases in which all grids have similar values can be predicted by a linear curve fitting approximation. The overall results of the hull performance simulations in regular head waves were in a good agreement with the experimental data, both for ship responses and its wake considering the aforementioned potential sources of discrepancy. An extensive wake study was also carried out for the simulations in waves and some general

conclusions are made, however, more analysis needed to derive a better understanding of the ship nominal wake and the effects of different hydrodynamic responses on the wake. For instance, it was seen that the bilge vortex shedding from the ship hull body moved relative to the ship motions. Therefore, pulsation of the hull vertices especially due to waves orbital velocities and ship motions passade into the nominal wake resulting in a significant change of propeller loading in comparison to calm water condition.

The general results are promising compared with the experimental measurements, as the current RANS method predicts the hydrodynamic responses and nominal wake and the corresponding trends qualitatively well. The uncertainty of the EFD data should not be overlooked. The flow field analyzes further provide valuable insight into the hull wave interaction effects and help the understanding of the mechanism of those effects. Although the finer grids mainly showed better results, the computational costs for such grids were rather high and the choice of refinement level highly depends on the available computing resources. The investigations carried out in this chapter are still ongoing and more analysis should be performed on the derived data.

6

Concluding Remarks and Future Work

In this thesis, the bare hull hydrodynamic performance is studied in calm water and regular head waves. A Fully Nonlinear Potential Flow method (FNPF) as well as a viscous flow method using a Reynolds-Averaged Navier-Stokes approach (RANS) are employed. Detailed information about the usage and computational results of these methods are given in Chapters 4 and 5, and detailed conclusions are given respectively in each chapter. The investigations in these methods include an extensive comparison of the results with the available experimental data. Moreover, a grid convergence study is performed on several quantities derived from the RANS method.

The overall results are in good agreement with the experimental measurements in both methods and the hull hydrodynamic performance is well predicted. Each method has its pros and cons which are fully explained under the respective chapters. Although the FNPF method predicts the ship hydrodynamic responses with a rather high accuracy, it is not capable of providing an insight into the viscous related phenomena in ship hydrodynamics. Moreover, the accuracy of the predicted resistance in the FNPF method is lower than that of ship motions. On the other hand, the viscous phenomena in ship hydrodynamics context can be investigated to some extent using RANS-type methods with the penalty of increased computational costs in comparison to the FNPF methods. As a general recommendation, FNPF is deemed sufficiently accurate for predicting the hull motions and to some extent the resistance. It is shown that the shear forces do not deviate much from the calm water values. Thus, the ITTC frictional line or other similar empirical methods can be used together with the FNPF methods for prediction of the frictional resistance of the hull. If, beside the hull motions and resistance, the wake of the hull is of interest, RANS-type methods have the capability to predict the complicated dynamics of the viscous wake and thus recommended.

The long-tern objective of this research is to study the propeller-hull interaction effects in calm water and regular head waves. In this thesis, extensive investigations are carried out to study the ship bare hull performance in those operational conditions. Although the simulations are completed, there still some room for further analysis of RANS simulations results which will be carried out in the near future. The effects of symmetry boundary conditions is also planned to be studied by running a simulation in full domain and comparing the results with that of symmetry boundary condition.

Then the next step concerns inclusion of propeller into the numerical investigations. To this end, it is planned to study the propeller open water characteristics in waves and compare those to the calm water conditions. A series of model tests have already been carried out and soon the numerical simulations will be performed. The analysis of the flow field will provide interesting information about the propeller-wave interactions.

Finally, the self-propulsion simulations are planned to be performed. The propeller-hull interaction effect in calm water and regular head waves will be analyzed through the study of the propulsive factors and the correlated uncertainties.

References

Berndt, J. C., R. Perić, and M. Abdel-Maksoud (2021). Improved Simulation of Flows with Free-Surface Waves by Optimizing the Angle Factor in the HRIC Interface-Sharpening Scheme. *Journal of Applied Fluid Mechanics* **14**.3, 909–920. ISSN: 1735-3572. DOI: 10.47176/jafm.14.03.32062.

Bertram, Volker (2012). *Practical Ship Hydrodynamics*. Second. Oxford: Butterworth-Heinemann.

Bertram, Volker (2016). "Added power in waves - Time to stop lying (to ourselves)". *Proceedings of the 1st Hull Performance & Insight Conference (HuLLPIC)*. Pavone, pp. 5–13.

Bhattacharyya, Anirban and Sverre Steen (2014). Propulsive factors in waves: A comparative experimental study for an open and a ducted propeller. *Ocean Engineering* **91**, 263–272. ISSN: 0029-8018. DOI: 10.1016/j.oceaneng.2014.09.020.

Bhattacharyya, Rameswar (1978). *Dynamics of Marine Vehicles*. A Wiley-Interscience publication. Wiley.

Block, Jan Jacobus (1993). "The resistance increase of a ship in waves." PhD thesis. Delft University of Technology.

Boese, Peter (1970). *Eine einfache Methode zur Berechnung der Widerstandserhföhung eines Schiffes im Seegang*. Tech. rep. (in German). institut für schiffbau der universitfät hamburg. DOI: 10.15480/882.648.

Coslovich, Francesco, Martin Kjellberg, Magnus Östberg, and Carl-Erik Janson (2021). Added resistance, heave and pitch for the KVLCC2 tanker using a fully nonlinear unsteady potential flow boundary element method. *Ocean Engineering* **229**, 108935. ISSN: 0029-8018. DOI: 10.1016/j.oceaneng.2021.108935.

Crepier, P. (2017). "Ship resistance prediction: verification and validation exercise on unstructured grids". *MARINE VII : proceedings of the VII International Conference on Computational Methods in Marine Engineering*. CIMNE, 365–376. ISBN: 978-84-946909-8-3.

Ducrozet, G., H. B. Bingham, A. P. Engsig-Karup, and P. Ferrant (2010). High-order finite difference solution for 3D nonlinear wave-structure interaction. *Journal of Hydrodynamics* **22**.5, 225–230. DOI: 10.1016/S1001-6058(09)60198-0.

Engsig-Karup, A. P., H. B. Bingham, and O. Lindberg (2009). An efficient flexible-order model for 3D nonlinear water waves. *Journal of Computational Physics* **228**.6, 2100–2118. ISSN: 0021-9991. DOI: 10.1016/j.jcp.2008.11.028.

Eça, L. and M. Hoekstra (2009). Evaluation of numerical error estimation based on grid refinement studies with the method of the manufactured solutions. *Computers & Fluids* **38**.8, 1580–1591. ISSN: 0045-7930. DOI: https://doi.org/10.1016/j.compfluid.2009.01.003.

Eça, L. and M. Hoekstra (2014). A procedure for the estimation of the numerical uncertainty of CFD calculations based on grid refinement studies. *Journal of Computational Physics* **262**, 104–130. ISSN: 0021-9991. DOI: https://doi.org/10.1016/j.jcp.2014.01.006.

Eça, L., G. Vaz, S. L. Toxopeus, and M. Hoekstra (July 2019). Numerical Errors in Unsteady Flow Simulations. *Journal of Verification, Validation and Uncertainty Quantification* **4**.2. 021001. ISSN: 2377-2158. DOI: 10.1115/1.4043975.

Eça, Luís, Guilherme Vaz, and M Hoekstra (Jan. 2010). "A Verification and Validation Exercise for the Flow Over a Backward Facing Step", pp. 14–17.

Faltinsen, Odd M. (1990). *Sea loads on ships and offshore structures.* Cambridge Ocean Technology Series. Campridge, UK: Cambridge University Press. ISBN: 9780521458702.

Faltinsen, Odd M., Knut J. Minsaas, Nicolas Liapis, and Svein O. Skjørdal (1980). "Prediction of resistance and propulsion of a ship in a seaway." *Proceedings of the 13th Symposium on Naval Hydrodynamics.* Tokyo, pp. 505–529.

Fenton, J.D. (1985). A fifth-order stokes theory for steady waves. *Journal of Waterway, Port, Coastal and Ocean Engineering* **111**.2, 216–234. DOI: 10.1061/(ASCE)0733-950X(1985)111:2(216).

Gerritsma, J. and W. Beukelman (1972). Analysis of the resistance increase in waves of a fast cargo ship. *International Shipbuilding Progress.* **19**.217, 285–293. ISSN: 0020868X. DOI: 10.3233/isp-1972-1921701.

Gerritsma, J., J.J. van den Bosch, and W. Beukelman (1961). Propulsion in regular and irregular waves. *International Shipbuilding Progress* **8**.82, 235–247. DOI: 10.3233/ISP-1961-88201.

Guo, B.J., S. Steen, and G.B. Deng (2012). Seakeeping prediction of KVLCC2 in head waves with RANS. *Applied Ocean Research* **35**, 56–67. ISSN: 0141-1187. DOI: 10.1016/j.apor.2011.12.003.

Havelock, Thomas Henry (1937). The resistance of a ship among waves. *Proceedings of the Royal Society of London. Series A - Mathematical and Physical Sciences.* **161**.906, 299–308. DOI: 10.1098/rspa.1937.0147.

Havelock, Thomas Henry (1942). XLVII. The drifting force on a ship among waves. *The London, Edinburgh, and Dublin Philosophical Magazine and Journal of Science.* 7th ser. **33**.221, 467–475. DOI: 10.1080/14786444208521213.

Hayashi, Y. (2012). "Phase-averaged 3DPIV flow field measurement for KVLCC2 model in waves". (in Japanese). MA thesis. Osaka University, Japan.

Hino, Takanori, Frederick Stern, Lars Larsson, Michel Visonneau, Nobuyuki Hirata, and Jin Kim, eds. (2021). *Numerical Ship Hydrodynamics - An Assessment of the Tokyo 2015 Workshop.* Springer. DOI: 10.1007/978-3-030-47572-7.

Hirdaris, S. E., Y. Lee, G. Mortola, A. Incecik, O. Turan, S. Y. Hong, B. W. Kim, K. H. Kim, S. Bennett, S. H. Miao, and P. Temarel (2016). The influence of nonlinearities on the symmetric hydrodynamic response of a 10,000 TEU Container ship. *Ocean Engineering* **111**, 166–178. ISSN: 0029-8018. DOI: 10.1016/j.oceaneng.2015.10.049.

Hirdaris, S.E., W. Bai, D. Dessi, A. Ergin, X. Gu, O.A. Hermundstad, R. Huijsmans, K. Iijima, U.D. Nielsen, J. Parunov, N. Fonseca, A. Papanikolaou, K. Argyriadis, and A. Incecik (2014). Loads for use in the design of ships and offshore structures. *Ocean Engineering* **78**, 131–174. ISSN: 0029-8018. DOI: 10.1016/j.oceaneng.2013.09.012.

Irannezhad, Mohsen, Rickard E. Bensow, Martin Kjellberg, and Arash Eslamdoost (2021). "Towards uncertainty analysis of CFD simulation of ship responses in regular head waves". *Proceedings of the 23rd Numerical Towing Tank Symposium (NuTTS 2021).*

Irannezhad, Mohsen, Arash Eslamdoost, and Rickard E. Bensow (2019a). "Numerical investigation of a general cargo vessel wake in waves". *Proceedings of the 22nd Numerical Towing Tank Symposium (NuTTS 2019)*.

Irannezhad, Mohsen, Arash Eslamdoost, and Rickard E. Bensow (2019b). "Numerical investigation of a large diameter propeller emergence risk for a vessel in waves". *Proceedings of the 8th International Conference on Computational Methods in Marine Engineering (MARINE 2019)*. Gothenburg, Sweden, pp. 634–645. DOI: 10.5281/zenodo.2650219.

Irannezhad, Mohsen, Arash Eslamdoost, Martin Kjellberg, and Rickard E. Bensow (2022). Investigation of ship responses in regular head waves through a Fully Nonlinear Potential Flow approach. *Ocean Engineering* **246**, 110410. ISSN: 0029-8018. DOI: 10.1016/j.oceaneng.2021.110410.

Irvine, Martin, Joseph Longo, and Frederick Stern (2008). Pitch and heave tests and uncertainty assessment for a surface combatant in regular head waves. *Journal of Ship Research*. ISSN: 00224502.

ITTC (2014). International Towing Tank Conference. Recommended Procedures and Guidelines 7.5-03-02-03, "Practical Guidelines for Ship CFD Applications", 27^{th} ITTC, 2014.

ITTC (2017a). International Towing Tank Conference. Recommended Procedures and Guidelines 7.5-02-03-01.5, "Predicting Powering Margins", 28^{th} ITTC, 2017.

ITTC (2017b). International Towing Tank Conference. Recommended Procedures and Guidelines 7.5-02-07-02.5, "Verification and Validation of Linear and Weakly Nonlinear Seakeeping Compuetr Codes", 28^{th} ITTC, 2017.

ITTC (2018). International Towing Tank Conference. Recommended Procedures and Guidelines 7.5-02-07-02.8, "Calculation of the weather factor f_w for decrease of ship speed in wind and waves", 29^{th} ITTC, 2018.

Joncquez, S. A. G., H. B. Bingham, P. Andersen, and D. Kring (2008). "Validation of Added Resistance Computations by a Potential-Flow Boundary-Element Method". *Proceedings of the 27^{th} Symposium on Naval Hydrodynamics*. Office of Naval Research, U.S.A.

Joosen, W. P. A. (1966). "Added resistance of ships in waves." *Proceedings of the 6^{th} Symposium on Naval Hydrodynamics.* National Academy Press., Washington D.C.,USA, pp. 637–647.

Kim, Ho (2014). "Phase-Averaged SPIV Wake Field Measurement for KVLCC2 Propeller Plane in Waves". PhD thesis. Osaka University, Japan. DOI: 10.18910/50513.

Kim, Mingyu, Olgun Hizir, Osman Turan, Sandy Day, and Atilla Incecik (2017). Estimation of added resistance and ship speed loss in a seaway. *Ocean Engineering* **141**, 465–476. ISSN: 0029-8018. DOI: 10.1016/j.oceaneng.2017.06.051.

Kjellberg, Martin (2013). "Fully non-linear unsteady three-dimensional boundary element method for ship motions in waves". PhD thesis. Chalmers University of Technology.

Larsson, L. and H. C. Raven (2010). *Ship Resistance and Flow.* PNA Series. Jersey City: Society of Naval Architects and Marine Engineers.

Larsson, Lars, Frederik Stern, and Michel Visonneau, eds. (2014). *Numerical Ship Hydrodynamics - An Assessment of the Gothenburg 2010 Workshop*. Springer. DOI: 10.1007/978-94-007-7189-5.

Lee, Cheol-Min, Sung-Chul Park, Jin-Won Yu, Jung-Eun Choi, and Inwon Lee (2019a). Effects of diffraction in regular head waves on added resistance and wake using CFD. *International Journal of Naval Architecture and Ocean Engineering* **11**.2, 736–749. ISSN: 2092-6782. DOI: 10.1016/j.ijnaoe.2019.02.013.

Lee, Cheol-Min, Jin-Hyeok Seo, Jin-Won Yu, Jung-Eun Choi, and Inwon Lee (2019b). Comparative study of prediction methods of power increase and propulsive performances in regular head short waves of KVLCC2 using CFD. *International Journal of Naval Architecture and Ocean Engineering* **11**.2, 883–898. ISSN: 2092-6782. DOI: 10.1016/j.ijnaoe.2019.02.001.

Lee, Jaehoon, Dong-Min Park, and Yonghwan Kim (2017). Experimental investigation on the added resistance of modified KVLCC2 hull forms with different bow shapes. *Proceedings of the Institution of Mechanical Engineers, Part M: Journal of Engineering for the Maritime Environment* **231**.2, 395–410. DOI: 10.1177/1475090216643981.

Lemaire, Sébastien, Guilherme Vaz, Menno Rijswijk, and Stephen Turnock (Sept. 2021). On the Accuracy, Robustness and Performance of High Order Interpolation Schemes for the Overset Method on Unstructured Grids. *International Journal for Numerical Methods in Fluids* **93**, 1–36. DOI: 10.1002/fld.5050.

Lewis, E V (1989). *Principles of naval architecture. 2nd reversion, vol III Motions in waves and controllability.*

Martinsen, Mads Asbjørn (2016). "A design tool for estimating the added wave resistance of container ships". MA thesis. Technical University of Denmark.

Maruo, Hajime (1957). The excess resistance of a ship in rough seas. *International Shipbuilding Progress.* **4, no. 35**, 337–345. DOI: 10.3233/ISP-1957-43501.

Maruo, Hajime (1960). The drift of a body floating on waves. *Journal of Ship Research.* **4**, 1–10.

Menter, F. R. (1994). Two-equation eddy-viscosity turbulence models for engineering applications. *AIAA Journal* **32**.8, 1598–1605. DOI: 10.2514/3.12149.

Mola, A., L. Heltai, and A. De Simone (2017). Wet and dry transom stern treatment for unsteady and nonlinear potential flow model for naval hydrodynamics simulations. *Journal of Ship Research* **61**.1, 1–14. DOI: 10.5957/JOSR.61.1.160016.

Moor, D. I. and D. C. Murdey (1970). Motions and propulsion of single screw models in head seas, Part II. *Transactions of the Royal Institution of Naval Architects* **112**.2.

Muzaferija, S. and M. Peric' (1998). "Computation of free surface flows using interface-tracking and interface-capturing methods". *In: Mahrenholtz O., Markiewicz M. (Eds.) Nonlinear water wave interaction, Computational Mechanics Publications.* Southampton.

Mwangi, Benson Oyunge (2021). "SPIV Flow Field Measurement around the Stern of a Self-propelled KVLCC2 Model Ship in Regular Head Waves". PhD thesis. Osaka University, Japan. DOI: 10.18910/85407.

Nakamura, Shoichi and Shigeru Naito (1975). Propulsive performance of a container ship in waves. *Journal of the Society of Naval Architects of Japan* **15**.158, 24–48.

Newman, J. N. (1967). The drift force and moment on ships in waves. *Journal of Ship Research.* **11**, 51–60.

Pacuraru, Florin, Leonard Domnisoru, and Sandita Pacuraru (2020). On the Comparative Seakeeping Analysis of the Full Scale KCS by Several Hydrodynamic Approaches.

Journal of Marine Science and Engineering **8**.12. ISSN: 2077-1312. DOI: 10.3390/jmse8120962.

Peric', Milovan (2017). Best Practices for Simulations With Waves, *Presentation at STAR Global Conference*, Berlin, Germany.

Perić, Robinson and Moustafa Abdel-Maksoud (2018). Analytical prediction of reflection coefficients for wave absorbing layers in flow simulations of regular free-surface waves. *Ocean Engineering* **147**, 132–147. ISSN: 0029-8018. DOI: https://doi.org/10.1016/j.oceaneng.2017.10.009.

Perić, Robinson and Moustafa Abdel-Maksoud (Mar. 2020). Reducing Undesired Wave Reflection at Domain Boundaries in 3D Finite Volume-Based Flow Simulations via Forcing Zones. *Journal of Ship Research* **64**.01, 23–47. ISSN: 0022-4502. DOI: 10.5957/jsr.2020.64.1.23.

Perić, Robinson, Vuko Vukčević, Moustafa Abdel-Maksoud, and Hrvoje Jasak (2022). Optimizing wave generation and wave damping in 3D-flow simulations with implicit relaxation zones. *Coastal Engineering* **171**, 104035. ISSN: 0378-3839. DOI: https://doi.org/10.1016/j.coastaleng.2021.104035.

Regener, Pelle Bo (2016). "Hull-Propeller Interaction and Its Effect on Propeller Cavitation". PhD thesis. Technical University of Denmark. DOI: 10.11581/DTU:00000032.

Roache, Patrick J. (1998). Verification of Codes and Calculations. *AIAA Journal* **36**.5, 696–702. DOI: 10.2514/2.457.

Sadat-Hosseini, Hamid, Ping-Chen Wu, Pablo Carrica, Ho Kim, Yasuyuki Toda, and Frederick Stern (Feb. 2013). CFD verification and validation of added resistance and motions of KVLCC2 with fixed and free surge in short and long head waves. *Ocean Engineering* **59**, 240–273. DOI: 10.1016/j.oceaneng.2012.12.016.

Salvesen, N. (1974). Second-ORDER STEADY-STATE FORCES AND MOMENTS ON SURFACE SHIPS IN OBLIQUE REGULAR WAVES.

Salvesen, Nils (1978). Added resistance of ships in waves. *Journal of Hydronautics* **12**.1, 24–34. DOI: 10.2514/3.63110.

Salvesen, Nils, E. O. Tuck, and Odd Faltinsen (1970). *Ship motions and sea loads*. DOI: citeulike-article-id:10193407.

Seo, Jin-Hyeok, Cheol-Min Lee, Jin-Won Yu, Jung-Eun Choi, and Inwon Lee (2020). Power increase and propulsive characteristics in regular head waves of KVLCC2 using model tests. *Ocean Engineering* **216**, 108058. ISSN: 0029-8018. DOI: 10.1016/j.oceaneng.2020.108058.

Sigmund, Sebastian (2019). "Performance of ships in waves". PhD thesis. DOI: 10.17185/duepublico/70021.

Simonsen, Claus D., Janne F. Otzen, Soizic Joncquez, and Frederick Stern (2013). EFD and CFD for KCS heaving and pitching in regular head waves. *Journal of Marine Science and Technology (Japan)*. ISSN: 09484280. DOI: 10.1007/s00773-013-0219-0.

Stern, Frederick, Robert Wilson, Hugh Coleman, and Eric Paterson (Dec. 2001). Comprehensive Approach to Verification and Validation of CFD Simulations—Part 1: Methodology and Procedures. *Journal of Fluids Engineering* **123**, 792. DOI: 10.1115/1.1412235.

Taskar, Bhushan, Kevin Koosup Yum, Sverre Steen, and Eilif Pedersen (2016). The effect of waves on engine-propeller dynamics and propulsion performance of ships. *Ocean Engineering* **122**, 262–277. DOI: 10.1016/j.oceaneng.2016.06.034.

Valanto, Petri and YongPyo Hong (2017). "Wave Added Resistance and Propulsive Performance of a Cruise Ship in Waves". *Proceedings of the 27th International Ocean and Polar Engineering Conference*. San Francisco, CA, USA: International Society of Offshore and Polar Engineers (ISOPE), pp. 737–745.

Wu, Ping-Chen (2013). "A CFD Study on Added Resistance, Motions and Phase Averaged Wake Fields of Full Form Ship Model in Head Waves". PhD thesis. Osaka University, Japan. DOI: 10.18910/26191.

Xing, Tao and Frederick Stern (June 2010). Factors of Safety for Richardson Extrapolation. *Journal of Fluids Engineering* **132**.6. 061403. ISSN: 0098-2202. DOI: 10.1115/1.4001771.

Xing, Tao and Frederick Stern (Dec. 2011). Closure to "Discussion of 'Factors of Safety for Richardson Extrapolation'" (2011, ASME J. Fluids Eng., 133, p. 115501). *Journal of Fluids Engineering* **133**.11. 115502. ISSN: 0098-2202. DOI: 10.1115/1.4005030.

Yao, Jianxi, Yan Su, Xuemin Song, Zuyuan Liu, Xide Cheng, and Chengsheng Zhan (2020). RANS Analysis of the Motions and Added Resistance for KVLCC2 in Head Regular Waves. *Applied Ocean Research* **105**, 102398. ISSN: 0141-1187. DOI: https://doi.org/10.1016/j.apor.2020.102398.

Yu, Jin-Won, Cheol-Min Lee, Jung-Eun Choi, and Inwon Lee (2017). Effect of ship motions on added resistance in regular head waves of KVLCC2. *Ocean Engineering* **146**, 375–387. ISSN: 0029-8018. DOI: 10.1016/j.oceaneng.2017.09.019.

Zeraatgar, H. and H. F. Abed (2006). Added resistance & drift force analysis in regular and irregular waves. *Marine Engineering* **2**.1, 1–16.

Zhang, Bao-Ji and Xu-Ning (June 2018). THE RESEARCH OF ADDED RESISTANCE IN WAVES BASED ON NONLINEAR TIME-DOMAIN POTENTIAL FLOW THEORY. *Journal of Marine Science and Technology* **26**.3, 343–351. ISSN: 1023-2796. DOI: 10.6119/JMST.2018.06_(3).0006.

Zou, Lu (2012). "CFD predictions including verification and validation of hydrodynamic forces and moments on ships in restricted waters". PhD thesis. Chalmers University of Technology.